

TWO-PHASE FLOW AND PHASE CHANGE HEAT TRANSFER  
IN SMALL STRUCTURES

TWEE FASEN STROMING EN FASEOVERGANG  
WARMTEOVERDRACHT IN KLEINE STRUCTUREN



# TWO-PHASE FLOW AND PHASE CHANGE HEAT TRANSFER IN SMALL STRUCTURES

PROEFSCHRIFT

ter verkrijging van de graad van doctor  
aan de Technische Universiteit Delft,  
op gezag van de Rector Magnificus prof.dr.ir. J.T. Fokkema  
voorzitter van het College voor Promoties,  
in het openbaar te verdedigen op woensdag 2 september 2009 om 15:00 uur  
door

Cornelius Maria ROPS

ingenieur in technische natuurkunde  
geboren te Nieuw-Ginneken

Dit proefschrift is goedgekeurd door de promotor:

Prof. dr. ir. J. Westerweel

Samenstelling promotie commissie:

Rector Magnificus	voorzitter
Prof. dr. ir. J. Westerweel	Technische Universiteit Delft, Promotor
Prof. dr. ir. M.T. Kreutzer	Technische Universiteit Delft
Prof. dr. ir. T.H. van der Meer	Universiteit Twente
Prof. dr. ir. G. Ooms	Technische Universiteit Delft
Prof. dr. ir. A.A. van Steenhoven	Technische Universiteit Eindhoven
Dr. ir. C.W.M. van der Geld	Technische Universiteit Eindhoven
Dr. W. Jouwsma	Bronkhorst High-Tech

ISBN: 978-90-9024517-1

Printed by: Ipskamp Drukkers B.V., Enschede

Cover: W. Schillemans

# Preface

This thesis is the result of about four years of scientific research on two-phase flow and phase transition heat transfer on small structures. The research is performed at TNO Science & Industry in close collaboration with the Laboratory for Aero & Hydrodynamics at Delft University of Technology. The first seeds of this fruitful collaboration were laid approximately five years ago by Prof. F.T.M. Nieuwstadt. The emerging research area called "microfluidics" opened new research and development possibilities, which were and still are of great interest for both Laboratory for Aero & Hydrodynamics and TNO Science & Industry.

Although only one name is present on the cover of this writing, it is clearly not the result of this one single person. Many people contributed in some way or another and for their input I am very grateful. First of all, I would like to thank Prof. J. Westerweel, for his input to keep me on a proper scientific path and for his time to have numerous discussions on and off the subject. Also his meticulous comments on my scientific writings are greatly appreciated. Likewise, the inspiring manner and the expert contribution of Prof. van der Geld answering our instantaneous request to comment on our work are highly appreciated. Next, I would like to thank dr. R. Lindken for his practically daily support, his efforts on the experiments and his ideas and enthusiasm. Furthermore, I would like to thank all other members of the Laboratory for Aero & Hydrodynamics for the nice working atmosphere and for inviting me for all social events as well.

During the four years of PhD-research at TNO Science and Industry I had the pleasure to work with all my helpful colleagues. Without detracting anybody from their merits, I would like to thank some of them in person. First, I have to thank Peter Paul van 't Veen and Machteld de Kroon for being the wonderful bosses who gave me the chance to work for TNO on this thesis. Next, Wim Peterse for always assisting me with a smile on the various experimental boiling setups. Han Velthuis, Rik van der Graaf, and Leon Geers for being highly appreciated sparring partners and Huib Blokland for the down to earth organisation. The cheerful discussions with Arnout Klinkenberg, Aris Twerda and Leander Noordijk have, in an indirect way, certainly contributed to this thesis as well. Likewise I mention the contributions of my five trainee students: Johan van der Dennen, Mohamed Oitrou, Peter Witte, Michael Dauda, and Christiaan Hollemans. Last but not least, an embrace for Bart Paarhuis who was my highly respected roommate and had to deal with me and all of my curiosities for most of the years.

However, a PhD is a twentyfour-seven process, demanding time and effort off-the-job as well. First, I would like to thank my parents for being there as a solid ground to start from. Next, I thank my brothers and sister: Jan, Bert, and Lisette for their warm and welcome support. Likewise, I am grateful for my family in law for creating the perfect background to feel at ease with. A special expression of thanks I want to give to Hilde. For being my wife, the mother of our two children, Hanna and Mathijs, and for her support, carefulness, cheerfulness, and lovingness not only during these past four years but hopefully for the rest of our lives.



# Table of contents

Preface .....	5
Table of contents .....	7
Summary .....	11
List of symbols .....	13
Latin .....	13
Greek.....	14
Subscripts.....	15
1 Introduction .....	17
1.1 Scaling .....	17
1.1.1 Dimensionless indicators.....	17
1.1.2 Flow transitions.....	18
1.1.3 Physical properties of some typical fluids .....	19
1.2 Effects of miniaturisation .....	19
1.2.1 Modelling aspects.....	20
1.2.2 Validity of engineering relations .....	22
1.2.3 Fabrication techniques.....	22
1.3 Micro-evaporator system: an illustrative example.....	23
1.4 Scope and outline of this thesis.....	25
1.4.1 Two-phase flow.....	25
1.4.2 Boiling .....	26
1.4.3 Outline of this thesis.....	26
2 Theoretical background.....	29
2.1 Two-phase flow .....	29
2.1.1 Void fraction .....	29
2.1.2 Vapour quality.....	30
2.1.3 Analytical void fraction models .....	30
2.1.4 Empirical void fraction models.....	32
2.1.5 Superficial velocity.....	33
2.1.6 Two-phase flow pattern map .....	34
2.1.7 Gas-Liquid systems: Macro-micro behaviour.....	36
2.2 Boiling bubble behaviour .....	37
2.2.1 Onset of nucleate boiling .....	37

2.2.2	Bubble size and departure time .....	39
2.2.3	Contact angle.....	42
2.2.4	subcooling of the bulk .....	43
2.2.5	Forced convection .....	44
2.3	Pool boiling.....	44
2.3.1	Wall superheat.....	44
2.3.2	Pool boiling curve.....	45
2.3.3	Nucleation site density.....	46
2.3.4	Pool boiling heat transfer mechanisms.....	46
2.3.5	Nucleate boiling heat transfer correlations .....	49
2.3.6	Critical heat flux correlations.....	52
2.4	Boiling within channels.....	53
2.4.1	Flow boiling map.....	53
2.4.2	Flow boiling heat transfer mechanisms .....	55
2.4.3	Flow boiling Heat transfer correlations.....	56
2.5	Summary.....	58
3	Air-water two-phase flow .....	59
3.1	Present status.....	59
3.1.1	Wambsganss et al. ....	59
3.1.2	Chung and Kawaji .....	60
3.1.3	Zhao and Bi .....	62
3.1.4	Tabatabai and Faghri.....	63
3.1.5	Literature comparison.....	65
3.2	Experimental .....	65
3.2.1	Experimental setup.....	65
3.2.2	Measurement method.....	68
3.2.3	Pattern definition.....	70
3.2.4	Contact angle rhodamine B/water - PMMA .....	72
3.3	Results and discussion.....	73
3.3.1	800 micron square channel .....	73
3.3.2	500 micron square channel .....	74
3.3.3	200 micron square channel .....	75
3.3.4	100 micron square channel .....	75
3.3.5	Overview .....	76

3.3.6	Conclusive remarks .....	78
4	Boiling miniaturisation.....	81
4.1	Present status.....	81
4.1.1	Nucleation site density.....	81
4.1.2	Bubble detachment frequency .....	85
4.1.3	Heater size effects.....	88
4.1.4	Literature discussion.....	90
4.2	Experimental .....	91
4.2.1	Experimental setup.....	91
4.2.2	Measurement method.....	93
4.2.3	Analysis of measurement assumptions.....	94
4.3	Results .....	96
4.3.1	Measurement results .....	96
4.3.2	Comparison of the results .....	98
4.3.3	Measurement set-up variation .....	99
4.3.4	High speed camera visualisation.....	102
4.4	Discussion .....	103
4.4.1	The confined pool boiling mechanism .....	103
4.4.2	Outscaling of confined pool boiling .....	104
4.5	Conclusions .....	106
5	Boiling within small-diameter channels.....	109
5.1	Present status.....	109
5.1.1	Small-diameter Flow boiling: instabilities.....	109
5.1.2	Confined bubble behaviour .....	113
5.1.3	Confined bubble growth.....	115
5.2	Elongated vapour bubble behaviour analysis.....	117
5.2.1	Single slug bubble detachment Modelling.....	117
5.2.2	Discussion on multiple channel flow.....	121
5.2.3	Explosive bubble growth Modelling.....	123
5.3	Experimental .....	125
5.3.1	Single slug bubble blockage setup .....	126
5.3.2	Explosive bubble growth setup.....	127
5.4	Experiment results .....	128
5.4.1	Single slug bubble blockage results .....	128

5.4.2	Explosive bubble growth results .....	129
5.4.3	Explosive bubble growth Model validation .....	131
5.4.4	Design recommendations.....	135
5.5	Conclusions .....	136
6	Conclusions and future work .....	137
6.1	Conclusions .....	137
6.2	Recommendations for future work .....	138
	Samenvatting.....	141
	Bibliography.....	143

## Summary

New production techniques, which became available since the 1980's, allowed the mass production of small sized fluidic systems. Reducing the size of a technical system alters the performance due to scaling effects. Physical phenomena which operate on volumes, such as gravity and inertia, become less important with respect to physical phenomena which act on surfaces or lines, such as pressure differences and surface tension. This relatively new research area on small sized fluidic systems is called "*micro-fluidics*". An illustrative example on the size reduction of an evaporator system shows a possible advantage of scaling down a physical process.

To characterise micro-fluidic flow dimensionless numbers can be used, such as the Reynolds number (Re), Weber number (We), Knudsen number (Kn) and Bond number (Bo). Gas-liquid two-phase flow systems are regarded to be small (or confined) if the Bond number is smaller than 4, or its square root inverse (i.e. the confinement number, Co) should be larger than 0.5.

The present work investigated the interaction of phase transition heat transfer and two-phase flow behaviour in small geometries. In order to get insight into the various interactions the research is split into two parts:

1. interaction between two-phase flow and small geometries,
2. interaction between phase transition heat transfer and small geometries.

The typical size of the "small geometries" regarded here range from about 5 mm down to about 0.1 mm. Furthermore, in general the liquid phase is water and the gaseous phase is either air or water vapour. In general standard conditions (i.e. pressure  $\sim 1 \cdot 10^5$  Pa and ambient temperature  $\sim 293$  K) are considered.

As a theoretical background the most commonly used two-phase flow concepts are introduced, such as the void fraction, superficial velocity, and two-phase flow pattern map. In literature an alternation in two-phase flow pattern map is observed on reducing the channel diameter. For example no horizontally stratified flow occurs in concurrent two-phase flow in small diameter channels. Only three anchor flow regimes are identified: bubble flow, slug flow, and annular flow. Textbook knowledge and the state of the art insights are presented on boiling bubble behaviour, nucleate pool boiling, and flow boiling. Various heat transfer mechanisms during nucleate boiling are described, as well as their interactions and relative importance.

An overview is given in literature readily available two-phase flow pattern maps, which are measured within small diameter channels ( $0.5 < Co < 50$ ). A reasonable agreement is found between these two-phase flow pattern maps found in literature. Likewise corresponds the present work ( $3 < Co < 25$ ) to the maps found in literature. This correspondence justifies the superficial velocity as a scaling parameter in plotting the two-phase flow pattern maps for both large diameter channels ( $Co < 0.5$ ) as small diameter channels ( $Co > 0.5$ ). The present work extends the researched regions of the two-phase flow pattern map to much lower superficial liquid velocities, in which the occurrence of stratified flow might be expected. The present experiments show no stratified flow or wavy flow pattern region. Therefore, in order to theoretically predict the transition lines the stratified flow is most likely not the

most adequate initial two-phase flow pattern. Annular flow is suggested to be a more appropriate initial two-phase flow pattern.

The present work on confined pool boiling demonstrates an enhancement of the nucleate boiling heat flux when the boiling pot diameter is decreased (i.e. increased confinement). In the nucleate boiling regime the heat flux in confined pool boiling is between 5 to 10 times higher than the heat flux for unconfined pool boiling. The analysis of possible errors and a variation of experimental parameters excludes that the observed enhancement is the result of the chosen boiling liquid, the variation in boiling pot depth, the material of the bounding wall, or the variation in the diameter of the inlet water supply. An explanation is found in the singularisation of the basic process for nucleate pool boiling, leading to a different flow behaviour. The flow pattern is chaotic in the case of unconfined pool boiling, and it becomes directed and circulating as the dimensions of the confinement are reduced. The circulating fluid motion augments the entrainment of liquid by the vapour bubbles, and hence it significantly increases the heat transfer in the nucleate boiling regime. Confined pool boiling could be integrated on a large scale by means of 'numbering up' or 'scaling out'.

Our research on flow boiling in small diameter channels gives a better understanding of the origin of the pressure fluctuations and the possible flow reversal. First, the measured length of a slug bubble at detachment agrees with the trend obtained by scaling analysis using a hydrodynamic force balance. The slope of the predicted linear correlation through the measurements corresponds to a 2% film thickness. This relative film thickness is similar to the values given in literature. By applying a similar hydrodynamic force balance on a multiple channel array, a criterion is found predicting vapour flow reversal. Within the flow reversal criterion the bubble cap position as a function of time is an important parameter. High-speed camera recordings allowed us to obtain the vapour bubble length during its explosive growth. Using simple assumptions we found an explicit relation for the vapour bubble length in time. After optimisation of the film thickness, this relation shows reasonable agreement with our explosive bubble length measurements. The explosive bubble growth model combined with the criterion predicting vapour flow reversal allows us to design the inlet restriction.

# List of symbols

## *Latin*

$a$	thermal diffusivity		$[m^2s]$
$A$	Area		$[m^2]$
$Bo$	Bond number		$[-]$
$Ca$	capillary number		$[-]$
$C_d$	drag coefficient		$[-]$
$Co$	confinement number		$[-]$
$C_p$	thermal capacity		$[Jkg^{-1}K^{-1}]$
$C_{3Dpen}$	correction factor for three dimensional penetration		$[-]$
$D$	diameter		$[m]$
$D_h$	hydraulic diameter		$[m]$
$E$	energy		$[J]$
$f$	fanning friction factor		$[-]$
$F$	force		$[N]$
$g$	gravitational acceleration constant:	9.81	$[ms^{-2}]$
$G$	mass flux		$[kgm^{-2}s^{-1}]$
$Gr$	Grasshof number		$[-]$
$h$	heat transfer coefficient		$[Wm^{-2}K^{-1}]$
$h_{ev}$	latent heat of evaporation		$[Jkg^{-1}]$
$H$	height		$[m]$
$Ja$	Jakob number		$[-]$
$Kn$	Knudsen number		$[-]$
$/$	typical system size		$[m]$
$L$	length		$[m]$
$m$	mass		$[kg]$
$\dot{m}$	mass flow		$[kgs^{-1}]$
$N_a$	nucleation site density		$[m^{-2}]$
$Nu$	Nusselt number		$[-]$
$p$	pressure		$[Pa]$
$Pr$	Prandtl number		$[-]$
$Q$	energy transport		$[W]$
$q''$	heat flux		$[Wm^{-2}]$

$r$	radius	[m]
$R_a$	micro roughness	[m]
Re	Reynolds number	[-]
S	slip ratio	[-]
t	time	[s]
T	temperature	[K]
u	velocity	[ms <sup>-1</sup> ]
$U_{SG}$	superficial gas velocity	[ms <sup>-1</sup> ]
$U_{SL}$	superficial liquid velocity	[ms <sup>-1</sup> ]
V	volume	[m <sup>3</sup> ]
We	Weber number	[-]
x	vapour quality	[-]
$X_{tt}$	Martinelli parameter	[-]
y	normal distance to heated surface	[m]

### ***Greek***

$\alpha$	void fraction	[-]
$\delta$	thickness of liquid film layer	[m]
$\Delta\rho$	density difference	[kgm <sup>-3</sup> ]
$\Delta T$	wall superheat	[K]
$\varepsilon$	mean distance between the molecules	[m]
$\theta$	contact angle	[°]
$\kappa$	mean free path of the molecules	[m]
$\lambda$	thermal conductivity	[Wm <sup>-1</sup> K <sup>-1</sup> ]
$\mu$	viscosity	[Pas]
$\rho$	density	[kgm <sup>-3</sup> ]
$\sigma$	surface tension	[Nm <sup>-1</sup> ]
$\tau$	characteristic time	[s]
$\phi$	flow rate	[m <sup>3</sup> s <sup>-1</sup> ]
$\chi$	molecular diameter	[m]

## ***Subscripts***

0	initial or reference
bf	bubble front
bub	bubble
cfb	convective flow boiling
CHF	critical heat flux
chan	channel
crit	critical
c-s	cross-section
eff	effective
entrance	entry of a flow structure
evap	evaporation
fb	flow boiling
flow	flow
gas	gas
hyd	hydrodynamic
kin	kinetic
liq	liquid
m_evap	evaporation mass
max	maximum
min	minimum
nb	nucleate boiling
nfb	nucleate flow boiling
ONB	onset of nucleate boiling
r	reduced
resp	response time
sat	saturation
surf	liquid-vapour interface
therm	thermal
tot	total
trans	transient
vap	vapour
wall	wall



# 1 Introduction

Physics is a science of which its main goal is to search for explanations of observations of natural phenomena. The explanations describe the observed phenomena as such that the description has predictive value. It is of interest to find proper descriptions of physical processes, or 'models', to control and adjust these processes. In the area of classical heat and mass transport many models, or 'laws', have been identified. The main challenge in this research area is therefore to obtain knowledge on their interaction and their range of validity. Most models are based on standard situations involving common materials and regular sizes. Deviation from these standards may lead to unexpected behaviour (Kolb and Hessel 2004; Herwig and Hausner 2003; Gad-El-Hak 2003).

In the 1980's production techniques became available for MEMS (Micro Electro Mechanical Systems). This allowed the mass production of small sized fluidic systems. Intriguing results sparked the excitement and renewed interest of researchers in the study of low Reynolds number flows at micro scales (Karniadakis and Beskok 2002).

Reducing the size of a technical system operating a certain physical process may alter its performance. The altered performance can be understood bearing in mind the different dependence on size of the various physical phenomena. Certain physical processes scale by volume e.g. body forces like gravity and inertia, while others scale by area e.g. surface tension forces and wall catalyst reactions. Consider a system with a characteristic length scale  $L$ . On scaling down this system, the volume related physical processes reduce in general by the characteristic length scale to the power three,  $L^3$  while the surface related physical processes only reduce in general by the characteristic length scale to the power two,  $L^2$ . Hence, process behaviour at regular scale may be governed by certain physical processes, while at small scale other physical processes may be dominant. This may lead to complete different process behaviour.

The challenge in this relatively new research area called *micro-fluidics* is to gain insight and understanding of the dominant physical phenomena in small systems and their interactions. An interesting process to study in a size-reduced system is the nucleate boiling process. This process contains various physical phenomena interacting together: Phase transition, two-phase flow and heat transfer. The buoyancy effects resulting from the large density differences in the fluid are typical volumetric forces. While the heat supply from the wall and the surface tension related physical processes scale by area.

## 1.1 Scaling

### 1.1.1 DIMENSIONLESS INDICATORS

In order to be able to identify which phenomenon is dominant with respect to another one certain dimensionless numbers are introduced. Typical numbers used to characterise micro-fluidic flow are:

$$\text{Reynolds number} \quad Re = \frac{\rho \cdot u \cdot D_h}{\mu} \quad \frac{\text{inertia forces}}{\text{viscous forces}} \quad (1.1)$$

$$\text{Weber number} \quad We = \frac{\rho \cdot u^2 \cdot D_h}{\sigma} \quad \frac{\text{inertia forces}}{\text{surface tension forces}} \quad (1.2)$$

$$\text{Capillary number} \quad Ca = \frac{\mu_{liq} \cdot u_{liq}}{\sigma} \quad \frac{\text{viscous forces}}{\text{surface tension forces}} \quad (1.3)$$

$$\text{Bond number} \quad Bo = \frac{\Delta\rho \cdot g \cdot D_h^2}{\sigma} \quad \frac{\text{gravitational forces}}{\text{surface tension forces}} \quad (1.4)$$

$$\text{Knudsen number} \quad Kn = \frac{\kappa}{L} \quad \frac{\text{indivial molecular}}{\text{group molecular}} \quad (1.5)$$

In the above equations the following notation is applied:  $\rho$  for density [kg/m<sup>3</sup>],  $u$  for velocity [m/s],  $D_h$  for hydraulic diameter [m],  $\mu$  for viscosity [Pas],  $\sigma$  for surface tension [N/m],  $\Delta\rho$  for density difference [kg/m<sup>3</sup>] and  $g$  for the gravitational acceleration constant 9.81[m/s<sup>2</sup>],  $\kappa$  for the mean free path length of the molecules and  $L$  is a characteristic macroscopic length.

### 1.1.2 FLOW TRANSITIONS

A characteristic flow transition marked by the Reynolds number is the laminar-to-turbulent flow transition. For round channels this transition occurs at a Reynolds number of about 2300 (Incropera and DeWitt 2001). Due to its small characteristic lengths, micro-fluidic flow is often regarded to be laminar. However, for high flow velocities (large pressure drops) the flow may become turbulent.

The critical Weber number below which an inviscid jet under weightless condition in vacuum is absolutely unstable is found to be  $\pi$  (Leib and Goldstein 1986). This means that at low Weber number no liquid jet is formed and only droplet flow will occur. Within micro-fluidic devices no jet formation is expected and liquid exits a capillary in a drop-wise manner. Although, for high velocities jet formation is possible (e.g. inkjet printers).

In case of an elongated gas bubble flow through a narrow channel, a characteristic change in flow pattern is noted at a capillary number of about 0.7 (Taylor 1961). Below this value the characteristic recirculation zones are present in the liquid plugs between the gas bubbles, while at higher capillary numbers a complete bypass flow occurs.

It is shown by Bretherton (1961) that the rise velocity of an elongated gas bubble vanishes in a sealed liquid phase capillary at a Bond number of about 3.4. In case of an air-water system this implies that below a channel diameter of about 5 mm the gravity forces are too small to induce bubble rise. The Bond number does not include a process variable such as the flow velocity and consists only of system parameters such as the hydraulic diameter and the physical fluid properties. Therefore, the Bond number is most often used to qualify whether a system is considered to be a microfluidic system (Kreutzer 2005).

The Knudsen number determines whether a fluid may be regarded as one entity or as a collection of individual molecules. For large Knudsen numbers the fluid acts as a collection of molecules with little internal interaction,  $Kn > 0.1$  (Bird 1994). In order to have enough molecular interaction (collisions) to prevent sudden velocity or temperature jumps near the wall the Knudsen number should be smaller than  $10^{-3}$ . These no-slip assumptions for velocity and temperature near the wall are commonly made in most physical models.

### 1.1.3 PHYSICAL PROPERTIES OF SOME TYPICAL FLUIDS

Some physical properties of fluids related to this research are shown in table 1.1 (taken from Weast *et.al.* 1980).

Table 1.1 – Fluids and their physical properties

Property Fluid		Density $\rho$ [kg/m <sup>3</sup> ]	Viscosity $\mu$ [Pas]	Therm.con. $\lambda$ [W/mK]	Therm.cap. $c_p$ [J/kgK]	Therm.diff. $a (= \lambda / \rho c_p)$ [m <sup>2</sup> /s]	Surf.tension $\sigma$ [N/m]	Boiling point @1bar [K]
Air	@293K	1.205	$1.8 \cdot 10^{-5}$	$2.57 \cdot 10^{-2}$	$1.0 \cdot 10^3$	$2.12 \cdot 10^{-5}$	--	--
water-vapour	@293K	0.77	/	$1.7 \cdot 10^{-2}$	$2.0 \cdot 10^3$	$1.04 \cdot 10^{-5}$	--	--
	@373K	$5.98 \cdot 10^{-1}$	$1.3 \cdot 10^{-5}$	$2.6 \cdot 10^{-2}$	$2.0 \cdot 10^3$	$2.17 \cdot 10^{-5}$	--	--
water-liquid	@293K	$9.98 \cdot 10^2$	$1.0 \cdot 10^{-3}$	$6.0 \cdot 10^{-1}$	$4.2 \cdot 10^3$	$1.43 \cdot 10^{-7}$	$7.3 \cdot 10^{-2}$	373
	@373K	$9.58 \cdot 10^2$	$2.8 \cdot 10^{-4}$	$6.8 \cdot 10^{-1}$	$4.2 \cdot 10^3$	$1.68 \cdot 10^{-7}$	$5.8 \cdot 10^{-2}$	
2-propanol	@293K	$7.86 \cdot 10^2$	$2.2 \cdot 10^{-3}$	$1.6 \cdot 10^{-1}$	$2.4 \cdot 10^3$	$8.36 \cdot 10^{-8}$	$2.4 \cdot 10^{-2}$	355
R134a	@298K <sup>@6.6bar</sup>	$1.21 \cdot 10^3$	$2.0 \cdot 10^{-4}$	$8.2 \cdot 10^{-2}$	$3.4 \cdot 10^2$	$2.01 \cdot 10^{-7}$	/	247
Aluminium	@293K	$2.70 \cdot 10^3$	--	$2.4 \cdot 10^2$	$9.0 \cdot 10^2$	$9.76 \cdot 10^{-5}$	--	--
Copper	@293K	$8.96 \cdot 10^3$	--	$3.9 \cdot 10^2$	$3.9 \cdot 10^2$	$1.12 \cdot 10^{-5}$	--	--
PMMA	@293K	$1.2 \cdot 10^3$	--	$1.9 \cdot 10^0$	$1.5 \cdot 10^3$	$1.06 \cdot 10^{-6}$	--	--
Teflon	@293K	$2.2 \cdot 10^3$	--	$3 \cdot 10^{-1}$	$1.0 \cdot 10^3$	$1.4 \cdot 10^{-7}$	--	--

## 1.2 Effects of miniaturisation

System miniaturisation incorporates various aspects. The alteration of the process behaviour may lead to new technical possibilities. The system design and the validation of the process modelling have to be carried out bearing in mind the new process situation. Likewise the construction of micro systems may be done differently from regular sized systems.

### 1.2.1 MODELLING ASPECTS

There are four fundamental assumptions that have to be satisfied in order to satisfy the validity of the Navier-Stokes equations (Gad-el-Hak 1999):

1. newtonian framework of mechanics: conservation of mass, energy and momentum,
2. the continuum approximation: space and time are indefinitely divisible,
3. thermodynamic (quasi-)equilibrium: linear relation between stress and rate of strain and between heat flux and temperature gradient (no-slip, no-temperature-jump boundary conditions),
4. Fourier's equation: no time delay exists for heat transport.

The first assumption is safe to make also in case of micro-systems: The fluid motion will not be in a relativistic or quantum mechanical domain. However, in order to satisfy the continuum assumption a sufficiently large number of molecules should be inside each fluid element. Therefore, if the spatial scale of the flow is not much larger than the mean distance between the fluid molecules not enough molecules will be in one control volume and the continuum assumption will not hold anymore. Finally, the last assumptions are imposed by the fact that it takes time for physical quantities to adjust to their surroundings. This adjustment is caused by the numerous molecular collisions. In order to guarantee enough collisions the mean free path of the molecules should be at least one order magnitude smaller than the flow length scale.

The above has already been studied with respect to rarefied gas dynamics, and can be 'translated to' small scale systems. The limits of the various approximations are shown in Figure 1.1.

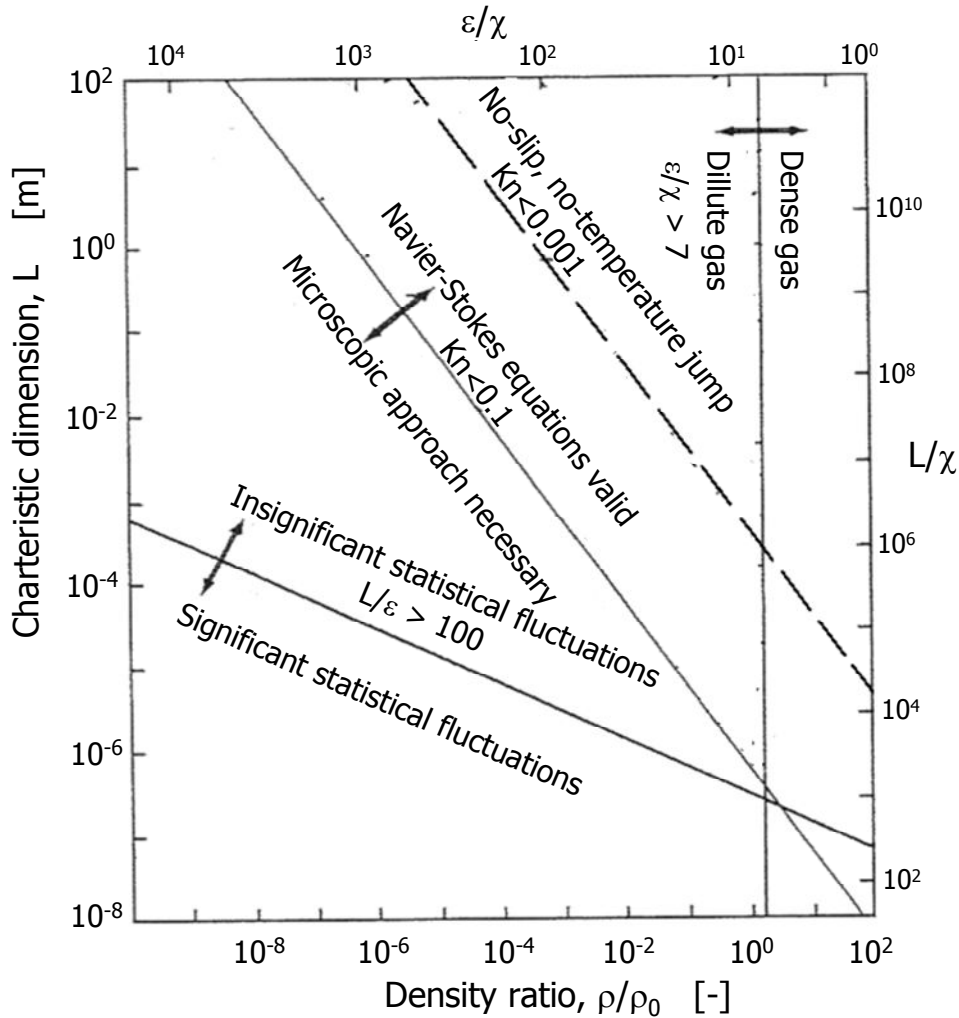


Figure 1.1 - Effective limits of different flow models for gases.  $L$  = characteristic flow dimension [m];  $\rho$  = density [kg/m<sup>3</sup>];  $\varepsilon$  = distance between molecules [m];  $\chi$  = molecular diameter [m]; Drawing after Bird (1994).

On the horizontal axis the (dimensionless) density, [-], of the fluid is given and on the vertical axis the characteristic length, [m]. Furthermore, the chart, as shown above, is made using a molecular diameter of 0.4 nm and  $\rho_0 = 1 \text{ kg/m}^3$ , which are comparable to air at standard conditions.

Fluids to the left of the vertical line in Figure 1.1 (indicated as  $\varepsilon/\chi > 7$ ) can be treated as dilute gasses, which means that intermolecular forces play no role. Above the lower gentle sloping line (indicated by  $L/\varepsilon > 100$ ) enough molecules are present ( $100^3 = 1 \cdot 10^6$ ) in the smallest volume of interest to compute proper macroscopic quantities (continuum approximation). The steeper solid line in Figure 1.1 (indicated as  $\text{Kn} < 0.1$ ) marks the boundary of the quasi-equilibrium assumption. This limit is governed by the Knudsen number. The Navier-Stokes equations are valid only if  $\text{Kn} < 0.1$ , although the no-slip boundary condition demands a stricter limit of  $\text{Kn} < 0.001$ .

For example, in case of air at 1 bar ( $\rho/\rho_0 \sim 1$ ), slip occurs if  $L < 100 \text{ } \mu\text{m}$ . The stress vs. strain-rate becomes non-linear if  $L < 1 \text{ } \mu\text{m}$ , and the continuum approximation fails completely if  $L < 0.4 \text{ } \mu\text{m}$ . However, in case of liquids ( $\varepsilon/\chi \sim 1$ ;  $\rho/\rho_0 \sim 10^2$ ) all

these limits are below characteristic lengths smaller than 1  $\mu\text{m}$ . This is smaller than the typical length scales applied in micro-flow devices.

### 1.2.2 VALIDITY OF ENGINEERING RELATIONS

On application of engineering relations one has to bear in mind that most of these dimensionless correlations are "best fits" to many experimental data. Therefore, they are only to be used within certain boundaries where some physical phenomena are dominant. Extrapolation of these results may lead to erroneous results. These boundaries are often marked by the various dimensionless numbers presented earlier.

Most of the engineering formulas are derived with respect to industrial applications in which the flow is most often turbulent,  $Re \gg 1$ . Due to the size reduction, the Reynolds number becomes small, indicating a laminar flow condition. Therefore, one should give attention whether the engineering formula is valid in the laminar flow regime as well.

In general engineering relations are obtained for fully developed process situations and entrance effects are not included. In case of miniaturised systems these entrance effects may be addressed with special attention. Generally, the entry length,  $L_{entrance}$ , of a Newtonian fluid is considered to be proportional to the Reynolds number (Hornbeck 1964) in case of laminar flow:

$$L_{entrance} = 0.056 \cdot Re \cdot D_h \quad (1.6)$$

Since equation (1.6) does not give good agreement for the case of low Reynolds numbers Dombrowski *et. al.* (1993) proposed the more general applicable equation:

$$\frac{L_{entrance}}{D_h} = \left[ (0.0575 \cdot Re)^2 + (0.655)^2 \right]^{1/2} \quad (1.7)$$

The thermal entry length can then be estimated by multiplication with the Prandtl number ( $Pr = \eta / \lambda \cdot c_p$ ).

### 1.2.3 FABRICATION TECHNIQUES

The miniaturisation of a given device into a Micro Electro Mechanical System (MEMS) allows (or requires) other fabrication techniques, such as automated high precision milling, layered manufacturing techniques and silicon etching techniques. Most of these manufacturing techniques allow complete integration of electronic circuits as well, leading to a highly compact and efficient device. The necessary high level of automation and the capability to batch fabricate allow these fabrication technologies for bulk fabrication. Micro devices made using these techniques are therefore inexpensive.

### 1.3 Micro-evaporator system: an illustrative example

The typical specifications of an evaporator system are the desired liquid mass (flow rate) to be evaporated and the desired reaction time. In case of the flow rate specification it most often holds that the higher the more desirable, while the reaction time is desired to be very small. However these specifications cannot be chosen at will, since they are linked by the system size and heat transfer, as we will show below.

First, the liquid flow specification implies the minimum needed area for evaporation. The evaporative heat flux,  $q''_{evap}$  [W/m<sup>2</sup>], is defined by the total evaporation energy,  $Q_{evap}$  [W], transported into the fluid divided by the evaporation area,  $A$  [m<sup>2</sup>]:

$$q''_{evap} = \frac{Q_{evap}}{A} \quad (1.8)$$

The energy,  $Q_{evap}$  needed to evaporate the liquid is given by:

$$Q_{evap} = \rho_{liq} \cdot \phi \cdot h_{ev} \quad (1.9)$$

where  $\rho_{liq}$  is the liquid density [kg/m<sup>3</sup>],  $\phi$  is the volumetric flow rate [m<sup>3</sup>/s] and  $h_{ev}$  is the latent heat [J/kg]. Combining equation (1.8) and equation (1.9) yields:

$$A = \frac{\rho_{liq} \cdot \phi \cdot h_{ev}}{q''_{evap}} \quad (1.10)$$

Since the evaporation area scales quadratic with a typical length scale of the evaporator, the typical minimum needed system size,  $l_{flow,min}$  imposed by the liquid flow specification is given by equation (1.11).

$$l_{flow,min} \sim \left( \frac{\rho_{liq} \cdot \phi \cdot h_{ev}}{q''} \right)^{1/2} \quad (1.11)$$

Next, the response time implies a maximum volume of the evaporator. In general the larger the volume, the larger the time constant of the evaporator system to react on a change. An exemplary time response,  $\tau$ , could be defined by the liquid flow-through time:

$$\tau \sim \frac{V}{\phi} \tag{1.12}$$

In which  $V$  is the evaporator volume [m<sup>3</sup>].

In general the evaporator volume,  $V$ , scales with the third power of a typical length scale of the evaporator,  $L$ . Therefore the maximum allowed system size,  $I_{resp\ max}$ , imposed by the response time specification is given by equation (1.13):

$$I_{resp\ max} \sim (\tau \cdot \phi)^{1/3} \tag{1.13}$$

Plotting together in one graph the typical minimum size needed for evaporation and the maximum allowed size with respect to the response time, an estimate of the possible attainable flow rates can be obtained, see Figure 1.2.

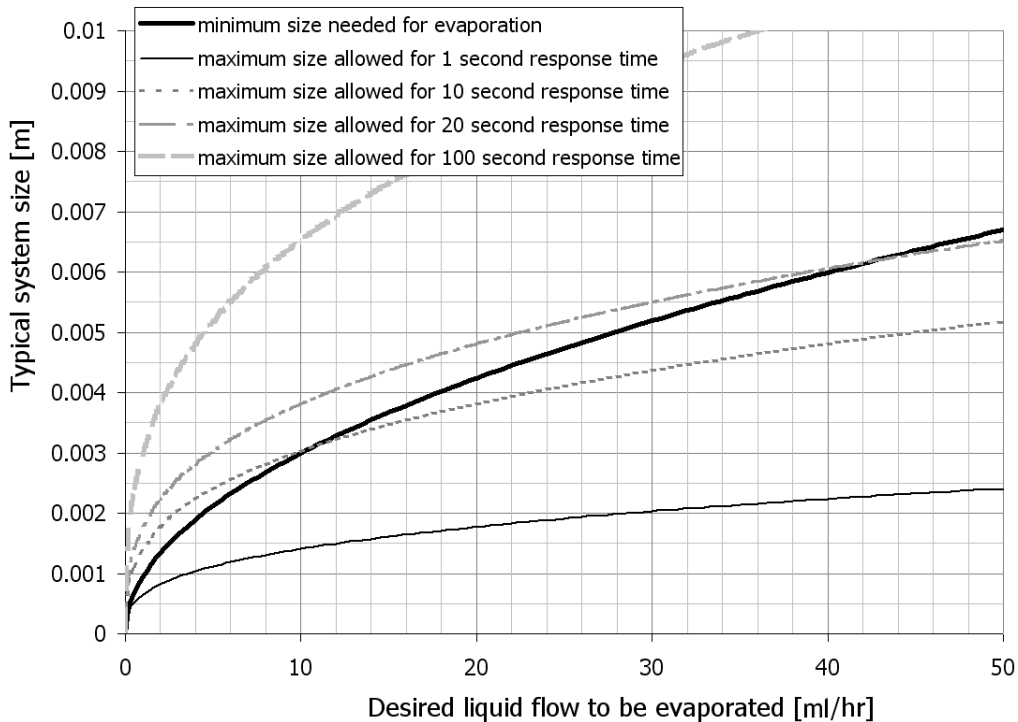


Figure 1.2 – Typical system size as a function of the desired maximum flow rate for three desired system time responses. The thick black line indicates the typical minimum size needed for complete evaporation. Typical values for boiling water are assumed: see Table (1.1) and  $q''=10^6$  W/m<sup>2</sup>.

In Figure 1.2 the thick black line indicates the typical minimum size needed to evaporate all entering liquid. Both the flow specification and the response time specification can be met, only if the estimated maximum size imposed by the response time is larger than the minimum size needed for evaporation. Conventional evaporators have a typical response time in the order of a few minutes ( $\sim 10^2$  s). If this response time needs shortening, the typical size of the evaporator needs to be reduced. However, Figure 1.2 shows that reducing the system size reduces in

general the maximum capacity as well. A typical system size of about 3 mm is found with a typical maximum liquid evaporation capacity of about 10 ml/hr. The typical response time of such a system would be about 10 s. Typical response times of 1 s can be achieved by reducing the typical system size below one millimetre. The flow capacity of such a system drops down to only a few tenths of a millilitre per hour.

Note that the above analysis is only indicative. A specific evaporator design enables us to stretch these typical limits. For example eight small single evaporators each with a response time of about ten seconds have an evaporative capacity of about eighty grams per hour. While packed in a cubic manner, the typical system size will be about six millimetres. The graph indicates that only about forty grams per hours can be evaporated with a typical single system length scale of 6 millimetres. This combined system will still have a response time of about ten seconds, or probably a bit longer due to control related delaying effects. This is faster than the expected typical twenty seconds for a single system with a typical size of six millimetres.

### ***1.4 Scope and outline of this thesis***

The aim of this research is to investigate the interaction of phase transition heat transfer and two-phase flow behaviour in small geometries. In order to get insight into the various interactions this research is split into two parts:

1. interaction between two-phase flow and small geometries,
2. interaction between phase transition heat transfer and small geometries.

The typical size of the "small geometries" regarded within this research range from about 5 mm (channel diameter for stagnant gas bubble) down to about 100  $\mu\text{m}$  (no-velocity slip, no-temperature jump assumption valid). Furthermore, in general water is assumed as liquid phase and air or water vapour as gaseous phases. Standard conditions (pressure  $\sim 1 \cdot 10^5$  Pa and ambient temperature  $\sim 293$  K) are considered.

#### 1.4.1 TWO-PHASE FLOW

Multiphase flow of gas and liquid occurs frequently in the production of oil and natural gas and in the transmission pipelines for both onshore and offshore operations. Multiphase flows are found in many other industrial processes as well. Usually the liquid and the gas are the products of a chemical reaction or simply a combination of the liquid and vapour phase of the same fluid (e.g. in case of boiling). Due to the complexity of the multiphase interaction and its common presence, much research is done in the past 50 years. However, most of the work is done on systems with a relatively large channel diameter, characterised by a Bond number larger than 1.

Research in the last decade has shown that the size of the channel influences the manner in which the liquid phase and gaseous phase flow together through the channel. In case of a horizontal channel, gravity may be able to pull down the liquid to the bottom of the channel establishing a horizontally stratified flow of the concurrent liquid and gas. Reducing the channel size such that the Bond number is less than 1, implies that gravity is less important. Horizontal stratification, which is a

result of gravitational forces, is therefore not likely to occur in these small sized channels.

#### 1.4.2 BOILING

Boiling is the phase transition of a liquid to its vapour which occurs at a solid-liquid interface. Due to the numerous interactions the physics of boiling becomes a complex phenomenon to describe. Dimensionless parameters governing the heat transfer physics during boiling can be obtained using the Buckingham  $\pi$  theorem (Fox and McDonald 1985). The heat transfer coefficient,  $h$  [W/m<sup>2</sup>K], is likely to be a function of the difference between the heated wall and the liquid saturation temperatures,  $\Delta T = T_{wall} - T_{sat}$  [K], the body force due to the liquid-vapour density difference,  $g(\rho_{liq} - \rho_{vap})$  [N/m<sup>3</sup>], a characteristic length scale,  $L$  [m], and the fluid properties: latent heat,  $h_{ev}$ , surface tension,  $\sigma$ , density,  $\rho$ , viscosity,  $\mu$ , heat capacity,  $c_p$  [J/kgK] and thermal conductivity,  $\lambda$  [W/mK]:

$$h = f(\Delta T, g(\rho_{liq} - \rho_{vap}), h_{ev}, L, \sigma, \rho, \mu, c_p, \lambda) \quad (1.14)$$

Since there are 10 variables and 4 dimensions (length [m], mass [kg], time [s], and temperature [K]) are available, 6 dimensionless groups can be formed related to the boiling heat transfer. For reasons of completeness, all six will be discussed below:

$$\frac{hL}{\lambda} = f \left[ \left( \frac{g(\rho_{liq} - \rho_{vap})L^2}{\sigma} \right), \left( \frac{\mu c_p}{\lambda} \right), \left( \frac{c_p \Delta T}{h_{ev}} \right), \left( \frac{\rho g(\rho_{liq} - \rho_{vap})L^3}{\mu^2} \right), \left( \frac{\mu^2}{\sigma \rho L} \right) \right] \quad (1.15)$$

The dimensionless heat transfer coefficient on the left hand side,  $hL/\lambda$ , is also known as the Nusselt number (Nu). The first dimensionless group on the right hand side is the Bond number (Bo), showing the influence of the buoyancy force (on the vapour bubbles) and the surface tension forces. The second group, the Prandtl number (Pr), indicates the ratio of the thermal boundary layer and the hydrodynamic boundary layer. Third, the Jakob number (Ja), denotes the ratio of sensible heat and the latent heat of the fluid. The fourth dimensionless group bears a strong resemblance with the Grasshof number (Gr), which relates the buoyancy forces to the viscous forces. The last dimensionless group is the ratio of viscous forces and the surface tension forces, like the squared Ohnesorge number ( $Z = We^{1/2} / Re$ ).

#### 1.4.3 OUTLINE OF THIS THESIS

In chapter two the general theoretical background on the various subjects is given. Chapter three gives the current status on small diameter two-phase flow pattern mapping and describes the measurement setup and results of our research. Chapter four deals with the miniaturisation of a pool boiling setup. Current theories are given in more detail explaining the observations done in the present research. Chapter five

contains the results of the miniaturised flow boiling experiments, which combine all three aspects: phase transition heat transfer, two-phase flow and small geometries. Finally, in chapter six the conclusions, which are drawn from the research described in this thesis, are summarised.



## 2 Theoretical background

This chapter describes the generally available and accepted knowledge on two-phase flow, boiling bubble behaviour, pool boiling and flow boiling. Their most commonly used parameters and theories relevant for this thesis will be introduced in this chapter. Apart from specific references, this textbook knowledge can be found in *Fundamentals of Heat and Mass transfer* (Incropera and DeWitt 2002), the *VDI Wärmeatlas* (Schlünder *et al.* 1994), and the *Wolverine engineering data book III* (Thome 2004).

### 2.1 Two-phase flow

A lot of research has been done in the wide spectrum of multiphase flow research. Within this section only a short overview on two-phase flow and its most commonly used parameters relevant for this thesis will be introduced.

#### 2.1.1 VOID FRACTION

The void fraction,  $\alpha$ , is one of the most important parameters used to characterize two-phase flows. However, various definitions are available for specifying the amount of void (gas or vapour) in a flow: local, chordal, cross-sectional, and volumetric void fraction (e.g. Thome 2004). These definitions are all more or less related to a specific measurement method. The local void fraction,  $\alpha_{local}$  is measured using a miniature probe resulting in  $\alpha_{local} = 1$  if the gas is present in the very small measurement volume and  $\alpha_{local} = 0$  if the probe tip is covered by the liquid. Due to the rather binary character of the signal typically the time-averaged local void fraction is used. The chordal void fraction,  $\alpha_{chordal}$  is typically measured using a narrow beam of radiation from a radioactive source through the flow (e.g. Thome 2004). The detected radiation intensity on the opposite side is a measure of the absorption and thus a measure of the void fraction along the beam path. The cross-sectional void fraction,  $\alpha_{c-s}$  can be measured either by optical means or indirectly by electrical means using the capacitance of a conducting liquid (e.g. Thome 2004). It is defined as:

$$\alpha_{c-s} = \frac{A_{gas}}{A_{liq} + A_{gas}} \quad (2.1)$$

where  $A_{gas}$  is the cross-sectional area occupied by the gas and  $A_{liq}$  is the cross-sectional area occupied by the liquid.

The volumetric void fraction,  $\alpha_{vol}$  is typically measured using a pair of quickly closing valves installed along a channel that trap the two-phase fluid (e.g. Thome 2004). Subsequently its respective liquid and gas/vapour volumes are determined.

The most widely used void fraction definition is the cross-sectional average void fraction,  $\alpha_{c-s}$ , henceforth simply referred to as the void fraction,  $\alpha$ , in the remainder of this thesis.

### 2.1.2 VAPOUR QUALITY

The vapour quality,  $x$ , is a thermodynamic quantity that indicates the amount of vapour/gas in a flow. Instead of using a geometrical indicator like the cross-sectional area or volume ratio, the ratio of masses is used (e.g. Thome 2004):

$$x = \frac{m_{gas}}{m_{liq} + m_{gas}} \quad (2.2)$$

Note that due to the difference in density of the liquid and gaseous phase that the values of the void fraction and the vapour quality may differ significantly. For example, a tube containing mainly a gas/vapour flow with only a few small liquid droplets the void fraction is almost 1, however due to the much higher water density ( $\rho_{liq} \sim 10^3 \text{ kg/m}^3$ ,  $\rho_{gas} \sim 10^0 \text{ kg/m}^3$ ) the vapour quality may still be as low as 0.1, see Figure 2.1.

### 2.1.3 ANALYTICAL VOID FRACTION MODELS

The relation between the void fraction and the vapour quality can be found using the homogenous void fraction approach. From the definition of the (cross-sectional) void fraction of a channel of area  $A$  and a volumetric flow rate  $\phi$ , the mean vapour and liquid velocities are (e.g. Thome 2004):

$$u_{gas} = \frac{\phi_{gas}}{A\alpha} = \frac{\dot{m}_{tot} x}{\rho_{gas} \cdot A\alpha} \quad (2.3)$$

$$u_{liq} = \frac{\phi_{liq}}{A(1-\alpha)} = \frac{\dot{m}_{tot}(1-x)}{\rho_{liq} \cdot A(1-\alpha)}$$

The homogeneous approach assumes that the liquid and vapour phases flow at equal velocities. Therefore equating the expressions for the vapour and liquid velocity yields:

$$\alpha_{homogeneous} = \frac{\frac{x}{\rho_{gas}}}{\frac{1-x}{\rho_{liq}} + \frac{x}{\rho_{gas}}} = \frac{1}{1 + \left(\frac{1-x}{x}\right) \frac{\rho_{gas}}{\rho_{liq}}} \quad (2.4)$$

The assumption of equal liquid and vapour velocities used in the homogeneous void approach is only reasonable in a limited range of circumstances. Therefore, the concept of velocity ratio (also referred to as the slip ratio),  $S$ , is introduced:

$$S = \frac{U_{gas}}{U_{liq}} \quad (2.5)$$

The introduction of the slip ratio leads to a more general relation between the void fraction and the vapour quality:

$$\alpha = \frac{1}{1 + \left(\frac{1-x}{x}\right) \cdot \frac{\rho_{gas}}{\rho_{liq}} S} \quad (2.6)$$

and

$$x = \frac{1}{1 + \left(\frac{1-\alpha}{\alpha}\right) \cdot \frac{1}{\frac{\rho_{gas}}{\rho_{liq}} S}} \quad (2.7)$$

Numerous analytical and empirical correlations have been developed for determining the slip ratio and consequently the actual void fraction. In most approaches some quantity, like momentum or kinetic energy of the two-phases, is minimised under the assumption that the flow will settle in the minimum of this quantity. Using a momentum flux model the velocity ratio is proportional to the square root of the vapour-liquid density ratio (e.g. Thome 2004):

$$S_{momentum} = \left(\frac{\rho_{gas}}{\rho_{liq}}\right)^{-1/2} \quad (2.8)$$

On the other hand optimisation with respect to the kinetic energy gives (e.g. Thome, 2004):

$$S_{kin.energy} = \left(\frac{\rho_{gas}}{\rho_{liq}}\right)^{-1/3} \quad (2.9)$$

A generalisation of eq. (2.8) and eq. (2.9) gives  $S = (\rho_{gas}/\rho_{liq})^n$  which leads to the following expression of eq.(2.6):

$$\alpha = \frac{1}{1 + \left(\frac{1-x}{x}\right) \left(\frac{\rho_{gas}}{\rho_{liq}}\right)^n} \quad (2.10)$$

in which  $n=0.5$  in case of the momentum flux approach and  $n=0.67$  applying a kinetic energy model (Thome 2004). More elaborate analytical models are available as well, which add a sort of constant in front of the vapour quality ratio and a power as well, i.e.  $c\left(\frac{1-x}{x}\right)^m$ .

Figure 2.1 shows the various void fraction models and the visualisations made by Nino *et al.* (2003). The void volume inside a channel is already substantial even at rather low vapour qualities.

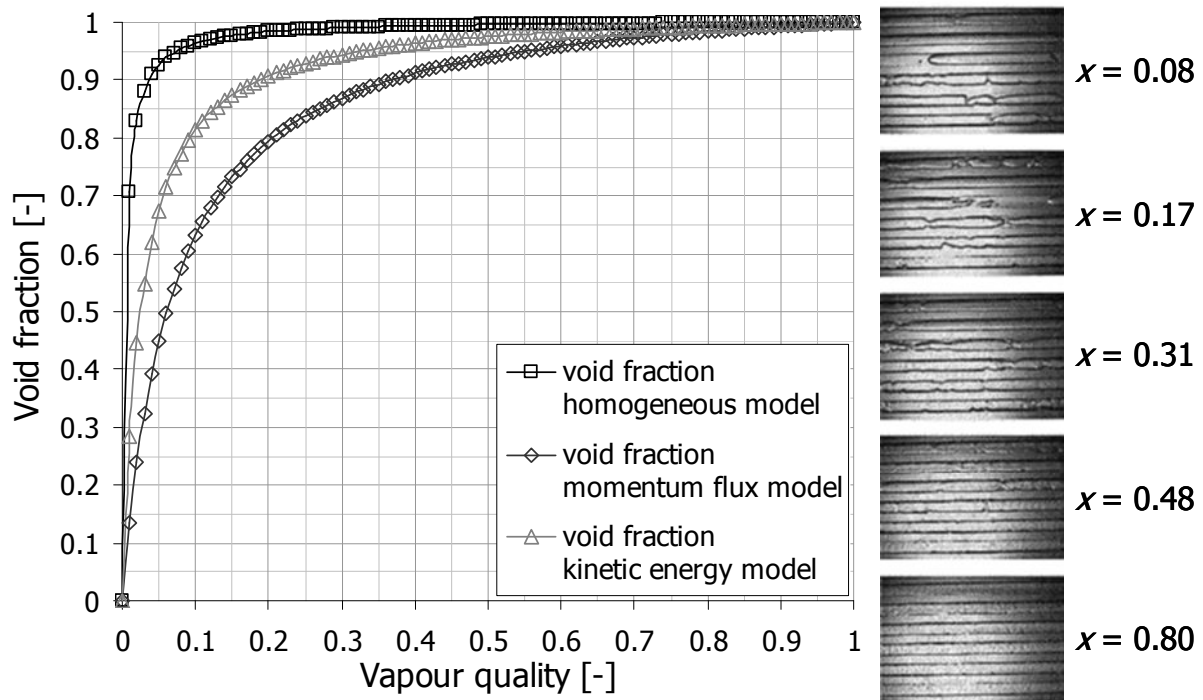


Figure 2.1 – Three basic void fraction models ( $\rho_{gas} = 5 \text{ kg/m}^3$  and  $\rho_{liq} = 1206 \text{ kg/m}^3$ ). Right hand side pictures: Visualisation by Nino *et al.* (2003) of the void fraction at different vapour qualities (Refrigerant R134a).

#### 2.1.4 EMPIRICAL VOID FRACTION MODELS

Equation (2.10) is the kind of general expression used in empirical models to relate the void fraction and vapour quality. Experimental studies show that the slip ratio depends on the following parameters: physical properties of the liquid and the gas/vapour (in particular the density ratio,  $\rho_{gas}/\rho_{liq}$ , and the viscosity ratio,  $\mu_{liq}/\mu_{gas}$ ), the local vapour quality, the mass velocity and some secondary variables (like geometry, heat flux and multiphase flow pattern), see Thome (2004). Butterworth

(1975) has shown that many (cross-sectional) void fraction equations can be fitted to the standard generalised expression:

$$\alpha = \frac{1}{1 + n_B \left( \frac{1-x}{x} \right)^{n_1} \left( \frac{\rho_{gas}}{\rho_{liq}} \right)^{n_2} \left( \frac{\mu_{liq}}{\mu_{gas}} \right)^{n_3}} \quad (2.11)$$

The terms following  $n_B$  are also known as the Martinelli parameter,  $X_{tt}$ . Depending on which physical property is studied the constants,  $n_1$ ,  $n_2$  and  $n_3$ , in this parameter may vary. For example, in case of a two-phase flow over vertical tube bundles the constants  $n_1$ ,  $n_2$  and  $n_3$  are usually set at 1, 0.57 and 0.11 respectively (Schlünder *et al.* 1994). In case of a two-phase flow over horizontal tube bundles the numbers 0.9, 0.5 and 0.1 are commonly used as constants  $n_1$ ,  $n_2$  and  $n_3$  respectively.

#### 2.1.5 SUPERFICIAL VELOCITY

Due to its complexity many empirical relations and graphs for engineering purposes have been developed. Much of the two-phase flow behaviour depends on the amount of liquid and vapour transported, which can be expressed using the superficial velocity for the liquid and gaseous phase separately. The liquid superficial velocity is defined by the total liquid volume flow divided by the total cross area of the channel. A similar definition holds for the superficial gas/vapour velocity.

$$U_{SL} = \frac{\phi_{liq}}{A} \quad (2.12)$$

$$U_{SG} = \frac{\phi_{gas}}{A} \quad (2.13)$$

Note that the superficial liquid velocity is not equal to the mean liquid velocity in the channel, since the gaseous phase occupies part of the channel as well. The superficial velocity can be seen as the average velocity of the phase if no second phase would be flowing through the channel as well. Although the superficial velocity is not dimensionless like the Martinelli parameter, it is a general parameter typically used in multiphase flow pattern maps.

The mass flux,  $G$  [kg/m<sup>2</sup>s], through a channel is the superficial velocity multiplied by the density, such that:

$$G_{liq} = U_{SL} \cdot \rho_{liq} \quad (2.14)$$

and

$$G_{gas} = U_{SG} \cdot \rho_{gas} \quad (2.15)$$

### 2.1.6 TWO-PHASE FLOW PATTERN MAP

Typically, for most industrial processes, and therefore in research as well, the Bond number, defined in eq.(1.4), is (much) larger than one. This indicates that gravitational forces are (by far) dominant over surface tension forces. In almost all two-phase flow systems the liquid phase has a much higher density than the gaseous phase. This means that the orientation of the channel influences the observed flow pattern for identical gas-liquid mixture flowing concurrent through the channel. Therefore, the first and most common distinction to be made is between horizontally and vertically oriented channels. Within this distinction, the manner in which two-phases flow concurrently through a channel depends on the ratio and the amount of the liquid and gaseous phase. However, it appears that if the flow of the phases is expressed as a superficial velocity, the flow pattern maps for one specific liquid-vapour combination roughly coincide regardless of the channel diameter.

The following recognisable flow structures, also called flow patterns, are defined (e.g. Thome 2004):

1. *Bubbly flow* : Numerous gas bubbles are observable. The bubbles may vary in size and shape, however they are typically nearly spherical and much smaller than the channel diameter. The superficial gas/vapour velocity is low.
2. *Slug flow* : On increasing the superficial gas velocity, the gas bubbles become larger and occupy nearly the complete channel diameter. The bubbles have typically the shape of a bullet (spherical cap, cylindrical body and blunt tail). These large bubbles (also called Taylor bubbles) are separated by slugs of liquid, which may include small bubbles.
3. *Churn flow* : This is an unstable structure containing large bubbles of irregular shape and annular films interacting with each other by liquid bridges crossing the channel diameter. The liquid phase may include small bubbles as well.
4. *Annular flow* : On further increasing the superficial gas velocity, the liquid phase is expelled from the centre of the tube. An annular ring of liquid is formed on the wall, while the gas flows in a continuous phase through the centre of the channel. The (thin) liquid layer may be entraining small gas bubbles, likewise the gas flow may entrain small liquid droplets.
5. *Mist flow* : At very high superficial gas velocities no liquid remains at the wall. The gas flow entrains all liquid in the form of small droplets, analogous to the inverse of the bubbly flow regime.

In horizontal channels two additional flow patterns can occur:

6. *Stratified flow* : At low superficial liquid and gas velocities gravity is able to pull the heavier phase (which is in general the liquid phase) towards the bottom of the (horizontal) channel. Complete separation of the phases occurs, horizontally stratifying the two-phase flow.

7. (*Stratified-)*Wavy flow : Due to the increased gas velocity the interface of the liquid and gas remains no longer undisturbed. Waves are formed on the interface. Their amplitude is notable and depends on the relative velocity, however their crests do not reach the opposite side of the channel

The flow patterns for concurrent flow of a gas and a liquid are shown in Figure 2.2.

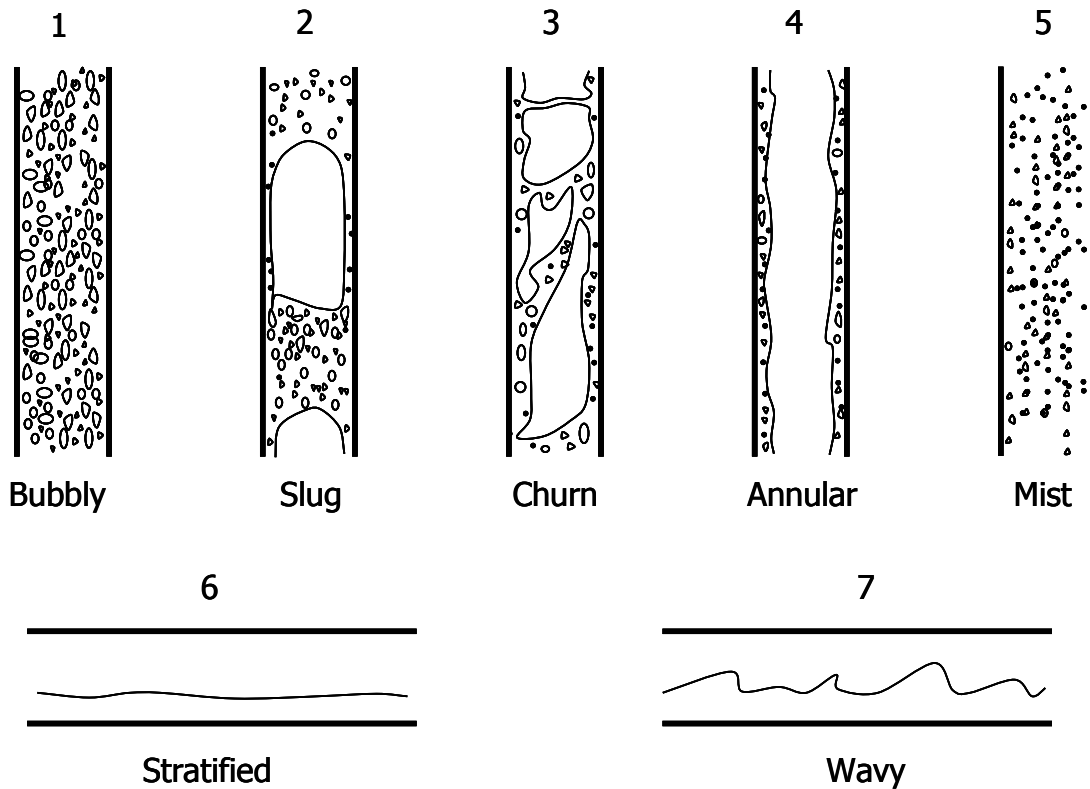


Figure 2.2 – Two-phase flow patterns. The numbers refer to the description of the flow patterns in the text. Flow patterns 1, 2, 4 and 5 may occur in both vertical channels as horizontal channels. Flow pattern 6 and 7 may only occur in horizontal channels.

The typical location of each flow pattern is given in Figure 2.3.

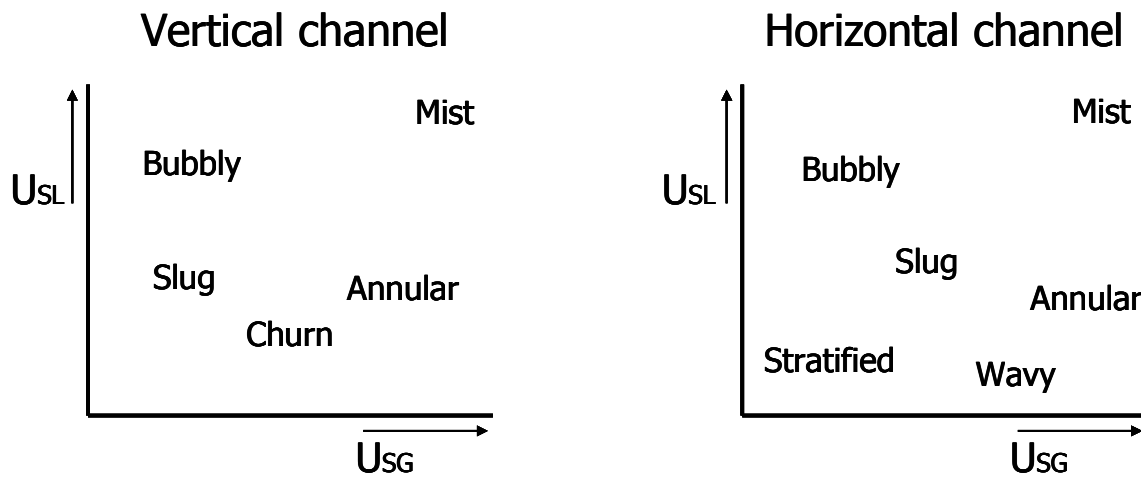


Figure 2.3 – General two-phase flow pattern maps using the superficial velocity of the liquid phase on the horizontal axis and the superficial velocity of the gaseous phase on the vertical axis. Left: Typical flow pattern positions for a vertical channel. Right: Typical flow pattern positions for a horizontal channel.

#### 2.1.7 GAS-LIQUID SYSTEMS: MACRO-MICRO BEHAVIOUR

As mentioned previously, the dimensions of the channel may influence the manner in which the liquid and gaseous phase flow together through the channel. For example in a regular size (channel diameter  $> 1$  cm) horizontal channel gravity may be able to 'pull down' the liquid to the bottom of the channel, horizontally stratifying the concurrent liquid and gas flows. Reducing the channel size implies that gravity effects will become less dominant. Horizontal stratification, which is a result of gravitational forces, is therefore not likely to occur in small diameter channels. Experimental observations of two-phase flow in small diameter channels reported in literature (e.g. Wambsganss *et al.* 1991, and Chen *et. al.* 2006) show a difference in the observed flow regimes. In general only three flow regimes are sufficient to describe the observed patterns:

1. *isolated bubble flow* : Similar to bubbly flow in large channels,
2. *slug flow* : Large bubbles occupy nearly the complete channel diameter. The bubbles have a cylindrical shape with spherical caps at the front and the back of the bubble. These large bubbles are separated by liquid slugs containing no bubbles,
3. *annular flow* : Similar to annular flow in large channels, however the presence of small liquid droplets in the core gas flow is not clear. Partial dryout of the annular film is observed as well (Bonjour and Lallemand, 1998).

The most commonly used dimensionless number to distinguish large diameter channels and small diameter channels is the Bond number, defined in eq.(1.4), or its square root inverse, the Confinement number:

$$Co = \sqrt{\frac{\sigma}{g(\rho_{liq} - \rho_{gas})D_h^2}} \quad (2.16)$$

Kew and Cornwell (1997), amongst other researchers, found that  $Co > 0.5$  defines the micro channel flow regime for two-phase flow. This means that in case of an air-water system (with  $\sigma$ ,  $\rho_{liq}$ , and  $\rho_{gas}$  given in Table (1.1)) channel diameters smaller than 5 mm may be regarded as small diameter channels. Note that channels with a hydraulic diameter less than 2.5 mm result in a Bond number less than unity for an air-water system.

## 2.2 Boiling bubble behaviour

One of the most characterising features of boiling is the presence of the vapour phase throughout the complete liquid. Typically, the vapour leaves the heated surface as bubbles. The following sections discuss the onset of the vapour bubbles, the bubble departure and the influence of physical phenomena. These phenomena form the basics for understanding the pool boiling heat transfer and the flow boiling heat transfer, sections 2.3 and 2.4.

### 2.2.1 ONSET OF NUCLEATE BOILING

The wall temperature at which the first bubbles start to rise from the heated surface is defined as the temperature for the *onset of nucleate boiling* (ONB) (Incropera and DeWitt, 2002). Bubbles originate at small cavities present on the surface of the heater. Vapour trapped in a cavity forms a bubble nucleus, which can grow and develop into a bubble. Within a spherical bubble the pressure,  $p$ , is higher than in the surrounding liquid. The pressure difference,  $\Delta p$ , (at thermo-dynamic equilibrium) is described by the Young-Laplace relation (Hsu, 1962):

$$\Delta p = \frac{2\sigma}{r_{bub}} \quad (2.17)$$

Where  $\sigma$  is the surface tension and  $r_{bub}$  the radius of the vapour bubble.

The saturation temperature,  $T_{sat}$ , inside the vapour bubble is estimated by combining the above Young-Laplace equation with the Clausius-Clapeyron equation:

$$T = T_{sat} + \frac{2\sigma T_{sat}}{r_{bub} \rho_{vap} h_{ev}} \quad (2.18)$$

Hsu (1962) assumes the cavity to be smaller than the thickness of the laminar thermal boundary layer. The initial bubble size from which the vapour bubble starts its growth, is assumed to be of similar size as the cavity it originates from. Therefore, a linear relation for the temperature in thermal boundary layer approximates the temperature distribution in the liquid surrounding the vapour bubble:

$$T(y) = T_{\text{wall}} - \frac{q'' y}{\lambda_{\text{liq}}} \quad (2.19)$$

Where  $y$  is the normal distance from the heated surface and  $T(y)$  the temperature at this location in the liquid.

For a bubble to grow several researchers (e.g. Hsu, 1962; Davis and Anderson, 1966) postulated that the liquid temperature surrounding the bubble should at least be equal to the saturation temperature inside the bubble. This condition supports evaporation at its interface and allows the bubble to grow.

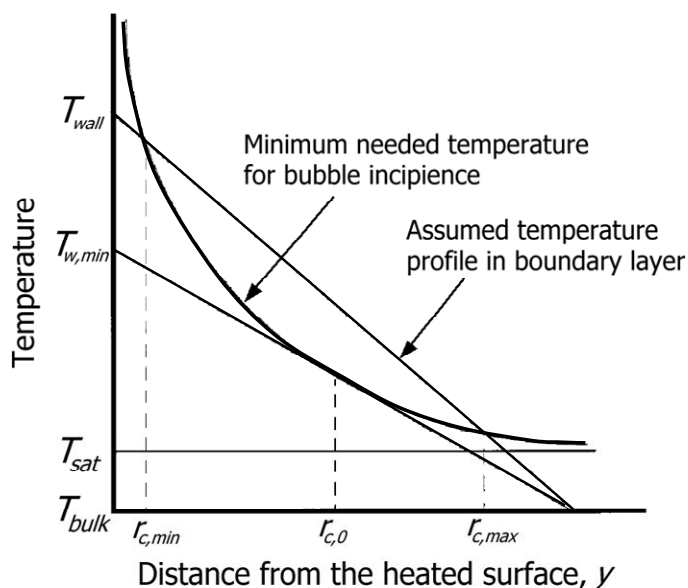


Figure 2.4 – Schematic depiction of the criteria necessary for bubble incipience.  $r_{c,min}$  is the minimum cavity size allowed for nucleation,  $r_{c,max}$  is the maximum cavity size allowed for nucleation, and  $r_{c,0}$  is the cavity size permitting nucleation at the minimum wall temperature; Drawing after Hsu (1962).

Using equations (2.18) and (2.19) the heat flux required to initiate nucleate boiling can be derived. This is shown schematically in Figure 2.4. The supplied heat flux determines the steepness of the linear temperature profile and thus the wall temperature. Assuming that the bubble has to be surrounded by liquid which has a higher temperature than the vapour within the bubble, any bubble with an internal temperature exceeding the liquid boundary layer temperature collapses. The position of the bubble tip can be related to the bubble radius,  $r_b$ , and the cavity radius,  $r_c$  (Davis and Anderson, 1966). By equating the internal bubble temperature to the liquid layer temperature at the bubble tip the range of possible bubble sizes (and

therefore cavity sizes) can be determined. The minimum needed heat flux for bubble nucleation is found by equating the derivatives of equations (2.18) and (2.19) as well. In case a hemispherical bubble is assumed (i.e.  $y_{bub} = r_{bub}$  and  $r_c = r_{bub}$ ), the following relation for the minimum needed heat flux is derived (Basu, 2002):

$$q_{ONB}'' = \frac{\lambda_{liq} h_{ev} \rho_{vap}}{8\sigma T_{sat}} (T_{wall} - T_{sat})^2 \quad (2.20)$$

Another type of assumption on the bubble shape will lead to a similar expression, see for example section 2.2.3.

## 2.2.2 BUBBLE SIZE AND DEPARTURE TIME

The initial vapour bubbles grow over time due to vaporisation. The vaporisation process is maintained by an energy transfer from the superheated liquid to the bubble interface. Several studies (e.g. Bosnjakovic 1930; Jakob and Linke 1935; and Plesset and Zwick 1952) show that the growth of a vapour bubble is mainly dominated by the evaporation flux. In general the surface tension and the liquid inertia (i.e. bubble dynamics characterised by the Rayleigh-Plesset equation) only play a secondary role.

It is assumed that the saturation temperature at the bubble interface is constant. For a uniformly superheated liquid, the bubble growth problem is analogous to the one-dimensional transient heat conduction problem (Zuber 1961). The energy balance for a growing bubble shows:

$$h_{ev} \rho_{vap} \frac{dr_{bub}}{dt} = h(T_{liq} - T_{sat}) = \lambda_{liq} \left( \frac{\partial T}{\partial y} \right)_{y=0} = \lambda_{liq} \frac{T_{liq} - T_{sat}}{\sqrt{\pi a t}} \quad (2.21)$$

where  $a$ , [ $m^2/s$ ], is the thermal diffusivity; ( $a = \lambda / \rho c_p$ ) and  $t$  [s] is penetration time.

Since this is an idealised case, correction factors are necessary to take into account the effects of liquid inertia, surface tension, the moving boundary and sphericity. According to Zuber (1961) the spherical shape introduces a factor,  $C_{3Dpen}$ , of  $\pi/2$  in front of the penetration depth  $\sqrt{\pi a t}$  in equation (2.21). Although Plesset and Zwick (1954) suggest a factor  $\sqrt{3}$ . The numeric values of the two suggested shape factors do not differ too much:  $\pi/2 \approx 1.57$  and  $\sqrt{3} \approx 1.73$ . We chose the shape factor suggested by Zuber (1961), since it nicely cancels the integration factor. The relation describing the bubble radius as a function of time thus becomes:

$$R = \left( \frac{\pi}{2} \right) \frac{2}{\pi} \frac{\rho_{liq} C_{p-liq} (T_{liq} - T_{sat})}{h_{ev} \rho_{vap}} \sqrt{\pi a t} \quad (2.22)$$

During the vapour bubble growth several forces act on the bubble (Mori and Baines 2001; Chen 2002; Geld 2007). The forces detaching the bubble are the buoyancy force, contact pressure force and the liquid inertia. Forces keeping the bubble attached to the heated surface are the surface tension force, bubble inertia force and the drag force related to the bubble growth.

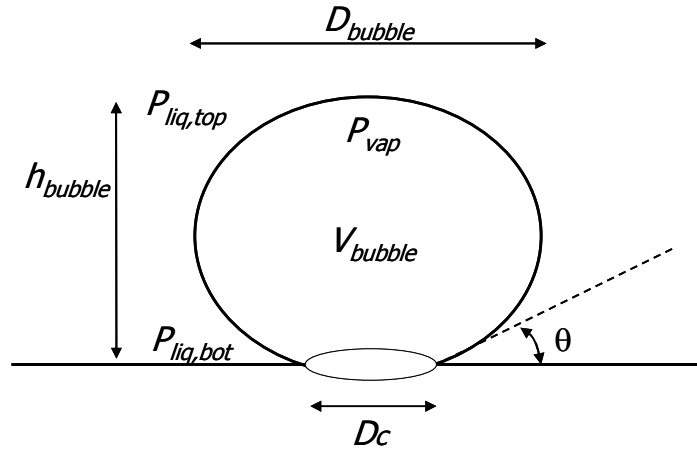


Figure 2.5 – A bubble growing on a heated surface.

The most obvious force detaching a vapour bubble is the buoyancy force,  $F_{buoyancy}$ . This volume force is obtained by employing the Gauss theorem to convert the surface integral of the liquid pressure to a volume integral. In case the bubble is fully surrounded by liquid the whole enclosing surface will contribute.

$$\iiint P_{liq} dA = \iiint \rho_{liq} g \cdot dV = \rho_{liq} g V_{bub} \quad (2.23)$$

Where  $dA$  is an infinitesimal small partition of the bubble surface. However, in case the bubble is attached to the wall the contact area,  $\pi/4 \cdot D_c^2$ , will not contribute to the buoyancy force (Geld 2007). By simply calculating the buoyancy force active on the attached bubble using equation (2.23) would imply that that wall contact area of the bubble experiences also a liquid pressure equal to the liquid pressure near the wall,  $P_{liq,bot}$ . Since no liquid is present this should be accounted for by subtracting the contribution of the contact area (Helden *et al.* 1995). Likewise the weight of the bubble has to be subtracted as well. The corrected buoyancy force for an attached bubble becomes:

$$F_{buoyancy} = \rho_{liq} g V_{bub} - \frac{\pi}{4} D_c^2 \cdot P_{liq,bot} - \rho_{vap} g V_{bub} \quad (2.24)$$

The contact area does give rise to a contribution to the bubble detaching forces. The pressure excess inside the bubble exerts a detaching force on the wall at the bubble contact area (Geld 2007).

$$F_{contact.pres} = \frac{\pi}{4} D_c^2 \left[ \sigma \left( \frac{1}{R_1} + \frac{1}{R_2} \right) \right] \quad (2.25)$$

where  $R_1$  and  $R_2$  are the bubble curvature radii.

Chen (2002) obtains the same total result for the corrected buoyancy force and the contact pressure force, however his reasoning is from a physical point of view not correct.

A third possible detachment force is due to the inertia of liquid,  $m_{liq.added}$ , put in motion by the bubble growth, i.e. virtual added mass,  $F_{liq.inertia}$  (Helden 1994; Chen 2002). Depending on whether the bubbles grows in an accelerating manner or a decelerating manner, this added mass force is either a detaching or an attaching force. The forces related to growth in radial direction are not accounted here. A thorough analysis is given in Geld (2000).

$$\begin{aligned} F_{detach} &= F_{buoyancy} + F_{contact.pres} + F_{liq.inertia} \\ &= [\rho_{liq} - \rho_{vap}] g V_{bub} - P_{liq,bot} \frac{\pi D_{contact}^2}{4} + \\ &\quad \sigma \left[ \frac{1}{R_1} + \frac{1}{R_2} \right] \frac{\pi D_{contact}^2}{4} + \\ &\quad \frac{d(m_{liq.added} \frac{dh}{dt})}{dt} \end{aligned} \quad (2.26)$$

The surface tension force,  $F_{surf.tension}$ , is the most obvious force attaching the bubble to the heated surface. It acts on the circumference of the contact area of the growing vapour bubble. Due to the size increase the vapour bubble is subject to a (vertical) drag force,  $F_{vert.drag}$ . Due to the bubble growth, the centre of mass of the bubble accelerates away from the heated surface resulting in a bubble inertia force,  $F_{bubble.inertia}$  (Helden 1994; Chen 2002).

$$\begin{aligned} F_{attach} &= F_{surf.tension} + F_{vert.drag} + F_{bubble.inertia} \\ &= \pi D_c \sigma \sin \theta + c_d \rho_{liq} \frac{\pi}{4} D_{bub}^2 \frac{(\frac{dh}{dt})^2}{2} + \frac{d(m_{vap} \frac{dh}{dt})}{dt} \end{aligned} \quad (2.27)$$

The growing vapour bubble will leave the heated surface if the detaching forces exceed the attaching forces,  $F_{detach} > F_{attach}$ . In case of a slow bubble growth only the surface tension force is of any importance to counteract the three detachment forces. At increased bubble growth rate the vertical drag force gains on importance

as well. The inertia of the vapour inside the bubble remains negligible in most cases, Chen (2002).

### 2.2.3 CONTACT ANGLE

The contact angle has a large influence on the shape of the initial and growing vapour bubble. The contact angle  $\theta$  is defined as the angle at which the liquid-vapour interface meets the solid surface. The angle is measured from the solid surface through the liquid towards the interface, see Figure 2.6.

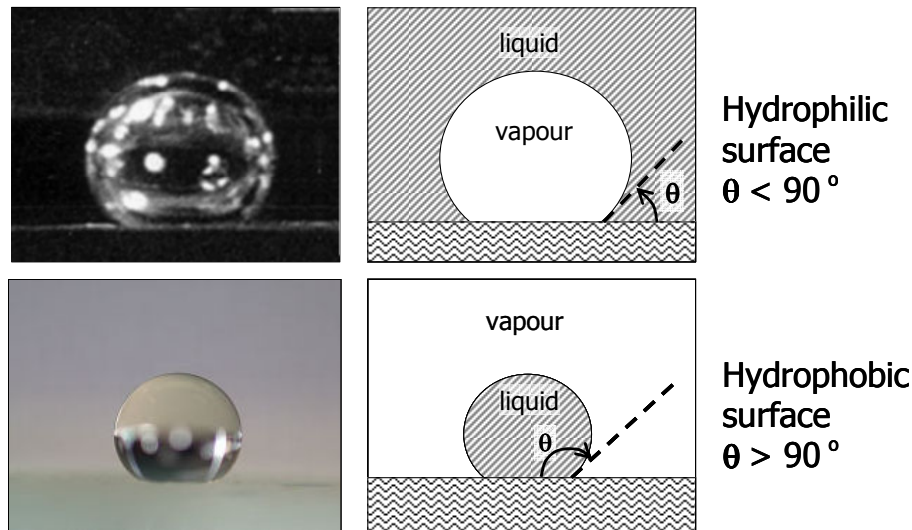


Figure 2.6 – Contact angle of a liquid-vapour interface. Top: a vapour bubble in a hydrophilic system; Bottom: a liquid droplet in a hydrophobic system.

When water has the tendency to form a round droplet on a solid surface, the surface material is said to be hydrophobic since it 'repels' the water by creating a contact angle larger than  $90^\circ$ . Although principally not correct ("*hydro*" is greek for water and "*phobos*" is greek for fear), other liquids than water are sometimes also called hydrophobic, which simply means "having a contact angle larger than  $90^\circ$ ". In case the contact angle is less than  $90^\circ$  the surface is called hydrophilic. As shown in Figure 2.6 hydrophilicity implies that the surface is "*aerophobic*", since the vapour tends to form a spherical bubble. Since it is the surface that is called hydrophobic/hydrophilic, it is principally a property of the surface and not of the liquid.

The contact angle not only depends on the materials, it is also dependent on the movement of the liquid-vapour interface. In case of a non-moving interface, the occurring contact angle is called the static contact angle. In case of a moving interface the contact angle is altered with respect to the static contact angle, and is called the dynamic contact angle. In case the liquid phase moves forward the contact angle is increased. This maximum contact angle is the advancing contact angle. In case the liquid phase moves backward the contact angle is decreased. This minimum contact angle is the receding contact angle. The difference between the advancing and receding contact angle is the contact angle hysteresis.

The shape of the vapour bubble at its incipience influences the onset of nucleate boiling (ONB). Generally, the conditions at the heated surface are such that the

contact angle is not equal to 90° and the initial assumption of a hemispherical bubble needs adjustment (Davis and Anderson, 1966). A hydrophilic surface creates a more complete bubble sphere, with its bubble tip placed further away from the heated surface. Therefore the contact angle dependence is included in equation (2.20) resulting in:

$$q_{ONB}'' = \frac{\lambda_{liq} h_{ev} \rho_{vap}}{8\sigma T_{sat} (1 + \cos \theta)} (T_{wall} - T_{sat})^2 \quad (2.28)$$

The shape of the vapour bubble during its growth influences the bubble departure as well. A hydrophobic heated surface will form rather flat vapour bubbles with a relatively small volume (buoyancy force) compared to the contact line of the liquid-vapour interface (surface tension force). A proper description of the bubble shape is therefore essential for the appropriateness of equations (2.26) and (2.27). The bubble shape has effect on all attachment and detachment forces, either by volume determination ( $F_{buoyancy}$ ,  $F_{liq.inertia}$ ,  $F_{bub.inertia}$ ), curvature determination ( $F_{contact.pres}$ ), diameter determination ( $F_{vert.drag}$ ) and contact area determination ( $F_{surf.tension}$ ,  $F_{contact.pres}$ ,  $F_{buoyancy}$ ) (Chen 2002).

#### 2.2.4 SUBCOOLING OF THE BULK

A liquid may start boiling although the main part of the liquid is not at its saturation temperature. Only a layer of liquid near the heated wall has a temperature high enough to allow the onset of nucleation and the formation of vapour bubbles. This phenomenon is called subcooled boiling (Warrier and Dhir 1999). The subcooling,  $\Delta T_{sub}$ , is defined by the temperature difference between the saturation temperature,  $T_{sat}$ , and the mean temperature of the bulk of the liquid,  $T_{liq}$ :

$$\Delta T_{sub} = T_{sat} - T_{liq} \quad (2.29)$$

The subcooling influences the nucleate boiling heat transfer by the onset of nucleate boiling, bubble behaviour and liquid heat transfer (Basu *et al.* 2005a, b). As visible in Figure 2.4 the temperature of the bulk liquid influences the criteria for ONB. A larger subcooling results in a colder boundary layer which leads to an increased necessary wall superheat for ONB. Under the assumption that the thickness of the thermal boundary layer is not much influenced, the increased temperature difference between the heated surface and liquid bulk results in an increased ONB heat flux as well.

The initiated bubbles will grow in a thermal boundary layer which allows considerable condensation at locations further away from the superheated wall, Steiner *et al.* (2005). The condensation at the bubble tip may balance the evaporation rate near the bubble base. Therefore, the initiated bubbles grow only to a certain size. If this maximum size is below the bubble departure size the bubbles will remain fixed at the

heated surface. However, if this evaporation-condensation balancing bubble size is larger than the bubble departure size, the vapour bubbles will detach into the subcooled bulk flow. The bulk subcooling may cause a collapse of the departed vapour bubble before it reaches the free surface. During the collapse the complete energy of the vapour bubble is absorbed by the bulk liquid.

#### 2.2.5 FORCED CONVECTION

In case a flow is forced over the heated surface the bubble dynamics of nucleate boiling mechanism is affected. The forced convection reduces the thickness of the thermal boundary layer. Therefore, higher wall superheats are required for the onset of nucleate boiling. Likewise, the corresponding heat flux is higher as well. After bubble incipience, the flow around the vapour bubble exerts an additional detachment force on the growing vapour bubble. This additional force decreases the bubble detachment time, which increases the bubble frequency and thus the heat flux from the heated surface into the liquid. Depending on the liquid subcooling, liquid mass flow and supplied energy, various two-phase flow patterns may occur (e.g. Thome 2004; Chen *et al.* 2006).

### **2.3 Pool boiling**

One of the most effective heat transfer mechanisms found in nature is the phase transition of a liquid to its vapour during nucleate pool boiling. For example the boiling of water may result in a heat flux exceeding  $10^6$  W/m<sup>2</sup> with only 20K of temperature difference and almost no flow. To obtain these heat fluxes with radiation at room temperature, a hot object at a temperature of about 2100K is needed. By means of single phase water cooling, a flow of about 300 kg/s is needed on assuming a 0.1 m tube diameter and a 20K temperature difference (Incropera and DeWitt 2002).

Pool boiling is encountered in many applications such as cooling of components, evaporators and home appliances. The boiling process varies considerably depending on the conditions at which the boiling occurs. The thermo-physical properties of the liquid and its respective vapour, the level of applied heat flux, the surface material, its finish and the physical size all may have an effect on the boiling process. Within this section an introduction will be given on pool boiling.

#### 2.3.1 WALL SUPERHEAT

The boiling process is initiated in a liquid if the wall temperature exceeds the saturation temperature of the neighbouring liquid. This excess in wall temperature is called the wall superheat:

$$\Delta T = T_{wall} - T_{sat} \quad (2.30)$$

Due to the pressure dependence of the saturation temperature,  $T_{sat}$ , the boiling behaviour of the fluid depends on the wall superheat,  $\Delta T$ , and not solely on the wall temperature,  $T_{wall}$ . (Rohsenow 1971).

### 2.3.2 POOL BOILING CURVE

Nukiyama (1966) was one of the first to identify various modes in pool boiling. On increasing wall temperatures the boiling passes through different regimes each with its typical behaviour and heat transfer rates. A pool boiling curve has the general shape as given in Figure 2.7.

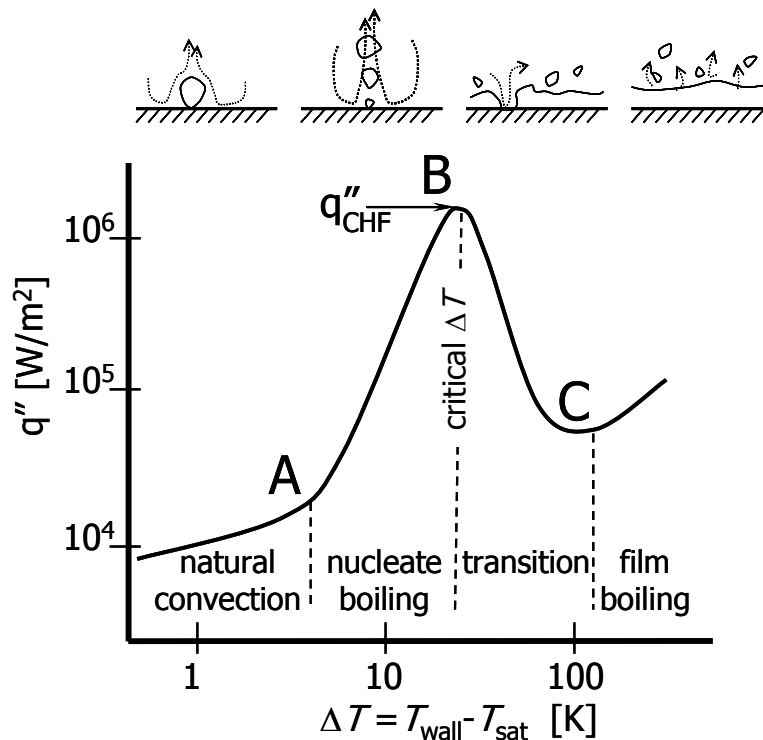


Figure 2.7 – Schematic representation of a pool boiling curve. The horizontal axis contains the temperature difference between the superheated wall and the fluid saturation temperature [K], the wall superheat, and the vertical axis contains the heat flux from the wall to the fluid [W/m<sup>2</sup>]. The values are indicative for water.

For low wall superheats, below point A, little vapour bubbles are present, which only occasionally rise from the heated surface. The heat is mainly transported by natural convection. Beyond this point the nucleate boiling regime starts and vapour bubbles begin to grow and rise. The associated liquid entrainment normal to the heated surface results in an enhanced heat transfer. For increasing wall temperatures, more boiling nuclei are activated, creating more bubbles and therefore rapidly augmenting the heat flux. The curve contains a maximum because it becomes more and more difficult for the liquid to reach the superheated wall if too many bubbles are created. On a further increase of the wall superheat an unstable vapour film is formed isolating the wall from the liquid and diminishing the heat flux. The maximum heat flux (point B in Figure 2.7) is known as the critical heat flux (CHF). For water at atmospheric pressure the critical heat flux is about  $10^6$  W/m<sup>2</sup>, which is one of the highest attainable heat flux values. At wall superheats exceeding point C in Figure 2.7, the vapour film, which withholds the liquid to reach the hot wall, becomes

stable. This behaviour is comparable to the Leidenfrost phenomenon. The subsequent increase in heat flux from the wall towards the fluid can be understood by vapour convection and radiation effects in the vapour film.

For temperature below point B, i.e. the CHF temperature, the boiling process is stable, while between points B and C it is unstable. Below the CHF temperature a disturbance causing a small increase in power input leads to a slightly higher wall temperature. However, the heat transferring capacity from the slightly additionally heated wall towards the fluid increases as well. Therefore, the wall temperature will return to its original value as soon as the disturbance in input power excess has passed. If such a disturbance should happen in the descending part of the boiling curve, the slight increase of power input leads to an increasing wall temperature as well. However, the heat transferring capacity reduces, which results in an even higher wall temperature with again a lower heat transferring capacity. Therefore, the wall temperature will rapidly increase towards the ascending branch of the boiling curve (after point C) and its corresponding heat flux. At CHF this corresponding film boiling temperature is much higher, even causing to possibly melt the boiling structure (also known as the boiling crisis). Under normal circumstances a device is operated in such a manner that the boiling process always remains safely below point B in Figure 2.7 to ensure a stable operation.

### 2.3.3 NUCLEATION SITE DENSITY

During the nucleate boiling process the vapour bubbles arise from fixed positions of the heated wall. All walls made of common materials, which are heated, contain irregularities with gas from which it is possible that a vapour bubble forms. Once such an irregularity facilitated the growth and departure of a vapour bubble, it is likely that a next vapour bubble will incipience at the same location. After bubble departure a little vapour is left behind at the surface, favouring the irregularity for a following bubble incipience. Such a location is called an active nucleation site. Similarly, although the setting is completely different: bare in mind the champagne bubbles rising each time from the same spot.

The number of active nucleation sites depends on various parameters. These parameters are for example the presence of appropriate sites (irregularities), surface wettability, heated wall thermo-physical properties and the wall superheat. In practice only the wall superheat is a parameter in correlations for the nucleation site density,  $N_a$  [ $\#/cm^2$ ] (Dhir 1998)

### 2.3.4 POOL BOILING HEAT TRANSFER MECHANISMS

During nucleate pool boiling various heat transfer mechanisms are occurring. The three most commonly identified mechanisms will be addressed here: Vapour bubble incipience, micro layer evaporation and heated boundary layer mixing.

The creation of a vapour bubble from a small quantity of liquid requires that heat is either extracted from the surrounding liquid or from the heated wall. Due to the latent heat, which is rather large for most fluids, this process may invoke a substantial heat flux from the heated wall towards the fluid.

An estimation based on the energy balance shows that the main heat transfer is not due to energy transport by the primary vapour bubbles and therefore must be transported by the liquid phase. Based on the model of Bowring (1962), we state that the heat transport by the vapour bubbles leaving the active nuclei sites,  $q''_{bubbles}$ , is given by the expression:

$$q''_{bubbles} = \rho_{vap} \cdot V_{bub} \cdot h_{ev} \cdot f \cdot N_a \quad (2.31)$$

where  $V_{bub}$  is the volume of the departing vapour bubble [m<sup>3</sup>] and  $f$  the bubble departure frequency [Hz].

To estimate the highest possible heat flux transported by the vapour bubbles we determined the most favourable value for each variable. The maximum possible departure frequency,  $f$ , is taken equal to the final rise velocity of the vapour bubble,  $u_{bub}$ , divided by the theoretically smallest possible distance between the centres of two rising bubbles, i.e. half the diameter of the first bubble plus half the diameter of the following bubble,  $D_{bub}$ . The final rise velocity of spherical vapour bubbles is given by equating the drag force to the buoyancy force, i.e.

$$c_d \cdot \frac{1}{2} \rho_{liq} u_{bubbles}^2 \cdot \frac{\pi}{4} D_{bub}^2 = \frac{\pi}{6} D_{bub}^3 (\rho_{liq} - \rho_{vap}) g$$

$$\Rightarrow u_{bubbles} = \sqrt{\frac{4 D_{bub} g}{3 c_d}} \quad (2.32)$$

where  $c_d$  the drag coefficient of a rising bubble in a liquid [-]. It is assumed that  $\rho_{liq} \gg \rho_{vap}$ . For a spherical vapour bubble at low Reynolds number the drag force is given by the shape drag only,  $c_d = 16/Re$ , since the shear stresses in the bubble are negligible. For Reynolds numbers within the range  $10^2 - 10^5$  the drag coefficient is approximately constant  $c_d \sim 0.4$ . Thus  $c_d > 0.4$  for  $Re < 10^5$ .

We set the theoretical maximum value for the active nucleation site density,  $N_a$ , to the reciprocal value of the projected area of a single bubble. This leads to the following relation:

$$q''_{bubble, max} = \rho_{vap} \cdot \frac{1}{6} \pi D_{bub}^3 \cdot h_{ev} \cdot \frac{u_{bubbles}}{D_{bub}} \cdot \frac{1}{\frac{\pi}{4} D_{bub}^2}$$

$$= \sqrt{\frac{16 \rho_{vap}^2 g D_{bub} h_{ev}^2}{27 c_d}} \quad (2.33)$$

Using typical values for vapour bubbles in water ( $\rho_{vap} \sim 1 \text{ kg/m}^3$ ,  $h_{ev} \sim 2.26 \text{ MJ/kg}$ ,  $D_{bub} \sim 0.1\text{-}2 \text{ mm}$ ,  $c_d \sim 0.4$ ) the maximum heat flux is estimated to be of the order of

$10^5 \text{ W/m}^2$ . Therefore the highest achievable heat flux transported by vapour bubbles is approximately one order of magnitude less than the measured critical heat flux for water. This indicates that the main heat transport cannot be through the vapour bubbles alone, but primarily through the induced liquid flow.

Micro layer evaporation occurs near the attachment of the vapour bubble to the heated wall. Due to the small dimensions of the bubble attachment layer, large temperature differences occur inside the liquid layer, which implies high heat fluxes. The parameters governing the micro layer evaporation heat flux are the nucleation site density, the vapour bubble diameter, the wall superheat and the thickness of the liquid micro layer and its thermo-physical properties. In case of water these heat fluxes could be theoretically as high as  $1.5 \cdot 10^8 \text{ W/m}^2$  (Lay and Dhir 1994). However, the exact contribution to the total heat flux is difficult to determine, since the actual participating area is unknown and may actually be relatively small. Myers *et al.* (2005) quantifies that not more than 23% of the total heat transfer can be attributed to microlayer evaporation and contact line heat transfer.

The vapour bubble incipience, and the departure from the heated wall, causes the thermal boundary layer to be disrupted. In the wake of the rising vapour bubble hot liquid of the thermal boundary layer is dragged into the colder bulk of the liquid, see Figure 2.8. Due to conservation of mass the departure of the hot liquid must be compensated by a supply of colder liquid from the bulk. This supply of colder liquid can be regarded as cold liquid impinging jets, providing a good heat transfer from the heated wall towards the fluid. These jets reduce the effective thickness of the thermal boundary layer. The more often a vapour bubble is formed and takes off into the bulk liquid, the more often the thermal boundary is disrupted and the thinner it effectively becomes.

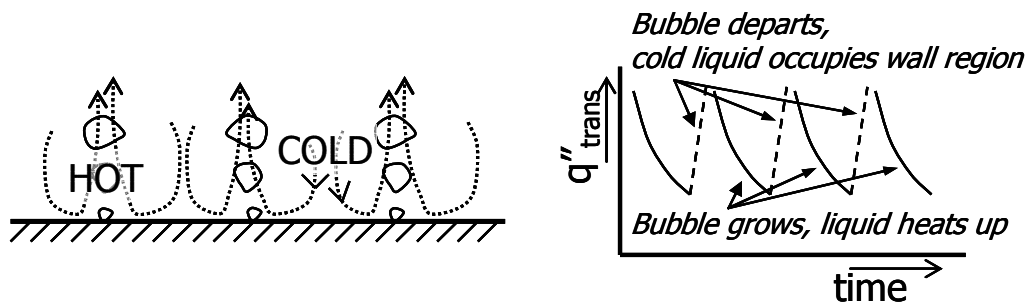


Figure 2.8 – Schematic representation of the transient conduction process induced by the bubble incipience and the departure from the heated wall.

The heat transfer into the replenished liquid near the heated wall can be simplified as a one-dimensional transient conduction process into a semi-infinite medium (Basu *et al.* 2005a). If the bulk liquid temperature is taken as its initial condition and the temperature of the heated surface as its one-sided boundary condition, the transient heat flux can be expressed as:

$$q''_{trans} = \frac{\lambda_{liq} (T_{wall} - T_{liq})}{\sqrt{\pi a_{liq} t}} \quad (2.34)$$

Therefore increasing the departure frequency, and the bubble formation frequency as well, results in a higher nucleate boiling heat transfer. Liquid subcooling increases also the heat transfer, despite the slowing down effect of liquid subcooling on the vapour bubble incipience, which is discussed in section 2.2, on Boiling bubble behaviour.

During the various stages of boiling all the heat transfer mechanisms described above happen simultaneously. Although these heat transfer models combined lead to a better physical understanding of boiling, the practical use of these models is limited. Parameters that are difficult to obtain like the bubble departure frequency, bubble size, thin liquid layer underneath the bubble, etc., are input parameters for these models. The influences of the various heat transfer mechanisms on each mechanism are most often neglected as well. Therefore, in case of designing an actual system engineers rely on empirical correlations.

#### 2.3.5 NUCLEATE BOILING HEAT TRANSFER CORRELATIONS

One of the first engineering correlations on nucleate boiling heat transfer was proposed by Rohsenow (1952). It is able to indicate the heat transfer in a wide range of applications, although it is not based on the actual underlying physics. Only the fluid properties are taken into account using the Bond number, the Prandtl number and the Jakob number, and no boiling system parameters are included, like the surface material and surface roughness. All these external system properties are effectively caught in a single empirical constant.

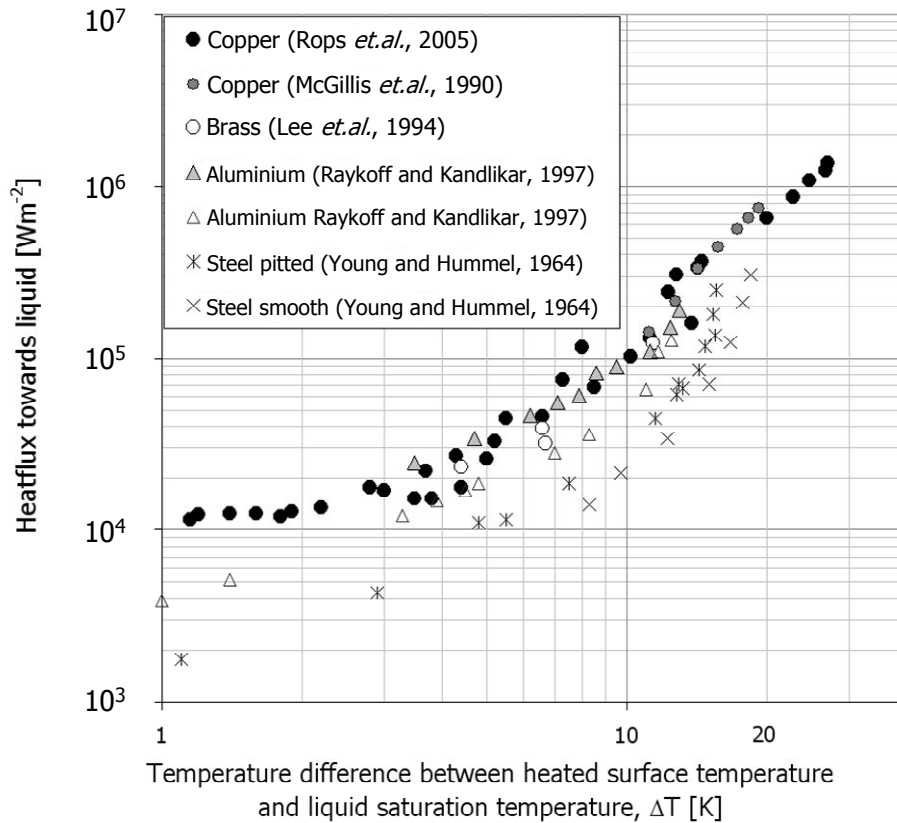


Figure 2.9 – Various measurement results on the pool boiling curve of water using different materials for the heated wall. Rops: Flat plate pool boiling experiments; McGillis: pressure controlled pool flat plate experiments; Lee: pressure controlled flat plate pool boiling experiments; Raykoff: flat plate including cross flow experiments; Young: flat plate pool boiling experiments.

In Figure 2.9 data are displayed of various pool boiling curves of water. This figure shows the influence of various parameters on the boiling curve. A first general trend is visible that at lower thermal conductivities of the heated wall material the boiling curve start to rise later, but steeper. Furthermore some influence of the surface condition (Young and Hummel 1964) and of the flow condition (Raykoff and Kandlikar 1997) are visible.

Numerous engineering relations by many researches have been developed to include these external system properties. Piore *et al.* (2004) has compared some of the most commonly used engineering relations. From this study Piore *et al.* (2004) proposed that if the exact situation is not known the 'old' Kutateladze correlation (Kutateladze and Borishanskii, 1966) is a good alternative. This correlation is given by:

$$h_{nb} = \frac{\lambda_{liq}}{D} \cdot 0.44 \left( \frac{0.0001 \cdot P \cdot q''}{g \cdot h_{ev} \cdot \rho_{vap} \cdot \mu_{liq}} \frac{\rho_{liq}}{\rho_{liq} - \rho_{vap}} \right)^{0.7} \left( \frac{C_p \mu_{liq}}{\lambda_{liq}} \right)^{0.33} \quad (2.35)$$

Another general expression for the heat transfer in nucleate boiling is proposed by Mostinski (1963). His dimensionally reduced pressure (the correlation must be used

with the pressure,  $P_r$  and the critical pressure,  $P_{crit}$ , in bar) gives the nucleate boiling heat transfer coefficient,  $h_{nb}$ , in  $W/m^2K$  :

$$h_{nb} = 2.54 \cdot A^* \cdot F(P_r) \cdot (q''_{nb})^{0.7} \quad (2.36)$$

in which:

$$A^* = 0.00658 \left( \frac{P_{crit}}{0.072} \right)^{0.69} \quad (2.37)$$

$$F(P_r) = 1.8 \cdot P_r^{0.17} + 4 \cdot P_r^{1.2} \quad \text{with : } P_r = \frac{P}{P_{crit}}$$

This relation includes the pressure dependence of the boiling curve as well, but it incorporates no underlying physical mechanism, by means of dimensionless numbers, at all. Despite this lack of physical input, this engineering relation is found to give the best agreement with the measurements obtained in the present work, see Figure 2.10.

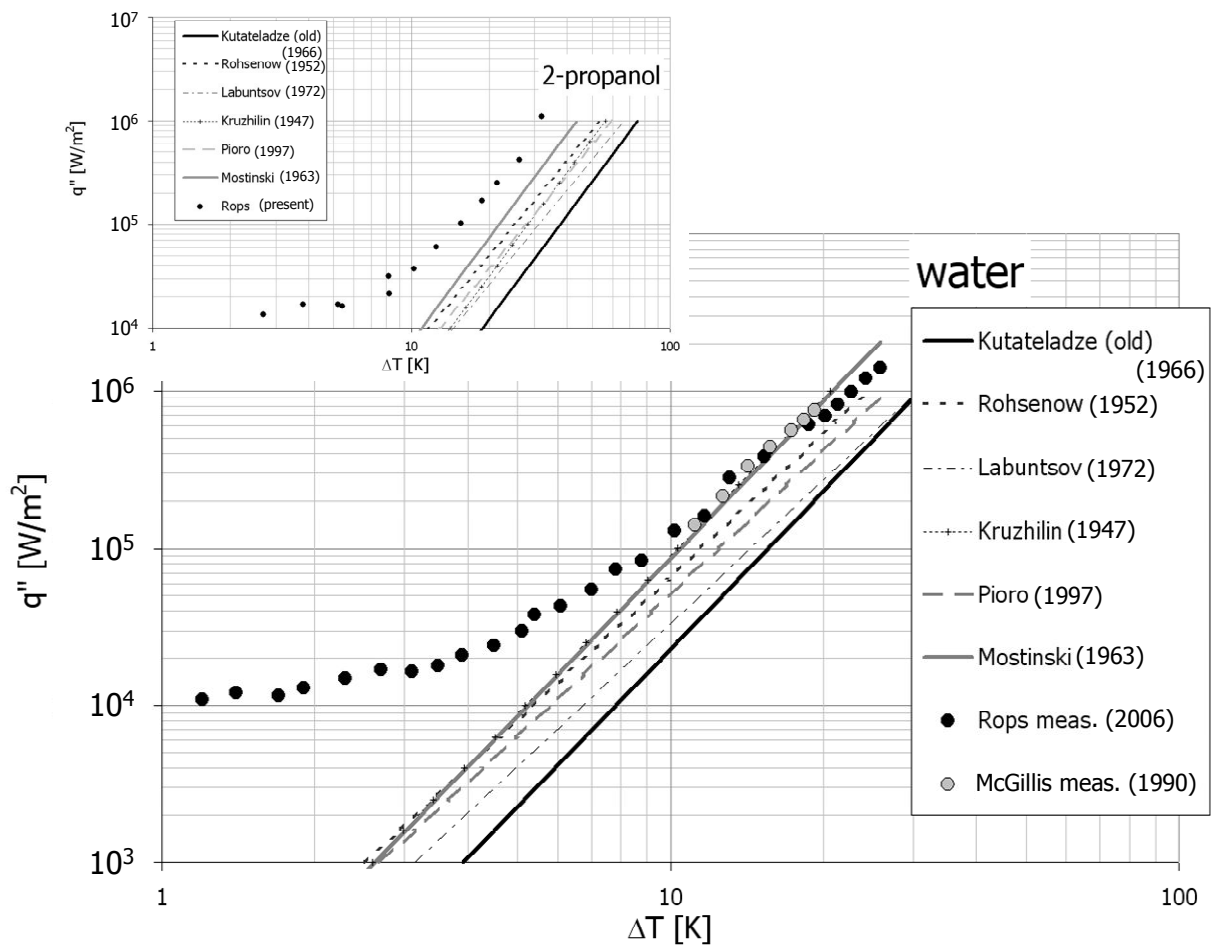


Figure 2.10 - Comparison of the various boiling models with the present measurement results for water (unconfined boiling) and 2-propanol (unconfined boiling). Equation (2.35) is the "Kutaladze

(old)" model and Equation (2.36) is referred to as "Mostinski". Rohsenow (1952); Labuntsov (1972); Kruzhilin (1947); Piro (1997) .

### 2.3.6 CRITICAL HEAT FLUX CORRELATIONS

The mechanism leading to the departure of the nucleate boiling heat transfer into the boiling crisis is up to now not fully understood. The dense distribution of active nuclei forcing the liquid away from the heated wall and the non-wetting tendency of the heated surface are suggested to play a role in the process. The critical heat flux occurs at the point of onset of a hydrodynamic instability. Zuber (1958) was one of the first to explain this.

Zuber (1958) proposed that the liquid-vapour interfaces suffers from a Helmholtz instability at the point of the critical heat flux. At this point the vapour velocity flowing parallel to the interface reaches some critical value, allowing a small perturbation to grow despite the attenuating interfacial surface tension. Zuber also assumed that the distance between the vapour jets is bounded by the "critical" two-dimensional Taylor wavelength. This leads to the following expression (Zuber, 1958):

$$q''_{CHF} = C \cdot \rho_{vap} \cdot h_{ev} \left( \frac{\sigma g (\rho_{liq} - \rho_{vap})}{\rho_{vap}^2} \right)^{1/4} \quad (2.38)$$

The constant, C, equals  $\pi/24$  in Zuber's analysis. A dimensional analysis leads to a similar expression (Kutateladze 1948) and after a comparison to experimental data the constant C was set to the empirical value of 0.168 in case of an upward facing heated wall.

Several system variables affect the value of the critical heat flux: the heated wall geometry, orientation, material, wettability, gravity, system pressure, flow velocity and liquid subcooling. Zuber *et al.* (1961) extended their critical heat flux equation to moderate subcooled liquids by accounting for transient heat losses to the liquid. This is given by the following expression:

$$\frac{q''_{CHF,subcooled}}{q''_{CHF,saturated}} = 1 + \frac{5.3}{\rho_{vap} h_{ev}} \cdot (\lambda_{liq} \rho_{liq} C_{p,liq})^{1/2} \cdot \left( \frac{\sigma g (\rho_{liq} - \rho_{vap})}{\rho_{vap}^2} \right)^{-1/8} \cdot \left( \frac{g (\rho_{liq} - \rho_{vap})}{\sigma} \right)^{1/4} (T_{sat} - T_{liq}) \quad (2.39)$$

In case of water, equation (2.39) reduces to:

$$\frac{q''_{CHF,subcooled}}{q''_{CHF,saturated}} = 1 + 0.05 \cdot (T_{sat} - T_{liq}) \quad (2.40)$$

So it can be concluded that a liquid subcooling of 20K doubles the critical heat flux value for saturated pool boiling,  $q''_{CHF,saturated}$ .

## **2.4 Boiling within channels**

Flow boiling can be divided into two classes: internal flow boiling (boiling characteristics influenced by external size) and external flow boiling (boiling characteristics not influenced by external size). Internal flow boiling has been extensively studied because of the need for understanding the cooling limits of nuclear reactor cores and steam generators. For external flow boiling the geometries that are studied most often are those of a liquid jet impinging on a horizontal surface (e.g. metal quenching) and of flow normal to a horizontal cylinder (e.g. refrigerant flooded evaporators and thermosyphon reboiler) (Thome 2004).

This thesis only considers internal flow boiling within small diameter channels. Therefore, in this section the emphasis is on existing knowledge on internal flow boiling.

### 2.4.1 FLOW BOILING MAP

In pool boiling the heat transfer from the heated surface towards the liquid is a strong function of the heat flux, by about  $h_{nb} \sim (q'')^{0.7}$ , see section 2.3.5. Instead, the heat transfer for boiling within channels is a strong function on its local vapour quality,  $x$ , and the mass flux,  $G$ . Therefore both the nucleate boiling heat transfer and the convective heat transfer must be taken into account. In general the following hydro-dynamical states are encountered during boiling inside channels, see Figure 2.11.

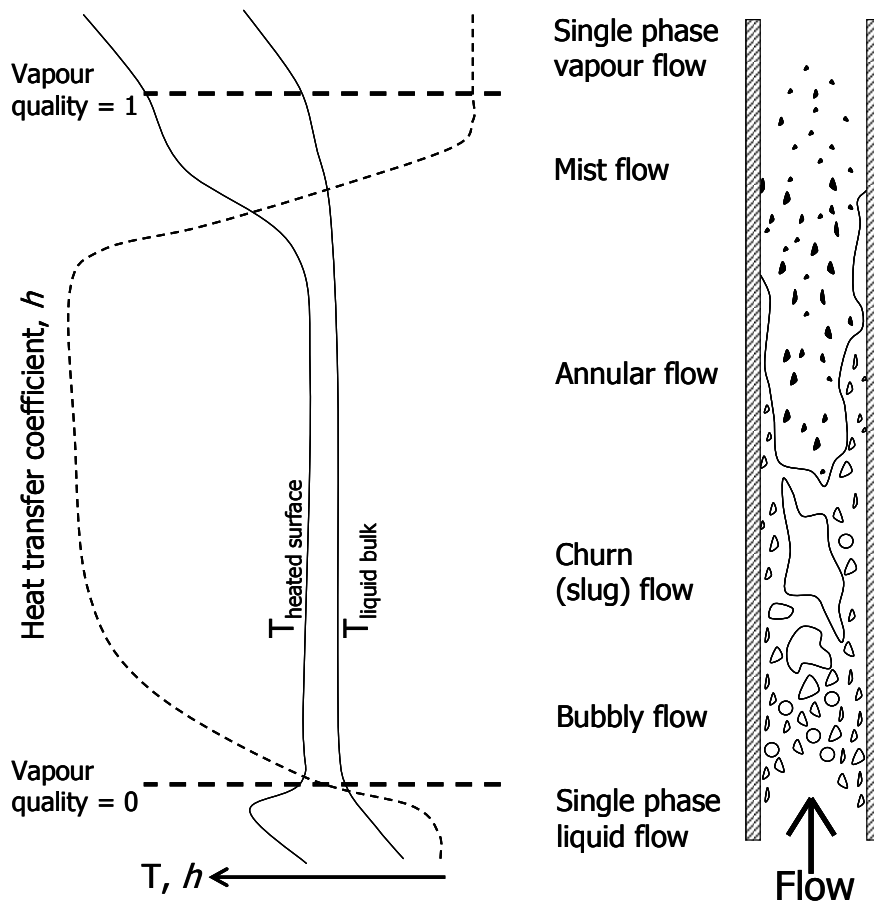


Figure 2.11 – Heat transfer regions encountered during convective boiling within channels. On the left the typical temperature profiles are shown in case of a uniform heat load along the boiling channel. After Thome (2004).

In Figure 2.11 a large diameter vertical pipe is chosen for illustration purposes. Consider a uniformly heated channel with a subcooled liquid entering at a constant mass flow rate. At the end of the channel the liquid has evaporated completely. When the liquid enters the channel it is below the liquid saturation temperature (and so is possibly the channel wall). The wall temperature rises more quickly than the liquid, and from a certain point on it exceeds the liquid saturation temperature. In this region subcooled single phase heat transfer takes place. This may be followed by subcooled flow boiling if the temperature of the channel wall becomes high enough to allow ONB and vapour bubble departure. The formation of vapour bubbles leads to a significant increase of the heat transfer. After the onset of significant void, OSV, first a bubbly flow region in the channel can be observed. In practice the liquid bulk is by then no longer subcooled. The heat is now transported from the heated channel wall by convective, saturated nucleate boiling. Moving through slug, churn and annular flow (see section 2.1.6 on Two-phase flow pattern map) the void fraction is increased and the saturated nucleate boiling heat transfer is taken over by forced convective heat transfer through a liquid film. As the annular liquid film thickness decreases, possible dry spots on the channel wall begin to occur, soon followed by complete 'dryout'. At the dryout point no liquid is attached to the channel wall and only droplets sheared from the wall form a mist flow. The 'dryout' region is typically characterised by a sharp increase of the channel wall temperature, due to the poor heat transfer. The heat transfer within this region is via four mechanisms: single

phase convection heat transfer to the vapour, heat transfer from the vapour to the droplets, heat transfer by impinging droplets heat transfer on the wall and thermal radiation heat transfer. Because of the non-equilibrium effect, droplets may continue to exist in the vapour phase beyond the point of unit vapour quality,  $x = 1$ . The equilibrium vapour quality  $x$  is defined by the enthalpy excess of the two-phase mixture with respect to its liquid state, divided by the evaporation enthalpy (e.g. Thome, 2004).

$$x = \frac{E_{tot} - E_{liq}}{m_{tot} h_{evap}} \quad (2.41)$$

When all droplets have evaporated the heat transfer is by single-phase convection to the dry vapour, see Figure 2.11.

#### 2.4.2 FLOW BOILING HEAT TRANSFER MECHANISMS

During flow boiling various mechanisms are responsible for the heat transfer: first, the single phase forced convection, second, the heat transfer due to the vapour bubbles breaking up the thermal boundary layer (comparable with the transient heat transfer within pool boiling), and third, the evaporation at the liquid-vapour interface (Basu *et al.* 2005a).

Single phase forced convection occurs during the time in between the initiation of two adjacent vapour bubbles of an active nucleation site, as the liquid flows over the heated channel wall. In principle this single phase heat transfer can be compared with the common forced convection heat transfer of a liquid. Therefore, in most flow boiling models textbook correlations on forced convection are used to calculate this contribution to the heat transfer (Thome 2004).

The second heat transfer mechanism occurs due to the departure of the vapour bubbles from the heated channel: hot liquid is dragged into the bulk of the flow where it mixes with the cooler bulk liquid. The displacement of the vapour bubble causes fresh liquid from the bulk to occupy the vacated bubble volume near the heated channel wall. The heat flux into the refreshed liquid can be regarded as a transient conduction process, with a heat transfer given by the model of equation (2.34) in the section on Pool boiling heat transfer mechanisms. An increased bubble departure frequency leads to a higher liquid refreshment rate and thus a higher time averaged heat transfer, see Figure 2.12).

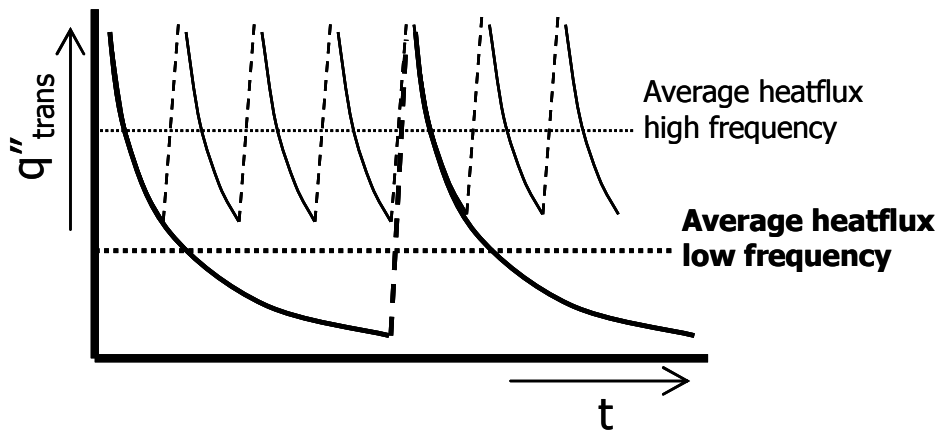


Figure 2.12 – Schematic representation of the average transient heat transfer increase due to a liquid refreshment frequency increase. On the horizontal axis the time is given and on the vertical axis the transient heat transfer, equation (2.34).

Evaporation and condensation on the liquid-vapour interface is the third heat transfer mechanism during subcooled nucleate flow boiling. This type of heat transfer may be compared to the heat transfer mechanism applied in heat pipes (Thome 2004). Near the heated channel wall, which is the hot side of the vapour bubble, liquid evaporates. Closer to the bulk, which is the cold side of the vapour bubble, vapour condensates. The same reasoning holds if the vapour bubble detaches and enters the bulk of the liquid where it may condensate.

The bulk mass flow velocity influences in several ways the transient heat transfer. Most obviously, a higher mass flow velocity increases the detachment force on the vapour bubble which leads to an earlier departure of the vapour bubble. Also, a higher mass flow rate has a larger capacity to receive heat and therefore the liquid subcooling is maintained better. The liquid subcooling increases the transient heat flux as well, see equation (2.34). On the other hand, the liquid subcooling slows down the vapour bubble incipience (see section 2.2.4), which reduces the vapour bubble departure frequency and which has a negative effect on the transient heat flux. Vapour bubbles sliding along the wall, vapour bubble coalescence, and possible vapour film initiation are just some examples of the void fraction interaction on the heat transfer.

The above shows the complexity of the various mechanisms affected by the two main parameters, i.e. mass flow velocity and void fraction.

### 2.4.3 FLOW BOILING HEAT TRANSFER CORRELATIONS

Flow boiling models usually consider two heat transfer coefficients (e.g. Schlünder *et al.* 1994; Thome 2004): the nucleate flow boiling heat transfer coefficient,  $h_{nfb}$ , and the convective flow boiling heat transfer coefficient,  $h_{cfb}$ . The nucleate boiling heat transfer coefficient,  $h_{nfb}$ , is considered to be similar to the one of the nucleate pool boiling, except for the influence of the bulk flow and the bubble induced convection effects (see the previous section on Flow boiling heat transfer mechanisms). The convective flow boiling coefficient,  $h_{cfb}$ , is dominated by the convective process in a thin liquid film flowing along a heated wall. This mechanism plays an important role at high void fractions in the presence of an annular flow without nucleate boiling in

the liquid film. The total two-phase flow boiling heat transfer coefficient,  $h_{fb}$ , is usually obtained by adding up the two heat transfer coefficients using a power law addition (Thome, 2004):

$$h_{fb} = \left[ (h_{nfb})^n + (h_{cfb})^n \right]^{1/n} \quad (2.42)$$

The value of  $n$  determines the smoothing in the transition between the two heat transfer mechanisms. In practice values like 1 (i.e. simple addition), 2, 3 and  $\infty$  (i.e. only the largest one is taken) are chosen in flow boiling heat transfer correlations.

Chen (1963) was one of the first to propose a flow boiling heat transfer correlation for vertical tubes. He simply added (i.e.  $n = 1$ ) a nucleate flow boiling coefficient,  $h_{nfb}$ , and a convective flow boiling coefficient,  $h_{cfb}$ , to obtain a total local flow boiling heat transfer coefficient. For both heat transfer coefficients he simply used known relations for nucleate pool boiling and single phase forced convection. To include the aspect of flow boiling, suppression and multiplication factors for the two mechanisms were introduced:

$$h_{fb\_chen} = C_1 \cdot h_{nfb} + C_2 \cdot h_{cfb} \quad (2.43)$$

Chen (1963) used the dimensional relation given by Forster and Zuber (1955) for nucleate pool boiling:

$$h_{nfb} = h_{nb\_FZ} = 0.00122 \left[ \frac{\lambda_{liq}^{0.79} c_p^{0.45} \rho_{liq}^{0.49}}{\sigma^{0.50} \mu_{liq}^{0.29} h_{ev}^{0.24} \rho_{vap}^{0.24}} \right]^{0.24} \Delta P^{0.24} \Delta T^{0.75} \quad (2.44)$$

In equation (2.44) the term  $\Delta P$  is the pressure difference between the vapour pressure of the liquid near the wall and the liquid vapour pressure at saturation temperature, which is similar to the term  $\Delta T$ , see eq. (2.30). All units must be SI-units, thus  $\Delta P$  is denoted in  $N/m^2$ .

The convective flow boiling coefficient,  $h_{cfb}$ , Chen (1963) used the Dittus-Boelter (1930) correlation:

$$h_{cfb} = h_{DB} = 0.023 \cdot Re_{liq}^{0.8} \cdot Pr_{liq}^{0.4} \cdot \left( \frac{\lambda_{liq}}{D_h} \right) \quad (2.45)$$

For the Reynolds number ( $Re_{liq}$ ) and Prandtl number ( $Pr_{liq}$ ) Chen (1963) used the superficial liquid velocity and the properties of the liquid phase only. Note that in a flow boiling channel the superficial liquid velocity is a function of the vapour quality.

The multiplier  $C_2$  in front of the convective flow boiling term is a function of the Martinelli constant (see section 2.1.4),  $X_{tt}$ , (with  $n_1=0.9$ ,  $n_2=0.5$  and  $n_3=0.1$ ):

$$C_2 = \left( \frac{1}{X_{tt}} + 0.213 \right)^{0.736} \quad (2.46)$$

and the nucleate flow boiling factor  $C_1$  equals:

$$C_1 = \frac{1}{1 + 2.53 \cdot 10^{-6} \cdot C_2^{1.46} \cdot \text{Re}_{liq}^{1.17}} \quad (2.47)$$

Like the correlations given by Chen (1963), many others (e.g. Shah 1982; Gungor and Winterton 1986; Kandlikar 1990) have formulated flow boiling relations. Due to the complexity of interacting physical phenomena, most of them are mainly empirical using both dimensionless as dimensional numbers like Chen's correlation.

## 2.5 Summary

The most commonly used two-phase flow concepts are introduced, such as the void fraction, superficial velocity, and two-phase flow pattern map. In literature an alteration in two-phase flow pattern map is observed on reducing the channel diameter. Most noticeable, no horizontally stratified flow occurs in concurrent two-phase flow in horizontal small diameter channels. In case of theoretical models to predict the transition lines in between the various patterns, stratified flow is regarded to be the base state. Only three anchor flow regimes are identified: bubble flow, slug flow, and annular flow.

Textbook knowledge and the state of the art insights are presented on boiling bubble behaviour, nucleate pool boiling, and flow boiling. The various heat transfer mechanisms during nucleate boiling are described :

1. the heat transfer due to the latent heat,
2. transient heat transfer due to the mixing of the heated boundary layer.

The interactions of the heat transfer mechanisms and their relative importance are addressed as well.

# 3 Air-water two-phase flow

## 3.1 Present status

The data for the mapping of two-phase flow regimes is extensive on channels with a 'large' diameter, i.e.  $Co < 0.5$ . However, with the emerging research field of microfluidics and its applications, 'small' diameter channels, characterised by  $Co > 0.5$ , have been investigated as well. Therefore, before presenting the present results, a short overview on these findings will be given first.

### 3.1.1 WAMBSGANSS ET AL.

Wambsganss *et al.* (1991) studied two-phase flow behaviour in a horizontal rectangular PMMA channel ( $19.05 \times 3.18 \text{ mm}^2$ ) with a hydraulic diameter of 5.45mm. This channel size is at the upper boundary of the transition region from large-diameter channels to small-diameter channels ( $Co = 0.5$ ). The air-water flow patterns are determined over a large range of total mass flux ( $50\text{-}2000 \text{ kg/m}^2\text{s}$ ) which includes all two-phase flow patterns typically found in larger channels, see section 2.1.6. Along the channel pressure transducers are placed to measure pressure drops. The axial location at which the observations are done is 153 times the hydraulic diameter downstream from where the air and water flows are merged. Wambsganss *et al.* (1991) identified the bubble/plug-to-slug transitions by visual observation and by the abrupt rise in pressure drop while increasing the vapour quality. The slug-to-annular transition is marked by a diminishing pressure drop. From visual observation the slug-to-annular transition is difficult to distinguish since it is more gradual than the other transitions.

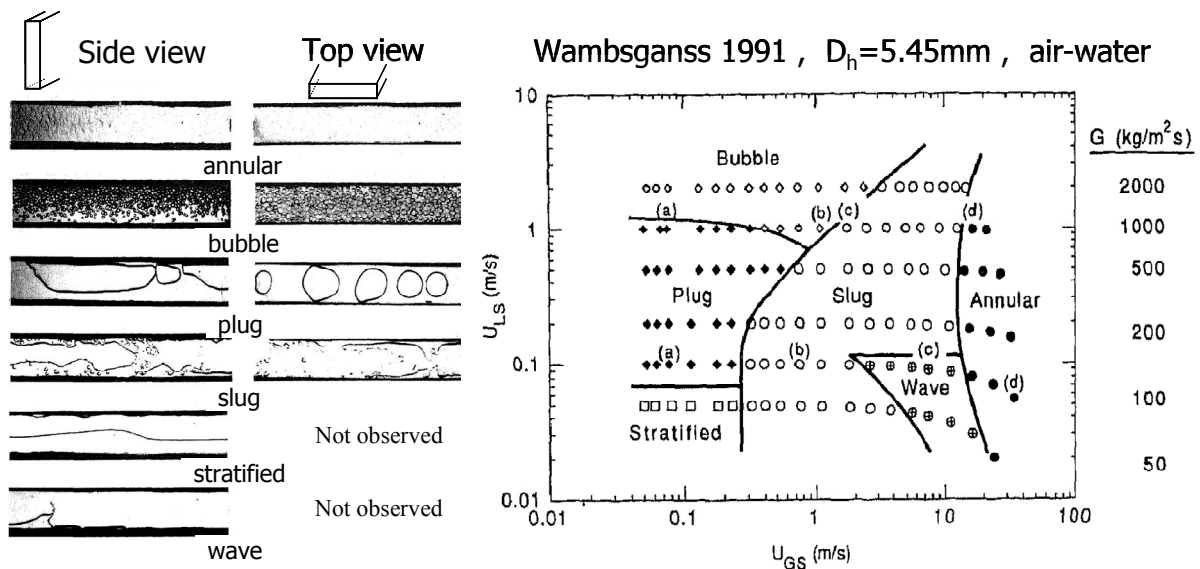


Figure 3.1 – Two-phase flow pattern examples as shown by Wambsganss *et al.* (1991). The two-phase flow pattern map is given for the upright position of the horizontal channel (side view).

The two-phase flow pattern examples, as given by Wambsganss *et al.* (1991) (Figure 3.1), show still some gravity effects in the channel in upright position (observed by side view). The occurrence of the stratified and wave flow regime and the flow of bubbles at the upper side of the channel during bubbly flow are its clear indicators.

In the position with the widest side down, the so called lying position, (observed by top view) none of these indicators are present. The two-phase flow pattern map for this configuration is given in Figure 3.2.

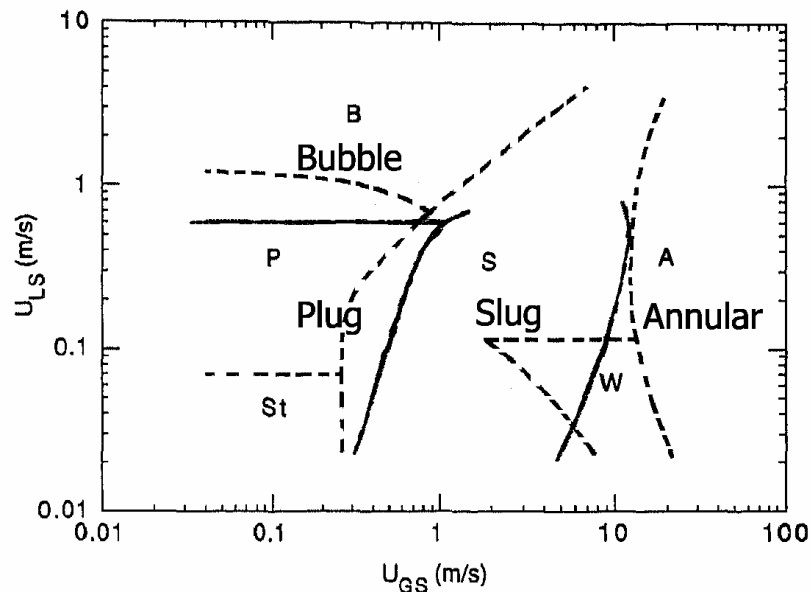


Figure 3.2 – Two-phase flow pattern map measured by from Wambsganss *et al.* (1991),  $D_h=5.45$  mm. Horizontal rectangular channel (aspect ratio 1:6) in lying position. Solid lines: lying position; Dashed lines: upright position. – pattern definitions are given in Figure 3.1 –

In the research their findings are compared with other two-phase flow pattern maps on both large diameter channels and round channels with similar hydraulic diameter. Only the upright channel showed general agreement to the large size channels pattern maps, while the lying channel showed qualitative agreement with the small sized round channels.

### 3.1.2 CHUNG AND KAWAJI

The effect of the channel diameter on adiabatic two-phase flow (nitrogen – water) in micro channels was investigated by Chung and Kawaji (2004). Their experiments are conducted in circular channels, which are made of fused silica with standard polyimide coating. The investigated channel diameters are 530, 250, 100 and 50  $\mu\text{m}$ . They observe two-phase flow patterns of typical small diameter ( $\sim 1\text{mm}$ ) channels for the 530 and 250  $\mu\text{m}$  diameter channels. In the 100 and 50  $\mu\text{m}$  channels, they report a departure from the typical small diameter two-phase flow behaviour. A new two-phase flow pattern consisting of a serpentine gas core (ring flow) is defined to characterise their observations.

In their experiments the gas and the liquid are driven by a pressurised vessel through a horizontal micro mixing channel. The long observation channels (with a length of  $\sim 500\text{-}1000$  times the (hydraulic) diameter) with the various diameters are attached to this mixing channel. Pressure transducers are connected to measure the pressure drop between the channel inlet and outlet for two-phase flow. Notion is made of the occurrence of more than one two-phase flow pattern for a given flow condition at the same location of the channel.

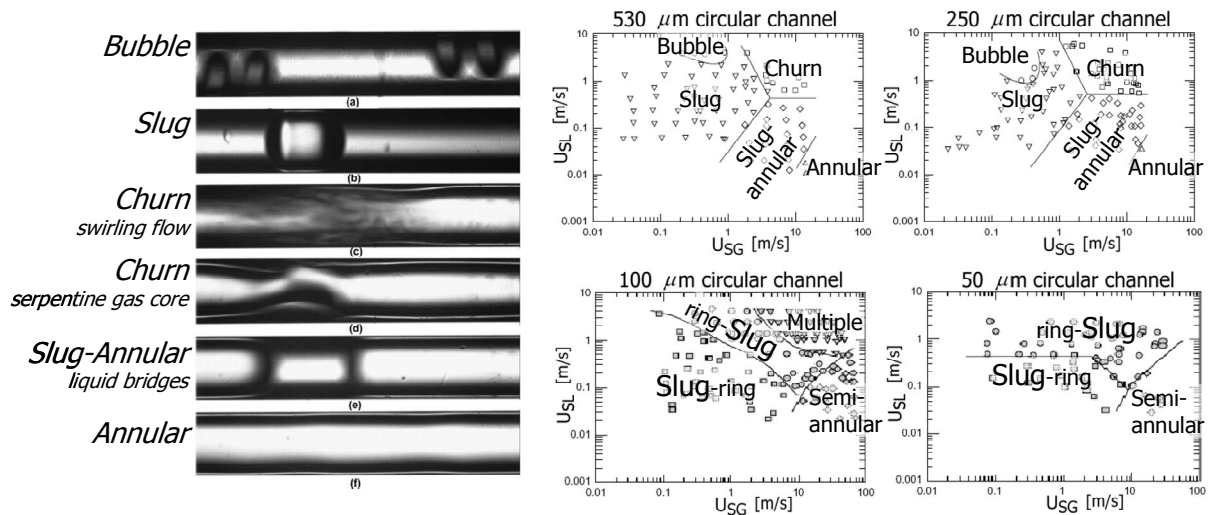


Figure 3.3 - Two-phase flow pattern examples and the two-phase flow pattern maps as given by Chung for the four different channel diameters.

Figure 3.3 shows the two-phase flow patterns as defined by Chung and Kawaji (2004) for small diameter channels. The definition of the ring-flow pattern is rather similar to the annular-churn flow (defined by Kawahara *et al.*, 2002). Therefore, the two-phase flow pattern “slug-ring” and “ring-slug” may be regarded as either slug flow or its transition from slug towards annular flow. Figure 3.4 shows the transition lines for four channel diameters placed in one map.

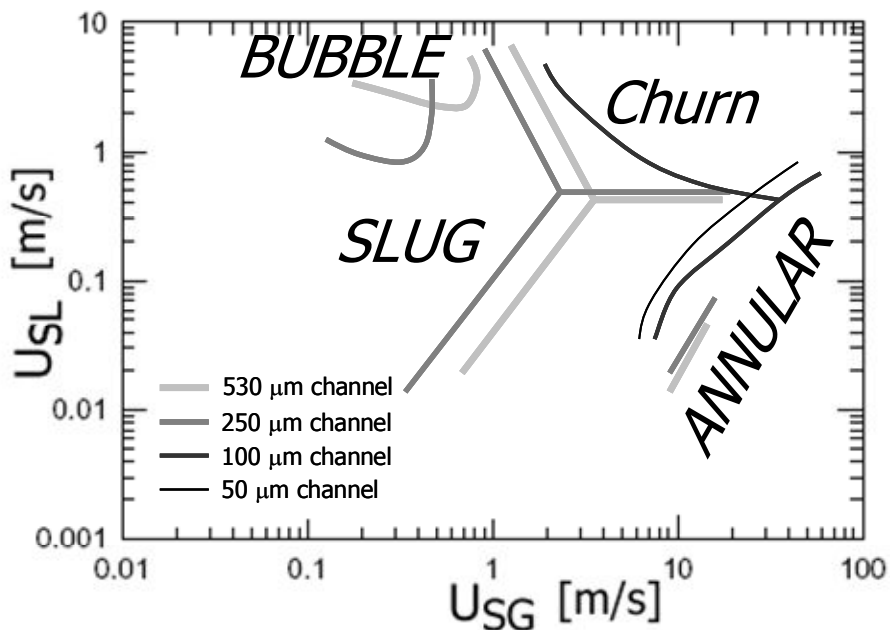


Figure 3.4 – The transition lines of four two-phase flow pattern maps data taken from Chung and Kawaji (2004) for channel diameters: 530  $\mu\text{m}$ , 250  $\mu\text{m}$ , 100  $\mu\text{m}$  and 50  $\mu\text{m}$  – pattern definitions as in Figure 3.3 –.

On displaying the transition lines of all four channel diameters in one map the annular flow transition lines roughly correspond in all four channels diameters. The same correspondence may be observed for the churn (or multiple patterns) flow. For the two smallest channels no bubbly flow is reported, indicating a dominance in slug flow occurrence.

Void fraction estimations are made for all four channel diameters. The image analysis is performed on 200-500 video images in each run. In case of the 530 and 250  $\mu\text{m}$  channels they find a linear relation between the volumetric quality and the void fraction. The linearity implies that the velocity ratio,  $S$ , is constant. For their case the velocity ratio is either unity (homogeneous approach) or 0.8 (as suggested by Ali *et al.*, 1993). In case of the two smallest diameters, 100 and 50  $\mu\text{m}$ , Chung and Kawaji (2004) report measurement of low void fraction at low vapour qualities and an exponential behaviour at vapour qualities higher than 0.8. The lower void fraction measurement at low vapour qualities indicates a larger velocity slip ratio and thus a weaker momentum coupling between the gas and the liquid phases. Chung and Kawaji (2004) give the following explanation for this behaviour: In a micro channel, between volumetric qualities of 0 and 0.8, the void fraction data fall below traditional correlations developed for small diameter channels due to the occurrence of short and long liquid slugs. The increased pressure gradient over long liquid slugs causes the short slug bubbles to accelerate, and thus evade capture by the video camera. At the higher volumetric qualities the gas volume is much higher in the micro channel, which reduces this effect. Their explanation may also clarify the disappearance of the bubble region.

### 3.1.3 ZHAO AND BI

Two-phase flow pattern characteristics were investigated experimentally by Zhao and Bi (2001) in three vertical equilateral triangular channels (PMMA) with hydraulic diameters of 2.886 mm, 1.443 mm and 0.886 mm. Upstream and downstream pressure taps are installed to estimate the two-phase pressure drop. Using high-speed visualisations typical small diameter two-phase flow patterns were identified.

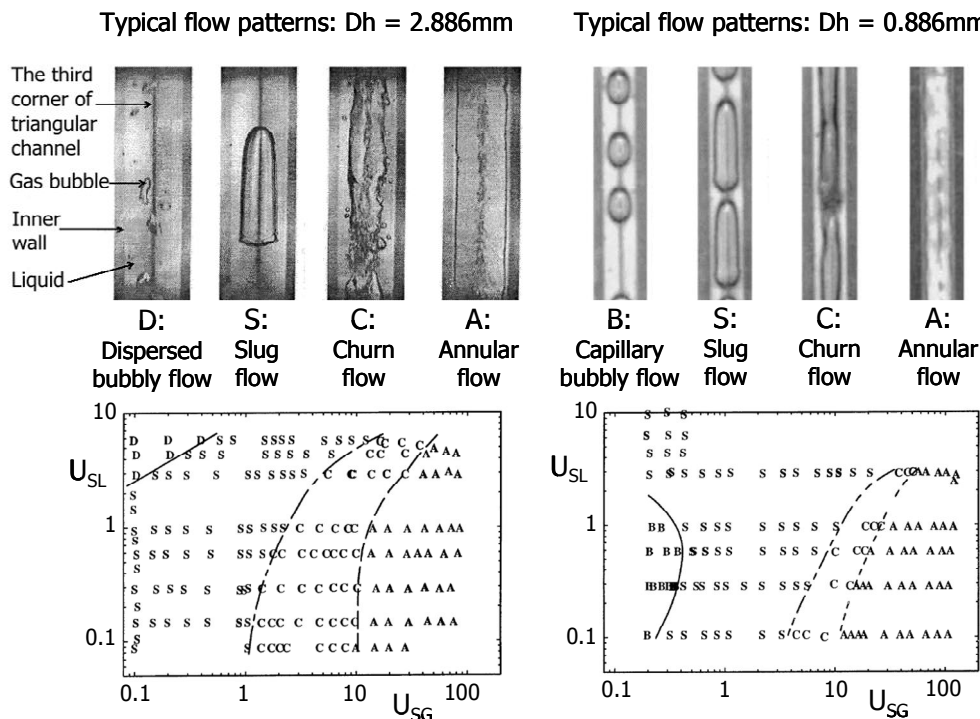


Figure 3.5 – Examples of two-phase flow pattern and two two-phase flow pattern maps as given by Zhao and Bi (2001). Left: triangular channel with hydraulic diameter equal to 2.886mm; Right: triangular channel with hydraulic diameter equal to 0.886mm;

The two-phase flow pattern examples given in Figure 3.5 show that the bubbly flow behaviour of the 0.886 mm channel is different from the triangular channels with larger hydraulic diameters considered in this work (2.886 mm and 1.443 mm). The bubbly flow for the smallest channel diameter consists of a single bubble train while the larger channels contain a randomly dispersed flow of bubbles. Secondly, the bubbly flow pattern occurs at low gas and liquid flows in the 0.886 mm channel, while the dispersed bubble flow appears at rather high liquid flows for the larger channels. Plotting all two-phase pattern maps together in one figure, see Figure 3.6, shows that the annular flow transition line shifts only slightly to higher superficial gas velocities on decreasing hydraulic diameter. In case of the smallest channel the transition region from slug to annular flow, churn flow, is narrowed, due to a widening of the slug flow region.

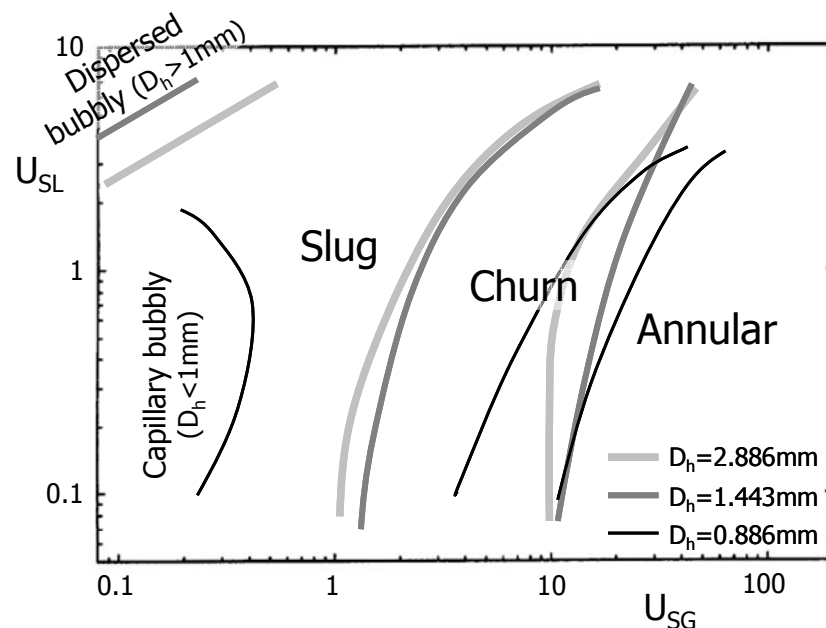


Figure 3.6 – The transition lines of two-phase flow pattern maps data taken from Zhao and Bi (2001) for three triangular channels with different hydraulic diameter: 2.886 mm, 1.443 mm and 0.886 mm.

Comparison of their experimental results with analytical models like Taitel *et al.* (1980) shows a qualitative agreement for the churn to annular flow transition. A poor prediction is found for the transition lines between the other two-phase flow patterns.

#### 3.1.4 TABATABAI AND FAGHRI

In case of large diameter channels ( $Co < 0.5$ ) many models are proposed predicting the transition lines from one two-phase flow pattern to another. These models are most commonly based on momentum balances and apply Kelvin-Helmholtz theory to deduce transition criteria. Surface tension effects are not taken into account resulting in considerable errors for tubes of smaller diameters, where surface tension plays an important role ( $Co > 0.5$ ). Horizontally stratified flow is assumed as the initial two-phase flow pattern from which the disturbance develops.

Tabatabai and Faghri (2001) propose a two-phase flow pattern model which includes the surface tension effects in case this is necessary. Therefore, first the relative effect of surface tension forces compared to shear forces has to be determined. Next, their model aims on determining the effects of the surface tension on the various flow regimes.

Tabatabai and Faghri (2001) estimated the pressure losses due to the shear forces assuming two contributions: the pressure drop of the gas flow as if no liquid phase were present, eq.(3.1), and the pressure drop of the liquid flow as if no gas phase were present, eq.(3.2):

$$-\left. \frac{dP}{dz} \right|_{gas} = \frac{2f_{gas}G_{gas}^2}{D_h \rho_{gas}} \quad (3.1)$$

$$-\left. \frac{dP}{dz} \right|_{liq} = \frac{2f_{liq}G_{liq}^2}{D_h \rho_{liq}} \quad (3.2)$$

Where  $f$  is the Fanning friction factor [-] and  $G$  is the mass flux [kg/m<sup>2</sup>s].

The pressure drop due to the shear is the sum of shear pressure drop terms for both gas and liquid phases. The pressure drop due to surface tension forces,  $\Delta P_{surf}$ , is estimated using the Young-Laplace equation:

$$\Delta P_{surf} = \frac{2\sigma}{r_{eff}} \quad (3.3)$$

Where  $r_{eff}$  is the effective radius of the gas/liquid interface. Tabatabai and Faghri (2001) proposes the hydraulic gas diameter,  $D_{h\_gas}$ , divided by two as an approximation for the effective radius for the two-phase flow. The cross-sectional gas flow area ( $=\pi/4 D_{h\_gas}^2$ ) and its wetted perimeter ( $=\pi D_{h\_gas}$ ) determine the hydraulic gas diameter, which Tabatabai and Faghri (2001) estimated using the void fraction.

$$\alpha = \frac{A_{gas}}{A_{gas} + A_{liq}} = \frac{\frac{\pi}{4} D_{h\_gas}^2}{\frac{\pi}{4} D_h^2} \Rightarrow D_{h\_gas} = D_h \alpha^{0.5} \quad (3.4)$$

Using equations (3.3) and (3.4) the pressure drop due to the surface tension forces is approximated by:

$$-\left. \frac{dP}{dz} \right|_{surf} \approx -\frac{\Delta P_{surf}}{\Delta Z} \approx \frac{2\sigma/r_{eff}}{r_{eff}} = \frac{8\sigma}{D_h^2 \alpha}. \quad (3.5)$$

The ratio of both pressure drops,  $\Delta P_{ratio}$ , indicating the dominance of a term, Tabatabai and Faghri (2001) expressed as follows:

$$\Delta P_{ratio} = \frac{\left. \frac{dP}{dz} \right|_{surf}}{\left. \frac{dP}{dz} \right|_{gas} + \left. \frac{dP}{dz} \right|_{liq}} = \frac{4\sigma\rho_{gas}\rho_{liq}}{D_h\alpha(f_{gas}G_{gas}^2\rho_{liq} + f_{liq}G_{liq}^2\rho_{gas})} \quad (3.6)$$

The above equation shows that for liquids with a higher surface tension,  $\sigma$ , the capillary forces become more dominant. Reducing the channel diameter,  $D_h$ , the dominance shifts to the surface tension forces as well. At increased liquid mass fluxes,  $G_{liq}$ , or gas mass fluxes,  $G_{gas}$ , the shear forces become more important. Increasing the void fraction,  $\alpha$ , has a similar effect.

The models for transition lines (e.g. Taitel and Dukler 1974) have to be adapted in the regions where the surface tension forces are dominant over the shear forces. In these regions the surface tension forces need to be added to the shear and buoyancy force balance.

### 3.1.5 LITERATURE COMPARISON

The general conclusions may be summarised by stating that the two-phase flow pattern maps in the small diameter channels do not correspond to the pattern maps in large-diameter tubes. However, general agreement can be found between their data. A second remark on their findings could be made that the gravitational forces play a minor role, explaining the disappearance of the two groups: two-phase flow pattern map for horizontal channels and vertical channels. The stratified flow dominated by gravity is not reported in small-diameter channels. The present research extends the field of interest to lower superficial liquid velocities to investigate the occurrence of flow stratification in sub-millimetre channels.

## 3.2 Experimental

### 3.2.1 EXPERIMENTAL SETUP

The two-phase flow setup is designed to perform adiabatic flow experiments with air-water mixtures flowing through a square small-diameter PMMA channel, see Figure 3.7. Four channel cross-sections are investigated,  $800 \times 800 \mu\text{m}^2$ ,  $500 \times 500 \mu\text{m}^2$ ,  $200 \times 200 \mu\text{m}^2$  and  $100 \times 100 \mu\text{m}^2$ . The chosen channel diameter range (one tenth of a millimetre to about one millimetre) is the range which is commonly used in most industrial micro-fluidic systems (e.g. Shah 2005; Forschungszentrum Karlsruhe 2008).

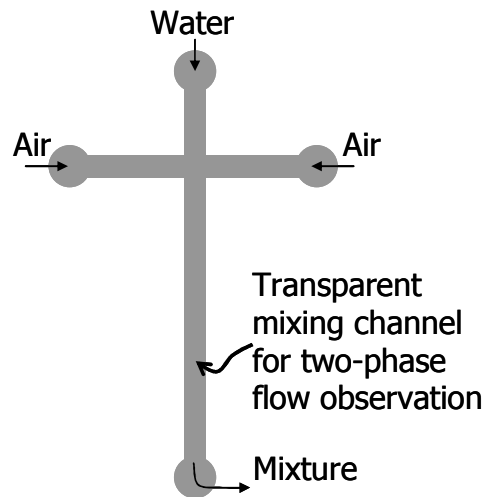


Figure 3.7 – Schematic overview of two-phase flow experiment. Four different channel geometries are investigated:  $800 \times 800 \mu\text{m}^2$ ,  $500 \times 500 \mu\text{m}^2$ ,  $200 \times 200 \mu\text{m}^2$  and  $100 \times 100 \mu\text{m}^2$ .

The length of the single phase air channels and water channel before joining in the mixing channel is 3 mm. This length ensures that the air and water flow are fully developed, thus minimising possible external supply influences, such as the shape of the supply tubing and the connection to it. The length of the transparent mixing channel is 12 mm.

The channels are constructed using precise micro-milling techniques in PMMA, resulting in micro precision and sub-micron roughness (optically determined). The milled structures are closed by a thin glass cover plate glued to the PMMA material. A UV hardening glue based on methacrylate (Photobond 4436, SIKO B.V.) is used, which allows a controlled manufacturing time. The liquid status of the glue and the resulting capillary effects force the glue in between the glass cover plate and the manufactured PMMA plate. By purging the non-hardened glued channel with air the possibly present redundant glue is blown away or evaporates in the purging air. The glue hardens only near its solid liquid interface. An extremely strong UV-lamp is used to instantly fixate the thin layer of glue. The thickness of the glue layer appears to be negligible to all researched channel diameters ensuring the desired channel diameter, see Figure 3.8.

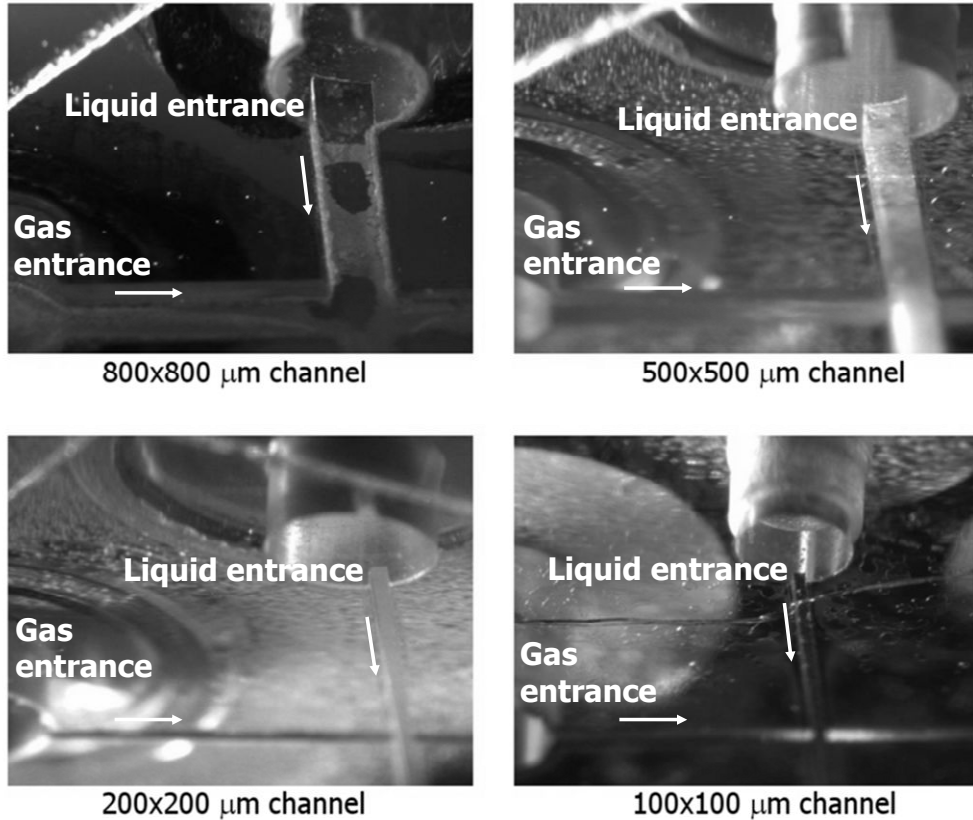


Figure 3.8 – Photos of the liquid entrance, mixing zone and a gas entrance of all four two-phase flow pattern mapping experiments.

After multiple experiments with the same channel, some irregularities (like colouring and sedimentation) could be detected on the channel walls. However, the possible flow disturbances induced by these irregularities did not change the observed two-phase flow pattern. This was investigated by checking the reproducibility of the first experiments in which no channel irregularities were present. The PMMA plate containing the mixing channel could be easily replaced, which allows us to use a different channel diameter of the mixing channel.

The gas supply is controlled by a thermal mass flow controller (Bronkhorst High Tech, EL-FLOW type). These controllers produce a stable and reproducible gas flow and have an accuracy of 0.5% (plus 0.1% of full scale). In order to cover the complete range of desired gas flows for all channels four controllers with different flow ranges were used: 0.02 to 1 ml<sub>n</sub>/min, 0.4 to 20 ml<sub>n</sub>/min, 6 to 300 ml<sub>n</sub>/min and 200 to 10 l<sub>n</sub>/min. Within the units “l<sub>n</sub>” stands for “normal litre”, which is one litre at standard conditions: p=1 bar and T=293 K. The overlap between the various flow controllers is chosen to have multiple data points measured with different flow controllers.

To minimise the gas compressibility effects on the flow, the tubing downstream from the gas controller towards the measurement channels is rigid and kept to a minimum volume. The temperature of the laboratory, and therefore also the temperature of the supplied air, is 293 K.

The liquid supply is by means of a syringe pump (KD-scientific, KDS101). In order to minimise the stepping behaviour of the pump (induced by the stepper motor), lower flow rates are supplied by thinner syringes; see Table 3.1.

Table 3.1 – Used syringes for the various liquid flow rates.

<b>Syringe volume [ml]</b>	<b>Inner diameter [mm]</b>	<b>Measured flow rates [ml/min]</b>
60	25.4	0.050 – 1.000
10	14.4	0.020 – 0.100
1	4.7	0.001 – 0.040

The used syringes ensure that for all applied flows the step frequency is higher than 10 Hz, with a micro-step advance of 0.088  $\mu\text{m}$ . Like the air the supply, the tubing for the water supply is kept short and rigid.

The outlet of the mixing channel is connected to a rather large tube for which the outlet is placed in a 'waste cup', which prevents the formation of water droplets at the outlet. This outlet configuration minimises the pressure fluctuations and maintains a near atmospheric pressure within the mixing channel. The pressure drop downstream from the air-water mixture zone towards the atmospheric outlet is estimated to be less than 0.05 bar (estimated by the total of the capillary pressure and the single phase shear stresses).

### 3.2.2 MEASUREMENT METHOD

By interchanging the various air and water supplies no clear mixing influence was found upon pattern detection at distances more than 10 channel diameters downstream of the mixing region. At distances larger than 5 channel diameters upstream from the end zone of the mixing channel no clear influence of the outlet could be detected. In most cases the length of the water slug or the air bubble exceeded the camera field of view. In the present experiments neither attention is given to the determination of the slug length, nor its frequency.

In order to measure at a reproducible depth in the mixing channel, a triangular slot with the same depth as the mixing channel was milled alongside the mixing channel. The position of the focus depth of the microscope lens is estimated easily by the in-focus part of the triangular bottom. In case of the present two-phase flow experiments the focal depth of the microscope was approximately at one third of the mixing channel depth. It was found that this depth provided the best image of the two-phase flow pattern. The applied magnification for the two widest channels (800  $\mu\text{m}$  and 500  $\mu\text{m}$ ) was 10 and the two smallest channels (200  $\mu\text{m}$  and 100  $\mu\text{m}$ ) were visualised using a 20 times magnification.

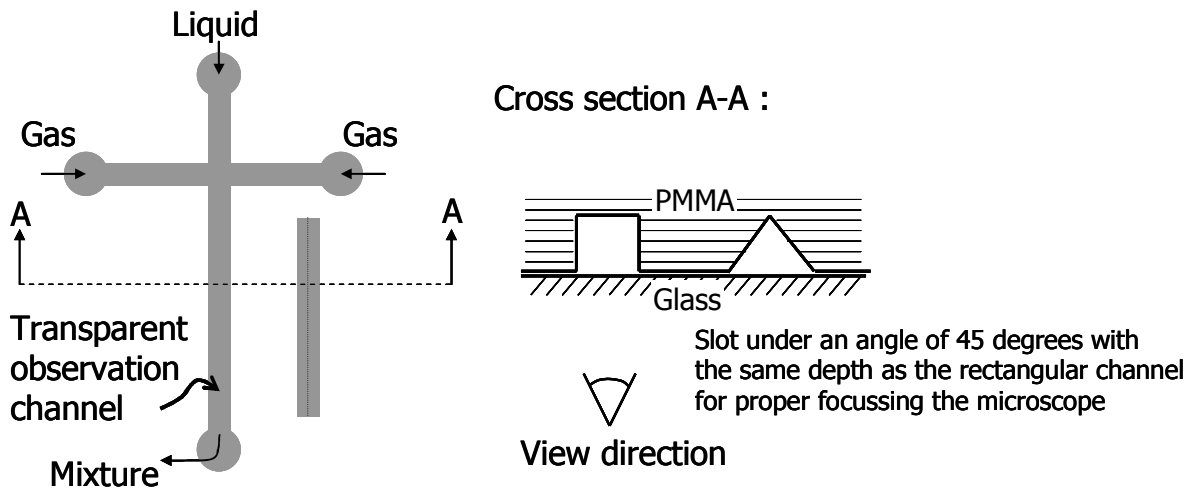


Figure 3.9 – Schematic overview of the experimental setup for the two-phase flow experiments including the triangular slot for improved reproducibility of focus depth.

Furthermore image enhancement was applied. The raw camera image of a slug bubble recorded with brightfield illumination is shown in Figure 3.10A.

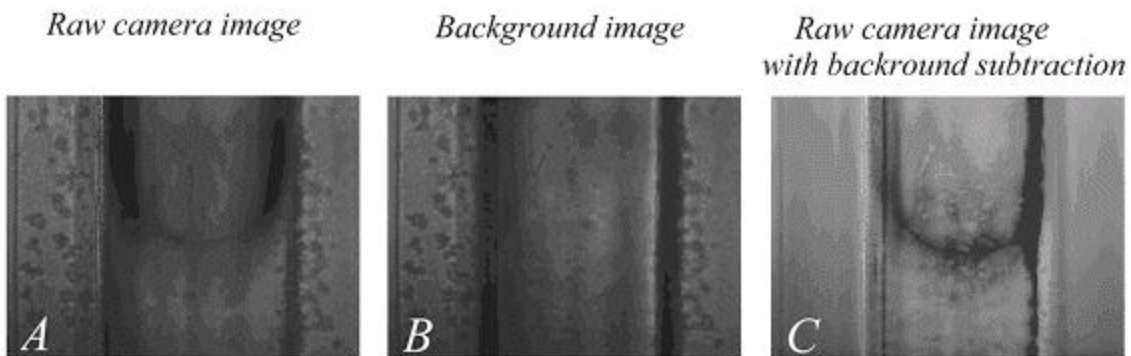


Figure 3.10 - *A*: Raw camera image of a passing slug bubble. *B*: 'background'-image (empty channel). *C*: 'Raw' camera image with the light of the 'background'-image subtracted. – Flow from top to bottom of the image –

The contours of a slug bubble are hardly visible. Only the interface between the air and the water is captured, which is also blurred due to the background light, the speed of the air bubble and the depth of field (ca. 30  $\mu\text{m}$ ). The quality of the recordings is improved significantly by taking an image of an empty (i.e. only filled with air) channel. This image contains only signal originating from the background and no signal from the air-water interface. This so-called background image (see Figure 3.10*B*) is then subtracted from the pictures of the air-water filled. After background subtraction the resulting image contains only information of the air-water interface and this improvement leads to a more robust better determination of the two-phase flow pattern (see Figure 3.10*C*).

Although in Figure 3.10*C* the gas-liquid interface is much more clear than in Figure 3.10*A*, only a priori knowledge on the bubble shape tells us what part is air and what part is water. The liquid film of the slug bubble is hard to detect and the image is still a somewhat blurred. Inherently the interface is smeared in brightfield illumination due to the depth of field and the curvature of the bubble. The blurring caused by the bubble motion can be minimised by shortening the exposure time,

however it will reduce the light intensity of the images. Therefore optimising the exposure time of the camera could result in a better image quality. Although, it should be mentioned that due to the large differences in speed of the gas-liquid interface during the complete pattern mapping, the optimum exposure time varies a lot. It would be a substantial effort to adjust the exposure time for each measurement.

The above considerations led to an alternative measurement technique visualising the water only. This method is based on adding a fluorescent dye, rhodamine B, to the water. This dye absorbs green light (absorption peak at 550 nm) and emits orange/red light at a longer wavelength (emission peak at 590 nm), Aoshima *et al.* (1984). Rhodamine B has no significant impact on the contact angle between water and PMMA, see 3.2.4. We use the light of the frequency-doubled Nd:YAG laser with a wavelength of 532 nm for illumination. A low pass optical filter, placed in front of the camera accomplishes that only the red light emitted by the water reaches the CCD chip of the camera, while all other scattered green light is blocked (see Figure 3.11A).

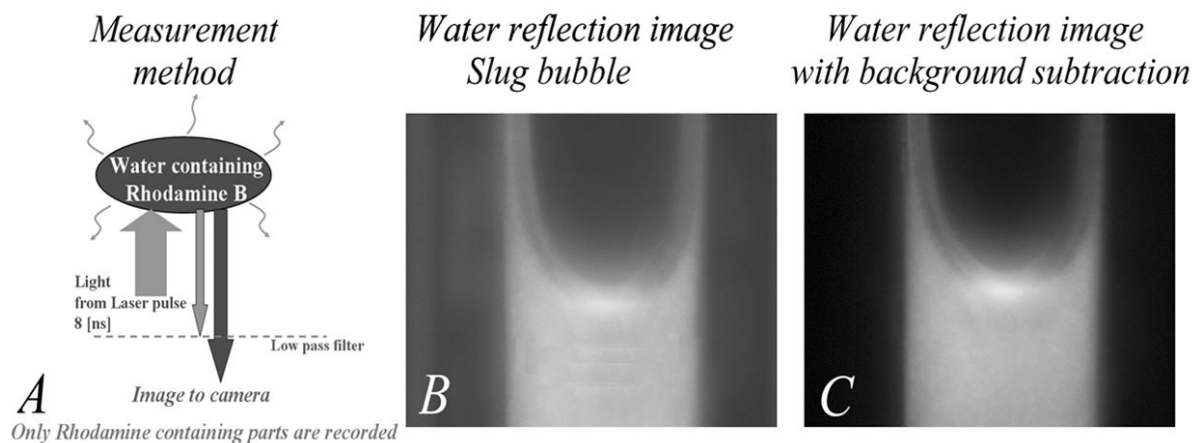


Figure 3.11 - *A*: Schematic overview of fluorescence measurement technique detecting only the aqueous parts. *B*: Slug bubble image using fluorescence technique. *C*: Slug bubble image using fluorescence technique combined with background subtraction. – Direction of the flow is from top to bottom of the image –

Due to the short pulse with a duration of 5 – 10 nanoseconds of the laser and its high intensity the bubble images are not subject to motion blur. Therefore no special attention is needed for the exposure time of the camera, see Figure 3.11*B*. Using this measurement method fast moving thin water layers like liquid bridges can be properly detected. Applying the background subtraction method (which is only an initial effort) as explained above further enhances the image with relatively little extra effort. Figure 3.11*C* is a typical measurement picture showing only the aqueous regions. For a discussion on the distortion effect (e.g. 'double' bubble edges) of the bubble images see e.g. Dias and Riethmuller (1998).

### 3.2.3 PATTERN DEFINITION

Most often the determination of two-phase flow patterns is based on visual observations. This subjective method leads to considerable differences in flow maps between different researchers. However, in most cases all the various two-phase

flow patterns may be related to one of the six most common two-phase flow patterns. These basic two-phase flow patterns are adapted from those given by Taitel and Dukler (1976), who described the two-phase flow patterns in macro channels, namely: *Stratified, Wave, Bubble, Slug, Churn and Annular (mist)* flow (see chapter 2.1.6). In accordance with previous investigations on two-phase flow pattern mapping in micro channels (Chung and Kawaji 2004; Wambsganss *et al.* 1991; Sobierska *et al.* 2004; Tabatabai and Faghri 2001; and Zhao and Bi 2001), no gravity-dominated patterns are found in this investigation. This leaves only the surface tension dominated regimes (slug, churn and bubble flow) and the shear dominated flow regime (annular flow).

To illustrate the identification of the various two-phase flow patterns, photographs that are representative of the two-phase flow patterns observed in the present research are shown in Figure 3.12.

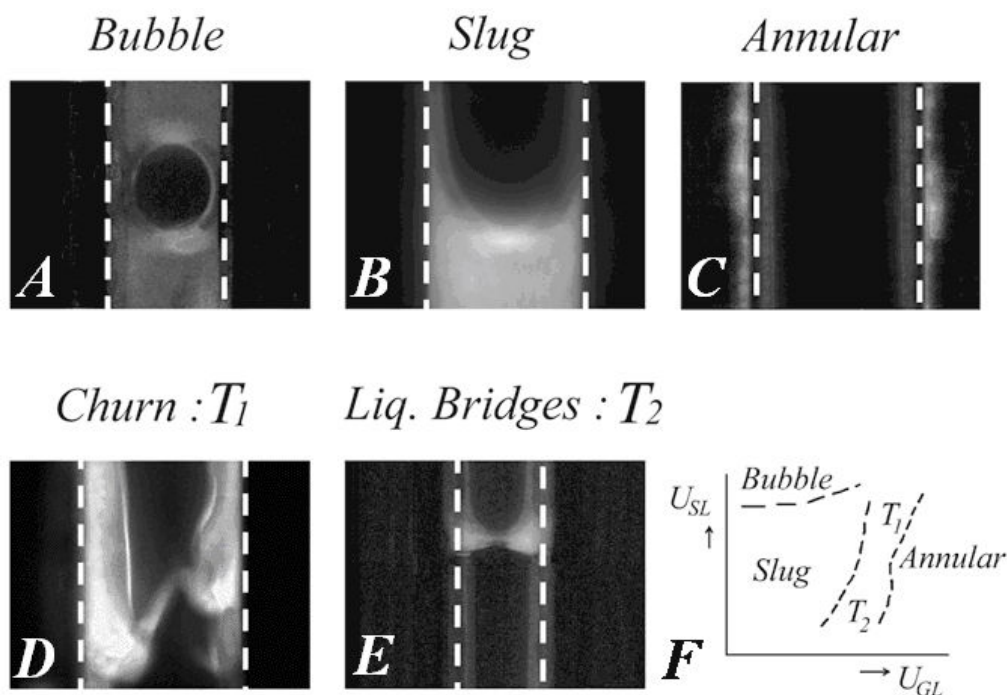


Figure 3.12 - Images using fluorescence technique detecting only the aqueous parts. *A, B, C*: The three “anchor”-patterns: Bubble flow, Slug flow and Annular flow. *D, E*: The two general transitions patterns. *F*: General indication of the pattern position in a two-phase flow pattern map.

For reasons of simplicity only three major patterns are chosen as “anchor-patterns”, namely: bubble (No straight thin film part, Figure 3.12*A*), slug (Elongated bubble separated by a liquid slug, Figure 3.12*B*) and annular-flow (No liquid bridging the channel, Figure 3.12*C*), while the remaining flow patterns: churn (Figure 3.12*D*) and liquid bridges (Figure 3.12*E*) are classified as slug-annular transition patterns. An indication of the general pattern positioning in a two-phase flow pattern map is given in Figure 3.12*F*.

Before starting the determination of the two-phase flow pattern, the flow is stabilised for each specific data point. After this stabilising period, between 200 and 500 pictures are recorded at a frame rate of 10 frames per second. Due to the (possible) high velocities in the mixing channel the camera recording should be

interpreted as individual snapshots of the flow. Long vapour bubbles could be identified as annular flow judging from one single snapshot. However, only if all 200 snapshots did not show any liquid slugs, air bubble tips or liquid bridges, the flow is classified as annular.

### 3.2.4 CONTACT ANGLE RHODAMINE B/WATER - PMMA

Rhodamine B is not known to act as a surfactant. We verified this by estimating the contact angle of droplets deposited on PMMA containing various Rhodamine B solutions. The investigated solutions are 50 mg/l, 20 mg/l, 10 mg/l and 0 mg/l (i.e. distilled water). The experiments are performed at room temperature (293K).

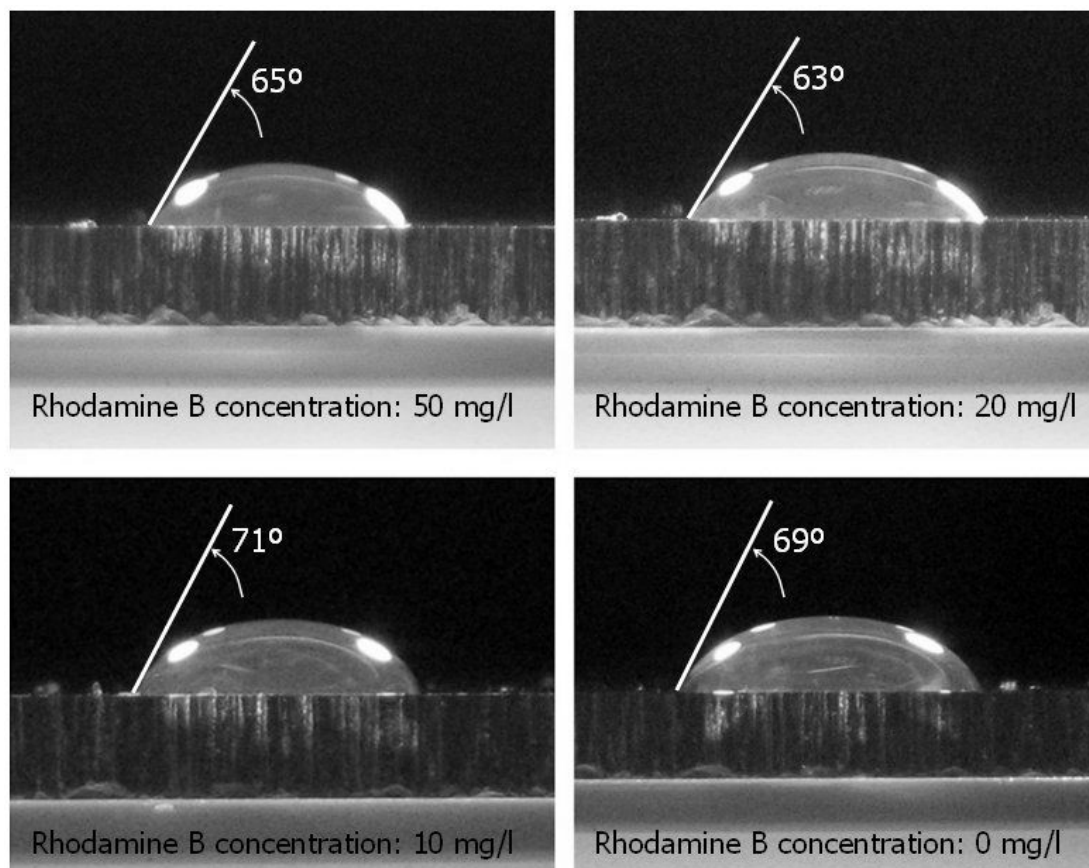


Figure 3.13 – Visual contact angle estimation water-Rhodamine B solution on PMMA.

We find a contact angle for (distilled) water on PMMA of about  $70^\circ$ , which is similar to the commonly accepted contact angle of  $73^\circ$  in literature, e.g. Kwok *et al.* (1998). On adding Rhodamine B to the water the contact angle is generally slightly decreased,  $66^\circ \pm 5^\circ$ . Although we have put our best effort in obtaining as accurate as possible the proper contact angle, our applied method remains subjective by visually estimating the slope near the contact surface. A more objective method, such as the “Axisymmetric Drop Shape Analysis” as applied by Kwok *et al.* (1998) should be used to determine the exact status of Rhodamine B of acting as a surfactant. However, to estimate this exact status is beyond the scope of this work, and for the remainder of this work it is assumed to be negligible.

In our investigation to map the two-phase flow regimes we have used the same Rhodamine B concentration (20 mg/l) for all experiments and named it an air-

“water” two-phase flow. One should therefore bear in mind that our “water” might have a slightly different (however most likely constant for all experiments) contact angle, or surface tension, as “pure” water.

### 3.3 Results and discussion

For the experiments the liquid flow range is limited from 0.001 ml/min to 1 ml/min, using three types of syringes. The gas flow range could be varied from 0.03 ml<sub>n</sub>/min to 10 l<sub>n</sub>/min using four different gas flow controllers. The liquid flow limitation to a maximum of 1 ml/min restrains the measurable superficial liquid velocities for the larger channels. The available gas flow range made it possible to measure at all desired superficial gas velocities.

#### 3.3.1 800 MICRON SQUARE CHANNEL

Figure 3.14 shows the two-phase flow pattern map for an air-water mixture flowing concurrently through a PMMA channel.

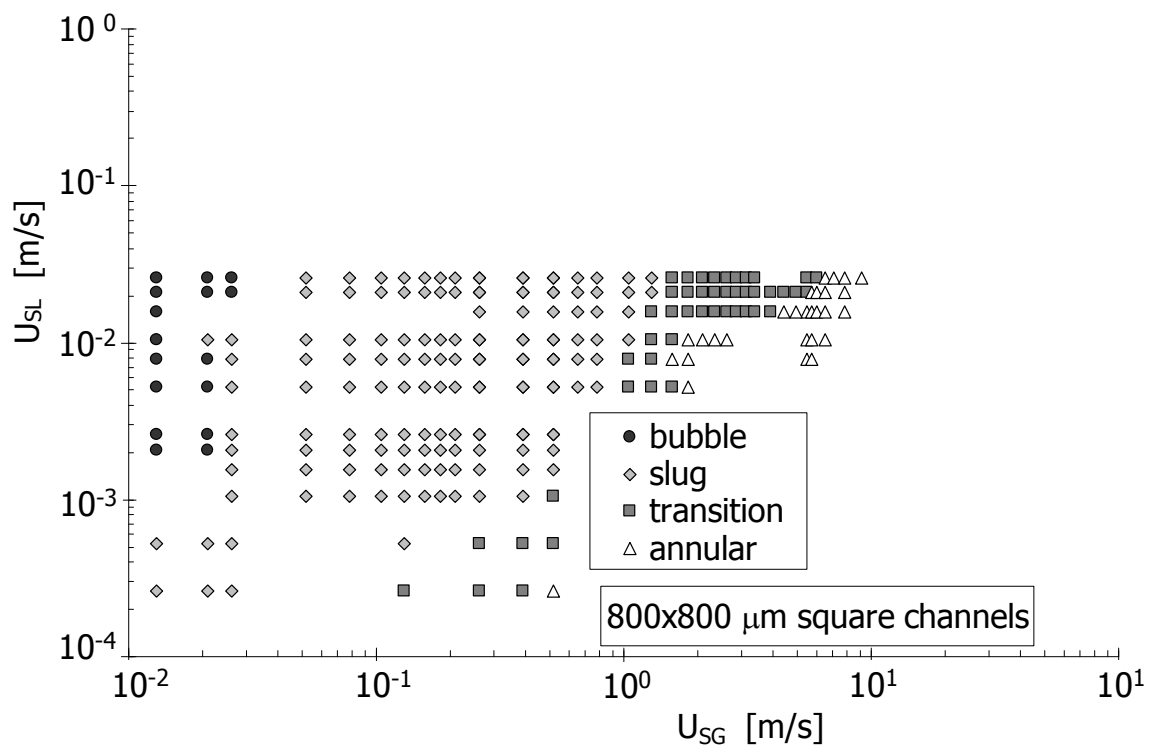


Figure 3.14 – Two-phase flow pattern map, 800x800 μm<sup>2</sup> PMMA channel with air-water concurrent flow. The vertical axis displays the superficial water velocity and the superficial air velocity is placed on the horizontal axis.

At certain positions in the map no smooth transition line can be drawn through the transitions from one two-phase flow pattern to another. This may be due to the manner of determining the two-phase flow pattern, which is based on visual observations, which can be rather subjective. Although, on random duplication measurements the position of the transitions did not vary more than one measurement position.

At higher water velocities ( $U_{SL} > 1 \cdot 10^{-2}$  m/s) the transition from slug flow to transitional flow (churn flow) happens at roughly 1-2 m/s superficial air velocity. At lower water superficial velocities this transition to transitional flow (liquid bridges) shifts to lower superficial air velocities. The transition towards annular flow occurs at  $U_{SG} \approx 0.5$  m/s for the lowest superficial water velocity and at  $U_{SG} \approx 7$  m/s for the highest water flow rate. For very low superficial gas velocities the existence of the bubble flow regime is observed. A stratified flow regime, however, is not observed in the entire range of investigated gas and liquid flows.

### 3.3.2 500 MICRON SQUARE CHANNEL

The two-phase flow pattern map obtained from the air-water experiments in a  $500 \times 500 \mu\text{m}^2$  channel is shown Figure 3.15. The vertical axis holds the superficial liquid velocity and the horizontal axis displays the superficial air velocity.

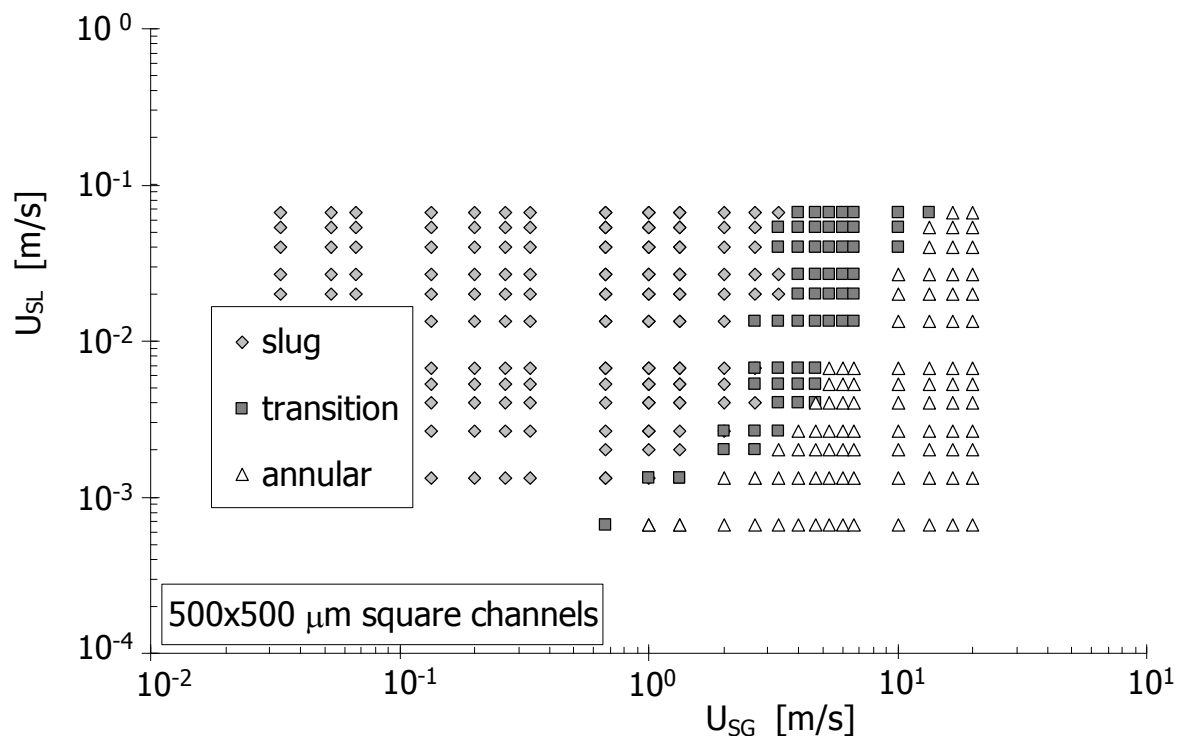


Figure 3.15 – Two-phase flow pattern map,  $500 \times 500 \mu\text{m}^2$  PMMA channel with air-water concurrent flow

At higher superficial water velocities ( $U_{SL} > 2 \cdot 10^{-2}$  m/s) the transition from slug flow to transitional flow (churn flow) happens at a superficial air velocity of roughly 3-4 m/s. At lower water velocities the transition to transitional flow (liquid bridges) shifts to lower superficial air velocities. The transition towards annular flow occurs at  $U_{SG} \approx 0.8$  m/s at the lowest superficial water velocity and at  $U_{SG} \approx 15$  m/s for the highest water flow rate. In the researched range of superficial water and air velocities no bubble flow is observed. Also, a stratified flow regime is not observed in the entire range of researched gas and liquid flows.

### 3.3.3 200 MICRON SQUARE CHANNEL

The two-phase flow pattern map obtained from the air-water experiments in a 200x200  $\mu\text{m}$  channel is shown Figure 3.16. The vertical axis holds the superficial liquid velocity and the horizontal axis displays the superficial air velocity.

The transition from slug flow to transitional flow (churn flow) happens at a superficial air velocity of roughly 3-5 m/s in the upper part of the pattern map ( $U_{SL} > 2 \cdot 10^{-2}$  m/s). The transition moves to lower superficial gas velocities at lower superficial water velocities. The annular flow transition occurs at 0.4 m/s superficial air velocity for the lowest water flow. For a superficial water velocity of 4 m/s the annular flow transition occurs at approximately 25 m/s superficial air velocity. It should be noted that the distinction between churn flow and annular flow at the high flow rates is rather difficult. No bubble flow is observed in the pattern mapping experiments in a 200x200  $\mu\text{m}$  channel. Again, a stratified flow regime is not observed in the entire range of researched gas and liquid flows.

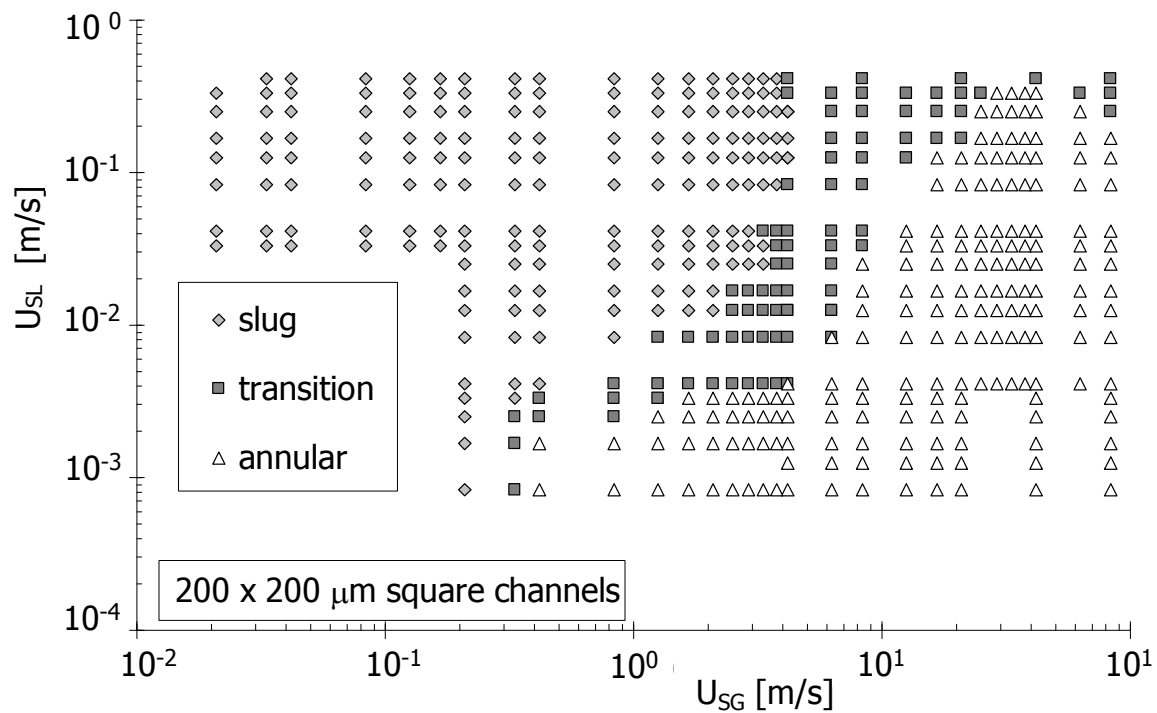


Figure 3.16 – Two-phase flow pattern map, 200x200  $\mu\text{m}^2$  PMMA channel with air-water concurrent flow

### 3.3.4 100 MICRON SQUARE CHANNEL

Figure 3.17 shows the 100x100  $\mu\text{m}^2$  two-phase flow pattern mapping results.

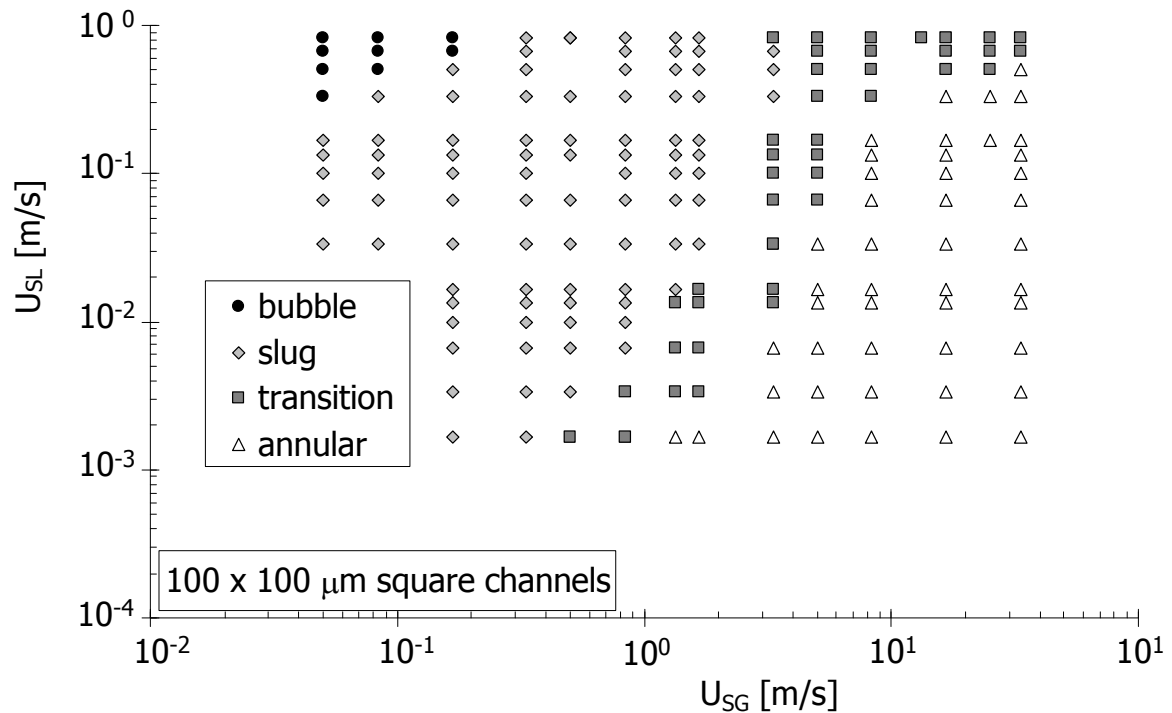


Figure 3.17 – Two-phase flow pattern map, 100x100  $\mu\text{m}^2$  PMMA channel with air-water concurrent flow

In Figure 3.17 the superficial air velocity is placed on the horizontal axis and the vertical axis holds the superficial water velocity.

The transition from slug to transitional flow occurs at about a superficial air velocity of 3-4 m/s for superficial liquid velocities higher than  $2 \cdot 10^{-2}$  m/s. At lower superficial liquid velocities the location of transition shifts to lower superficial gas velocities. The annular flow transition starts at 0.4 m/s superficial gas velocity and increases moving to higher superficial liquid velocities. For the highest water flow rates ( $U_{SL} > 0.6$  m/s) no clear transition towards annular flow could be observed. Bubble flow is observed at low superficial gas velocities in the upper part of the graph.

### 3.3.5 OVERVIEW

The two-phase flow pattern maps developed for all four channel diameters are compared in Figure 3.18.

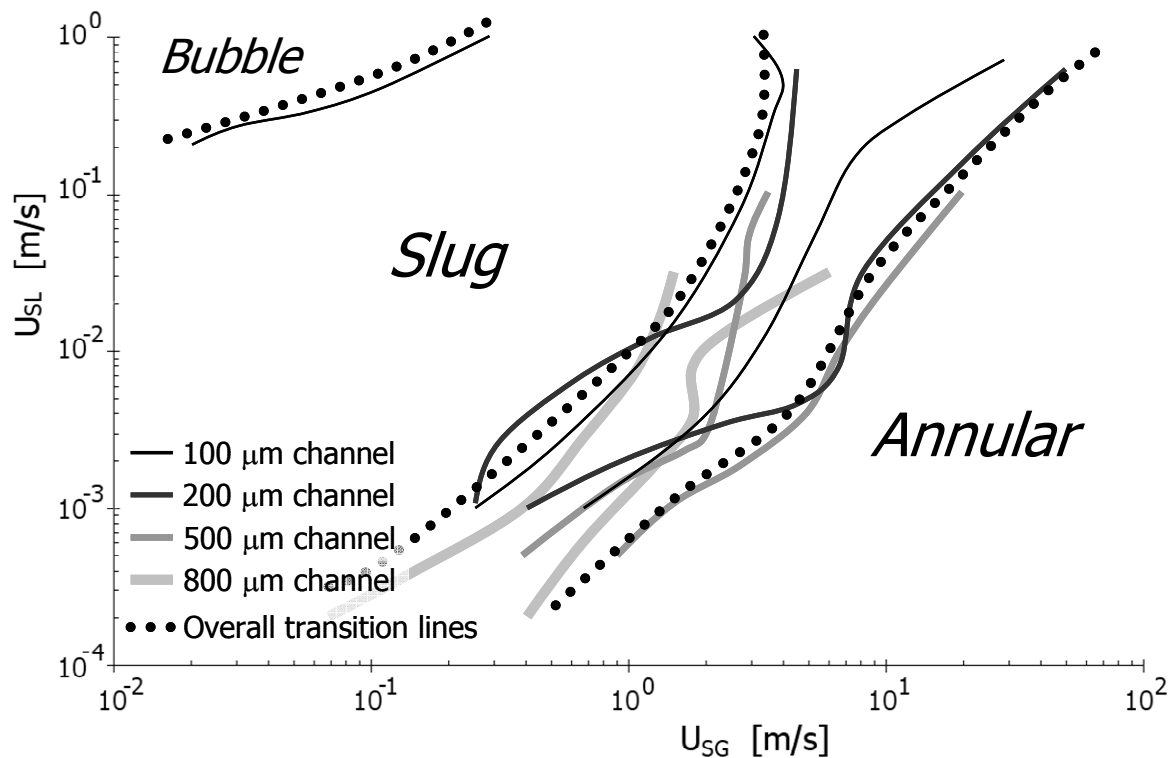


Figure 3.18 – Superposition of all four channel diameters ( $D_h=800, 500, 200$  and  $100 \mu\text{m}$ ) and the suggested overall transition lines for air-water mixtures flowing through small diameter channels.

Figure 3.18 shows no consistent movement of the slug-annular transitional flow pattern boundaries as the channel size decreases. The variance in transition lines may indicate some uncontrolled influence or hysteresis or chaotic behaviour. Further investigations are suggested, emphasising the less subjective determination methods like pressure drop measurements or (void) frequency measurements.

The overlap in the transitional flow pattern regions of the four channels suggests that channels ranging from  $100 \mu\text{m}$  to  $800 \mu\text{m}$  will contain similar two-phase flow behaviour. Overall transition lines for small diameter can be drawn as in Figure 3.18. The slug-annular transitional flow region of the overall pattern map is chosen a bit wider than the transitional flow regions for a single channel. However, it should always be borne in mind that the transition lines do not indicate sharp boundaries but rather smooth ones. The overall transitional flow area for small diameter channels should be interpreted as a region in which transitional flow patterns may occur.

The transition from slug to bubble flow is observed at very low gas velocities. Only at high superficial liquid velocities the bubble pattern region expands more. Since there is no dispersed bubbly flow, the bubble flow in small diameter channels is regarded not to be induced by shear forces during the two-phase mixing. The bubble flow is rather seen as the result of small air packages torn off from the air supply channel by the liquid flow before they could form a 'proper' slug bubble.

### 3.3.6 CONCLUSIVE REMARKS

The two-phase flow pattern maps developed for the tested small diameter channels are compared with small diameter maps found in literature. The channels tested by Wambsganss *et al.* (1991) mark the upper limit of the small diameter channels ( $Co=0.5$ ), while the channels tested by Zhao and Bi (2001) and Chung and Kawaji (2004) are typical small diameter channels. Direct comparison between the various maps is shown in Figure 3.19.

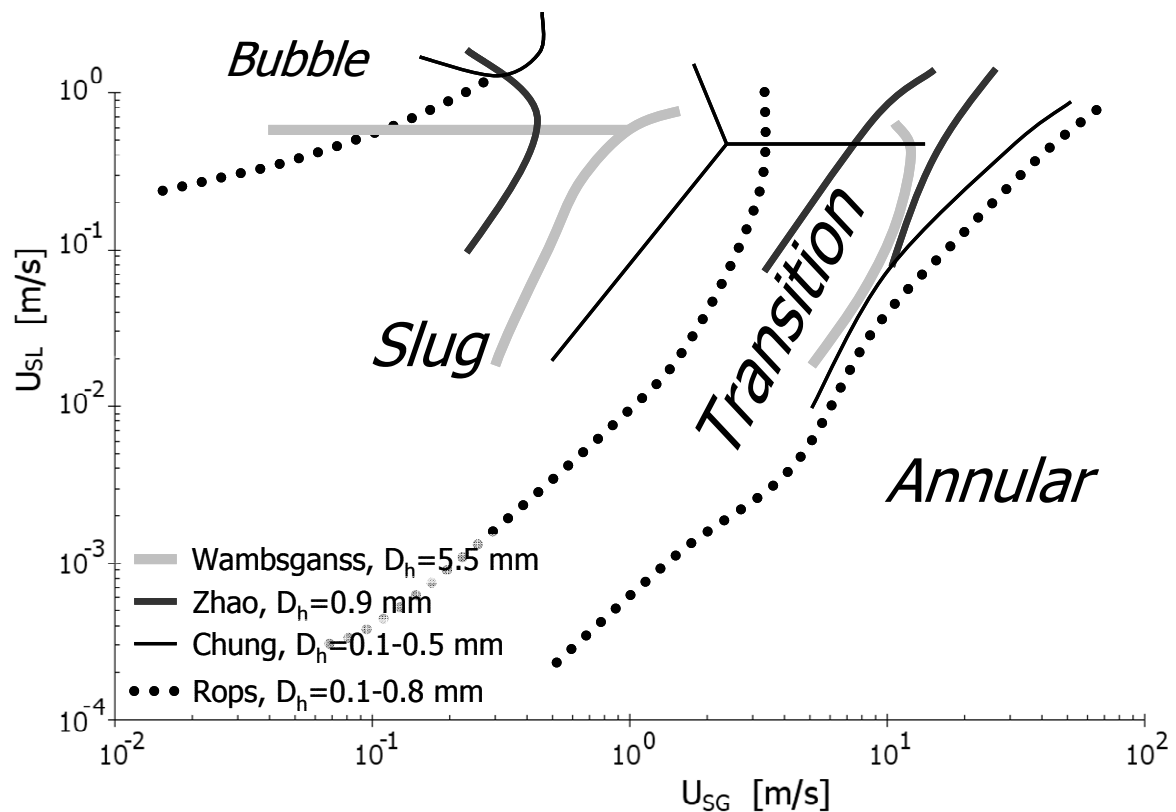


Figure 3.19 - Comparison of the present data (Rops;  $D_h=0.1-0.8$  mm, PMMA, square) with the maps of Wambsganss *et al.* (1991) ( $D_h=5.5$  mm, PMMA, rectangular), Zhao and Bi (2001) ( $D_h=0.9$  mm, PMMA, triangular) and Chung and Kawaji (2004) ( $D_h=0.1-0.5$  mm, fused silica, circular)

The annular flow transition roughly coincides for all tested channels. The transition from slug flow towards transitional-flow pattern is not so well-defined. The larger channel measured by Wambsganss *et al.* (1991) shows a transition at lower superficial gas velocities than the sub-millimetre channels. The slug transition line found in the present research lies in between the results of Zhao and Bi (2001) and Chung and Kawaji (2004) sub-millimetre channels. Poor agreement is seen in the bubble transition for the different channels tested. The results by Chung show bubble flow only for superficial liquid velocities higher than 1 m/s, while Zhao indicates that if the gas velocity is low enough ( $U_{SG} < 0.2$  m/s) bubble flow will occur. The present work corresponds best to the results found by Wambsganss *et al.* (1991) positioning the bubble transition line roughly at a superficial liquid velocity of 0.7 m/s. Only at much lower superficial gas velocities ( $U_{SG} < 2 \cdot 10^{-2}$  m/s) bubble flow is observed.

Despite the differences in the pattern maps measured by the various researchers, a general overall agreement can be seen. This rough correspondence indicates that despite the different channel geometries (square, round, triangular, rectangular) the two-phase flow behaviour is not largely affected. Varying the material (PMMA: contact angle  $\sim 70^\circ$ , coated fused silica: contact angle  $\sim 95^\circ$ ) does not result in a large variance of the two-phase flow pattern map as well.

The present work is in correspondence with the observations available in literature and extends the researched region to lower superficial liquid velocities. This allows to investigate the occurrence of stratified flow in the expected regions of the two-phase flow pattern map. The present experiments show no stratified flow or wavy flow pattern region, see Figure 3.19. Therefore, in order to predict the transition lines the stratified flow is most likely not the most adequate initial two-phase flow pattern.



## 4 Boiling miniaturisation

Within the following chapter the confined pool boiling mechanism will be presented. Decreasing the boiling surface together with the boiling pool leads to a surprising heat transfer enhancement. Before showing our results and explanation the present status is given of the knowledge on three interacting phenomena during pool boiling.

### 4.1 Present status

The nucleate boiling enhancement on pool boiling miniaturisation is a result of various interacting phenomena. To obtain a better understanding three important parameters will be discussed in detail: nucleation site density, bubble detachment frequency and heater miniaturisation.

#### 4.1.1 NUCLEATION SITE DENSITY

The nucleate boiling heat flux is related to the nucleation site density on which many published correlations exist. Sakashita (2001) compared several correlations to experimental data. Most correlations can be written in the following form:

$$q'' = c \Delta T^{m_1} N_a^{m_2} \quad (4.1)$$

in which  $c$  is a function of varying physical properties and boiling geometry. Best agreement with the measurements is found if the powers  $m_1$  and  $m_2$  for the wall superheat,  $\Delta T$ , and nucleation site density,  $N_a$ , are set to  $3/2$  and  $3/8$  respectively. Sakashita (2001), however, proposes the following relation for the nucleate boiling heat flux:

$$q'' = c \Delta T^{4/3} N_a^{3/8} \quad (4.2)$$

$$C_{Sakashita} = 0.5 \lambda_{liq} \left( \frac{\sigma_{liq}}{\mu_{liq} \frac{\lambda_{liq}}{\rho_{liq} c_{p,liq}}} \right)^{1/4} \left( \frac{\mu_{liq} c_{p,liq}}{\lambda_{liq}} \right)^{-1/12} \left( \frac{\rho_{liq} c_{p,liq}}{\rho_{vap} h_{ev}} \right)^{1/3}$$

The three groups in the factor  $C_{Sakashita}$  have the following physical meaning: the first group is the ratio of surface tension forces and viscous forces which are related to the average thickness of the conduction layers formed under the primary bubbles. The second group is the liquid Prandtl number, and the third group is related to the Jakob number.

The prediction of the nucleation site density is fundamental for the development of mechanistically based nucleate boiling heat transfer models. Using various physical assumptions, a number of models for the nucleation site density exist. Most models, however, use a cavity from which a (spherical) vapour bubble initiates and grows, see for example Hsu (1962). The wall superheat has to compensate for the additional pressure invoked by the surface tension of the vapour bubble. Qi and Klausner (2006) experimentally investigated the nucleation site density occurring during pool boiling and (adiabatic) gas nucleation.

In case of water on a brass surface Qi and Klausner (2006) report results as shown in Figure 4.1.

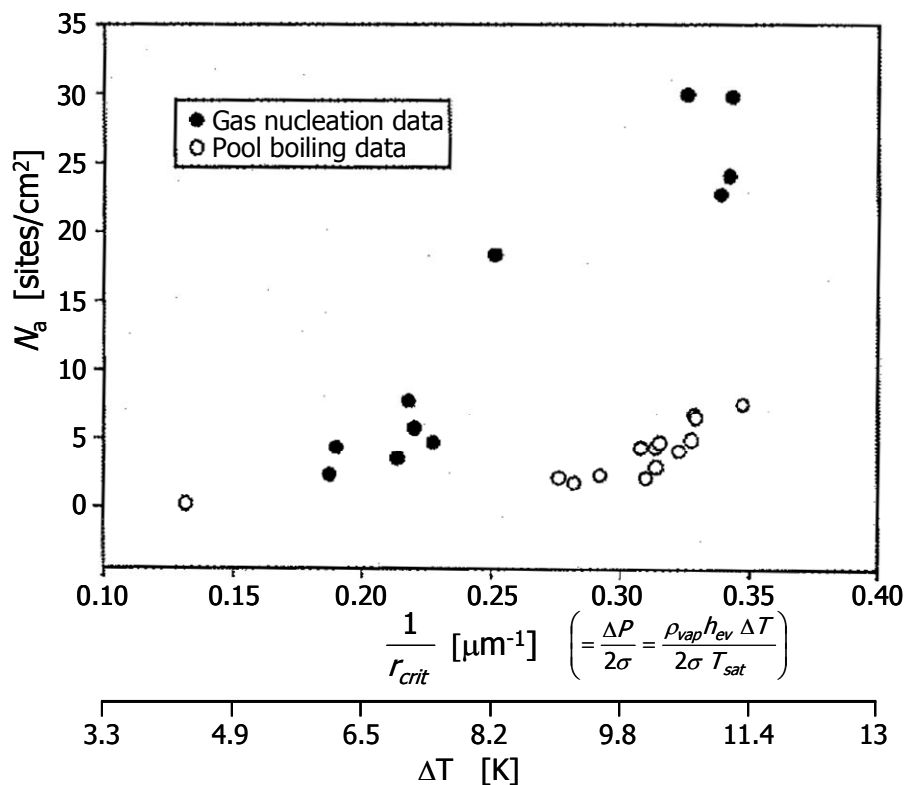


Figure 4.1 – The nucleation site density as function of the critical cavity radius required for incipience using gas nucleation and pool boiling (water on brass). The secondary horizontal axis represents the wall superheat in case of the boiling experiments. – data taken from Qi and Klausner (2006) –

Figure 4.1 shows that the nucleation site density follows a similar trend for both the gas nucleation experiments and the pool boiling experiments. However, for the same cavity radius more nucleation sites are active in case of the gas nucleation experiments. They observe a similar behaviour in case of water on a stainless steel surface. Two possible explanations for the higher nucleation site density in case of the gas nucleation experiments are mentioned by Qi and Klausner (2006):

1. a (very) thin thermal boundary layer results in an upper limitation of the size of appropriate nucleation sites. No such limitation exists for gas nucleation,
2. in the vicinity of a nucleation site energy is removed from the heater that suppresses the formation of active nucleation sites in the vicinity.

The availability of a nucleation cavity with an appropriate size is related to the surface roughness. Benjamin and Balakrishnan (1997) determined the nucleation site density with a variety of surface finishes on different materials in combination with various liquids. It is claimed that as the average micro roughness,  $R_a$ , of the surface increases, the nucleation site density first decreases and then increases for a given heat flux. The left graph of Figure 4.2 shows some indications of this observation, however similar graphs for other liquids do not clarify this statement entirely. The pool boiling curves show a lesser dependency on the roughness than on the material, see right graph of Figure 4.2.

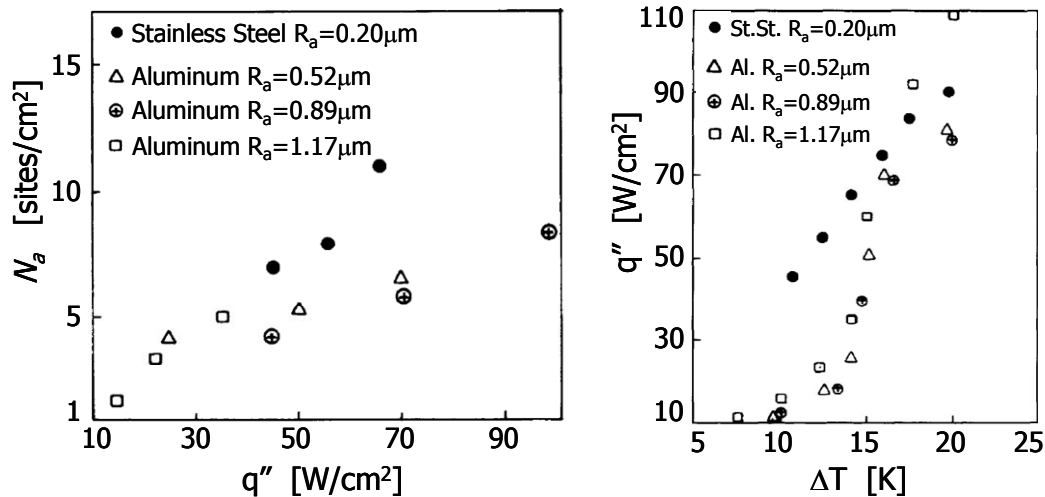


Figure 4.2 – Influence of surface roughness on nucleate boiling (water as boiling liquid). Left: nucleation site density as a function of the heat flux on different boiling surfaces. Right: the heat flux plotted against the wall superheat for various materials and surface roughness. – data taken from Benjamin and Balakrishnan (1997) –

The overlap of the different boiling curves indicates that all desired nucleation sites for the pool boiling process can be activated, despite the variance in roughness. The onset of nucleate boiling (ONB) point depends on the surface roughness as shown by Qi and Klausner (2006), Figure 4.3. Again, for different surface roughness the nucleation site densities overlap in the developed nucleate boiling regime.

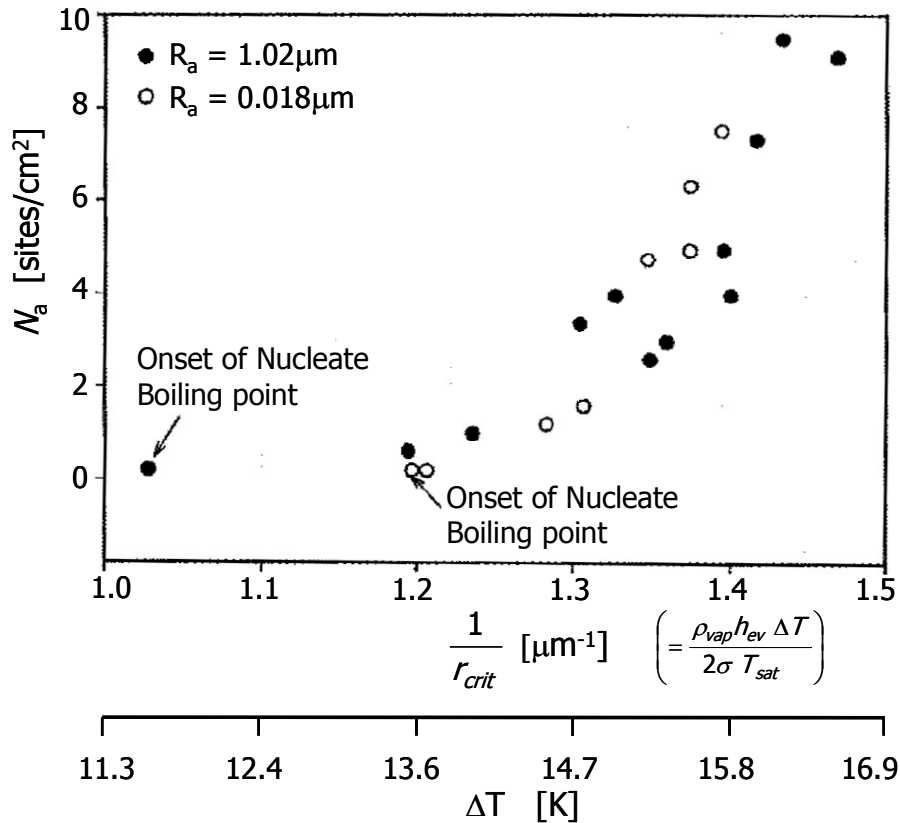


Figure 4.3 – Nucleation site density as function of the critical cavity radius required for incipience in pool boiling (ethanol on brass). The secondary horizontal axis represents the wall superheat. – data taken from Qi and Klausner (2006) –

Benjamin and Balakrishnan (1997) obtained a correlation for the nucleation site density as a function of the liquid properties (Prandtl number), the solid-liquid interaction (ratio of thermodynamic properties), the surface roughness and the wall superheat:

$$N_a = 218.8 \frac{\text{Pr}^{1.63} \cdot \Delta T^3}{\tilde{T}^{0.5} \cdot \tilde{R}^{0.4}} \quad (4.3)$$

$$\text{with: } \tilde{T} = \frac{\lambda_{wall} \rho_{wall} C_{p\_wall}}{\lambda_{liq} \rho_{liq} C_{p\_liq}}$$

$$\tilde{R} = 14.5 - 4.5 \left( \frac{R_a P}{\sigma} \right) + 0.4 \left( \frac{R_a P}{\sigma} \right)^2$$

Equation (4.3) shows the strong influence, on nucleation site density, of the wall superheat,  $\Delta T$ , and the Prandtl number, Pr. The influence of the roughness parameter,  $\tilde{R}$ , and thermodynamic solid-liquid interaction,  $\tilde{T}$ , are accounted for using an exponent smaller than 1. In case of water boiling on a copper surface the proposed formula results in approximately 1 active site per cm<sup>2</sup> at a wall superheat

of 5 K (Onset of Nucleate Boiling) and about 100 active sites per  $\text{cm}^2$  near the CHF-temperature ( $\Delta T \sim 24$  K). These values correspond to the values that were measured by Basu et. al. (2002).

#### 4.1.2 BUBBLE DETACHMENT FREQUENCY

Interactions between nucleation sites influence the bubble detachment frequency. Zhang and Shoji (2003) identify three significant interactions.

First, the hydrodynamic interaction between growing vapour bubbles is identified. This interaction through the surrounding liquid increases the bubble detachment frequency and is most noticeable at a cavity spacing of two bubble diameters.

Secondly, thermal interaction through the solid causes a diminishing effect on the bubble detachment frequency. The span of influence of the cooled down region around an active nucleation site depends on the thermodynamic properties of the solid.

Finally, horizontal and declining bubble coalescence (see Figure 4.4) results in a strong increase of the bubble frequency.

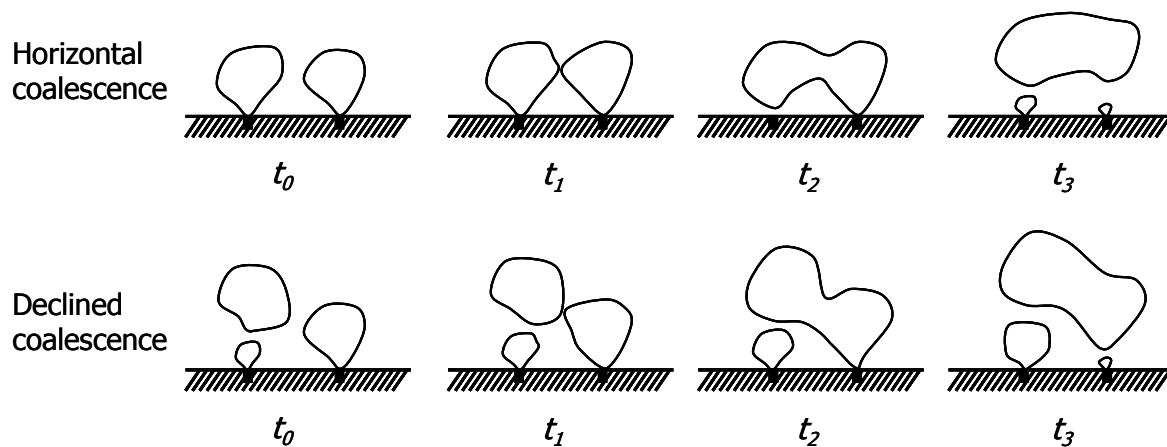


Figure 4.4 – Schematic visualisation of two types of bubble coalescence near the surface. Top: horizontal coalescence of two primary bubbles; Bottom: inclined coalescence of a primary and secondary bubble. – drawing after Zhang and Shoji (2003) –

The coalescence span of influence on the bubble detachment frequency exceeds just one bubble diameter at the moment of detachment. Zhang and Shoji (2003) summarised the effect of the three interactions between nucleation sites in a graph on the average bubble detachment frequency, shown in Figure 4.5. Negligible influence of all three interactions is found if the cavities are more than three bubble diameters apart from each other, indicated as the independent region. In case the cavities are less than 3 bubble diameters apart, the hydrodynamic interactions come into play increasing the bubble detachment frequency. In their case (water-silicon) the thermal interactions come to play a role of importance within cavity spacing of 2 bubble diameters. Finally, the coalescence interactions take over if the cavities are separated by less than 1.5 bubble diameters.

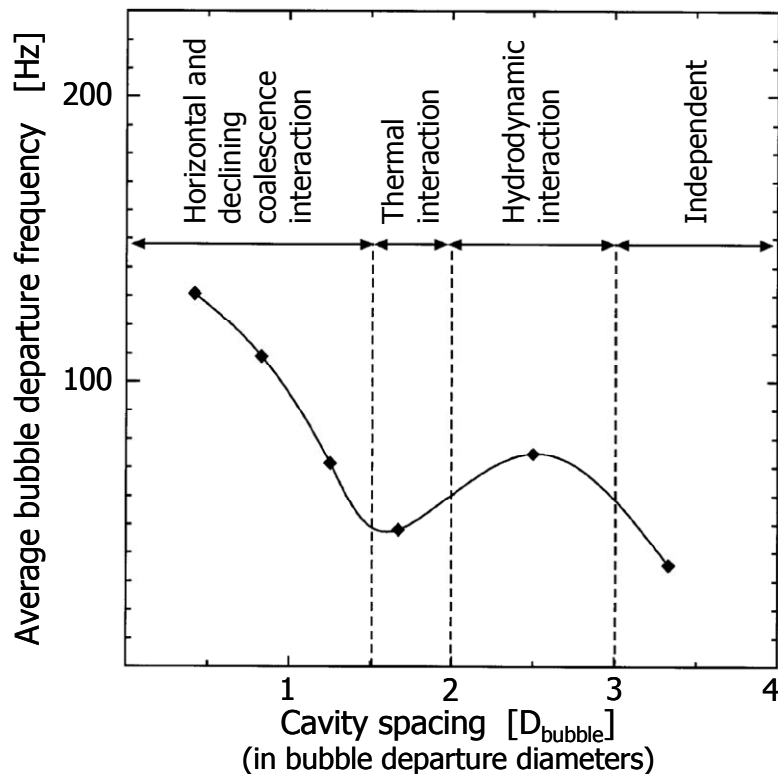


Figure 4.5 – Bubble detachment frequency as a function of the spacing between two cavities on a silicon boiling plate (water as boiling liquid). Four cavity interaction regions are indicated. – data taken from Zhang and Shoji (2003) –

During nucleate boiling the bubble detachment frequency may be increased applying various means.

Wu *et al.* (1998) investigated the effect as a result of the addition of low concentrations of surfactant. At the applied concentrations the physical properties of the water causes no change in physical properties except for the surface tension, which is greatly reduced. Although some shortening of the bubble ebullition cycle is observed, the mechanism responsible for the heat transfer increase is not explained. Especially, considering that the surfactants need to migrate to the interface and the surface tension effects only come into play after several seconds. Therefore the time scale for the surfactants is at least an order of magnitude larger than the time scales involving vapour bubble formation and growth.

Zhao *et al.* (2003) enhanced the bubble detachment frequency by forcing vertical vapour bubble coalescence. In order to promote vertical coalescence a wire mesh is placed above the boiling surface. This mesh forces the secondary bubbles to stay closer to the boiling surface. The growing primary vapour bubbles on the surface make early contact with the (large) secondary vapour bubble yielding in vertical coalescence, see Figure 4.6.

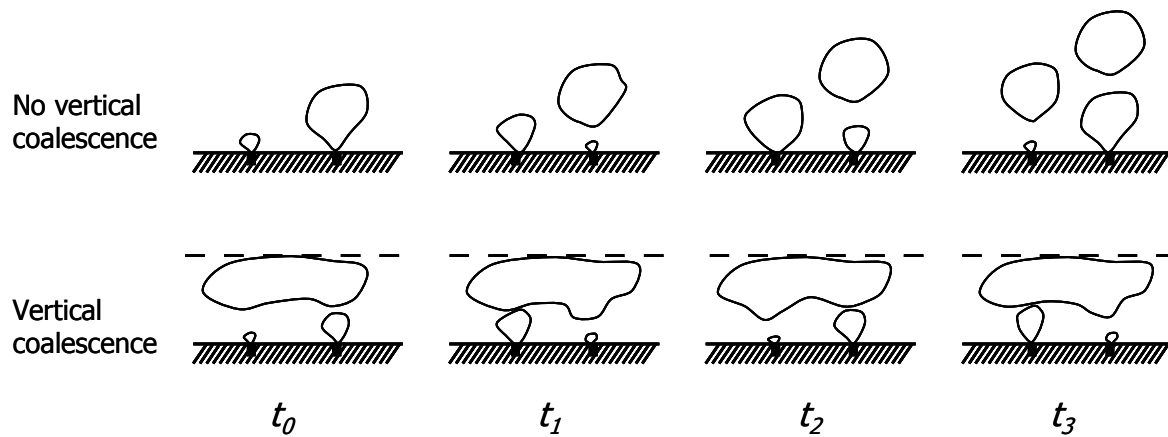


Figure 4.6 – Schematic representation of vertical vapour bubble coalescence stimulation by restraining the rise of the secondary vapour bubble, Zhao *et al.* (2003).

In regular pool boiling vertical coalescence between the primary and secondary bubbles occurs as well, however the mesh stimulates this type of coalescence. The spacing between the boiling surface and the mesh influences the vertical coalescence enhancement. The smaller the spacing the sooner the vertical coalescence occurs, see Figure 4.7. However, the mesh should not be placed too close to the boiling surface, since its presence may result into dry-out of the boiling surface invoking an early CHF. An optimal spacing of 3mm is reported.

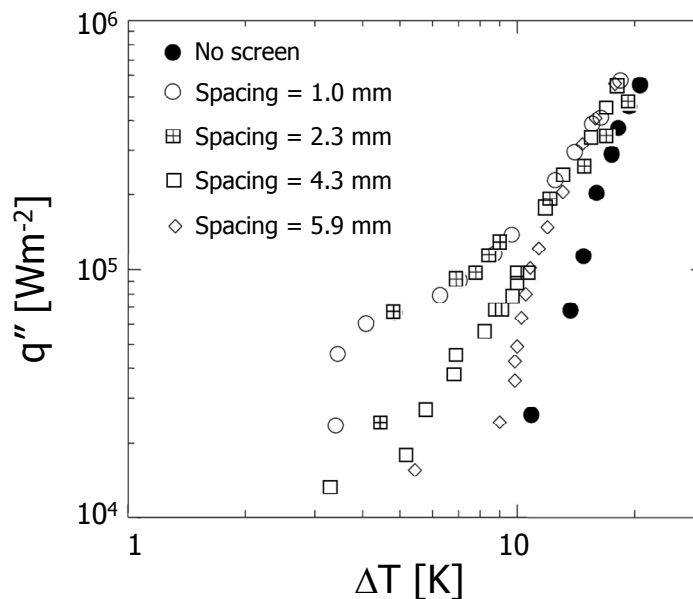


Figure 4.7 – Heat flux versus wall superheat for a tight wire mesh (wire distance 1.23mm) placed with different spacings above the copper boiling surface, boiling liquid water – data taken from Zhao *et al.* (2003) – .

At increasing wall superheats the horizontal and inclined coalescence effects take over due to the increased nucleation site density. This causes the boiling curves to overlap again at higher wall superheats.

Kim *et al.* (2006) increase the vapour bubble (Boiling liquid: FC-72) detachment frequency by reducing the width of their platinum wire heater (390 $\mu$ m, 75 $\mu$ m and 25 $\mu$ m). The reduction of the wire width reduces the surface tension forces that attach

the vapour bubbles to the boiling wire. This reduction increases the bubble detachment frequency. By means of their consecutive-photo method, they measured an average detachment frequency of about  $1 \cdot 10^6 \text{ Hz/m}^2_{\text{boil.surf.}}$  in case of the  $390 \mu\text{m}$  wire. While for the  $75 \mu\text{m}$  and  $25 \mu\text{m}$  wires  $8 \cdot 10^6$  and  $4 \cdot 10^7 \text{ Hz/m}^2_{\text{boil.surf.}}$  are the measured frequencies on average, Figure 4.8.

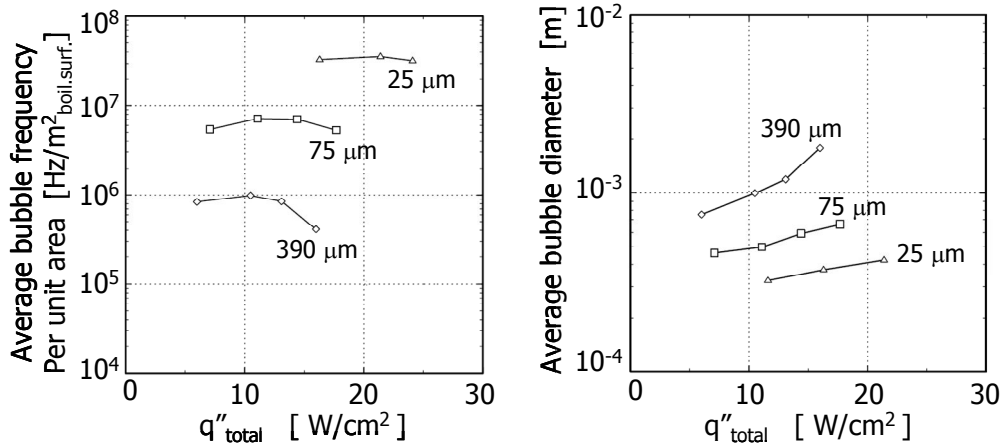


Figure 4.8 – FC-72 vapour bubble characteristics. Left: average bubble detachment frequency; Right: average bubble diameter on detachment; – data taken from Kim et. al. (2006) –

#### 4.1.3 HEATER SIZE EFFECTS

There are several modes of heat transfer: overall natural convection, local convection around the vapour bubbles near the surface, and latent heat. Their relative importance shifts between boiling stages. Kim *et al.* (2006) measured the total nucleate boiling heat transfer (FC-72) for thin wires, the average vapour bubble detachment frequency and the average bubble diameter using a high speed consecutive photo technique. Hence they estimated the contribution of the latent heat to the total heat transfer, see Figure 4.9. The multiple coalescence (vertical and inclined) of the primary vapour bubbles for the  $390 \mu\text{m}$  wire complicate the estimation of the latent heat flux by the primary bubbles.

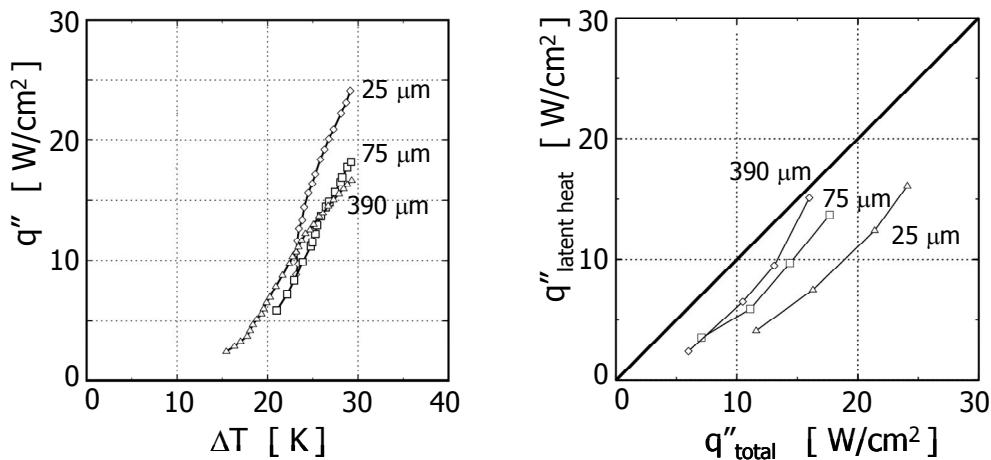


Figure 4.9 – FC-72 Boiling behaviour at varying wire thickness. Left: the total heat transfer as a function of the wall superheat; Right: latent heat portion as a function of the total heat transfer. – data taken from Kim et al (2006) –

As shown by Figure 4.9 the latent heat contribution decreases as the size of the wire decreases, although the measured overall heat flux increases in the nucleate boiling regime. Therefore it may be concluded that the heat transfer through the liquid is improved for smaller wires. The authors attribute this increase to the higher bubble detachment frequency, which thins the superheated liquid layer along the boiling wire.

Henry and Kim (2004) report their findings on the effect of the heater size, subcooling and gravity level on FC-72 pool boiling heat transfer. A square array of 96 heaters is constructed of which each heater can be controlled individually. Video recordings were taken (at a framing rate of 29.97 Hz) of the growing vapour bubbles, simultaneously from the bottom and from the side.

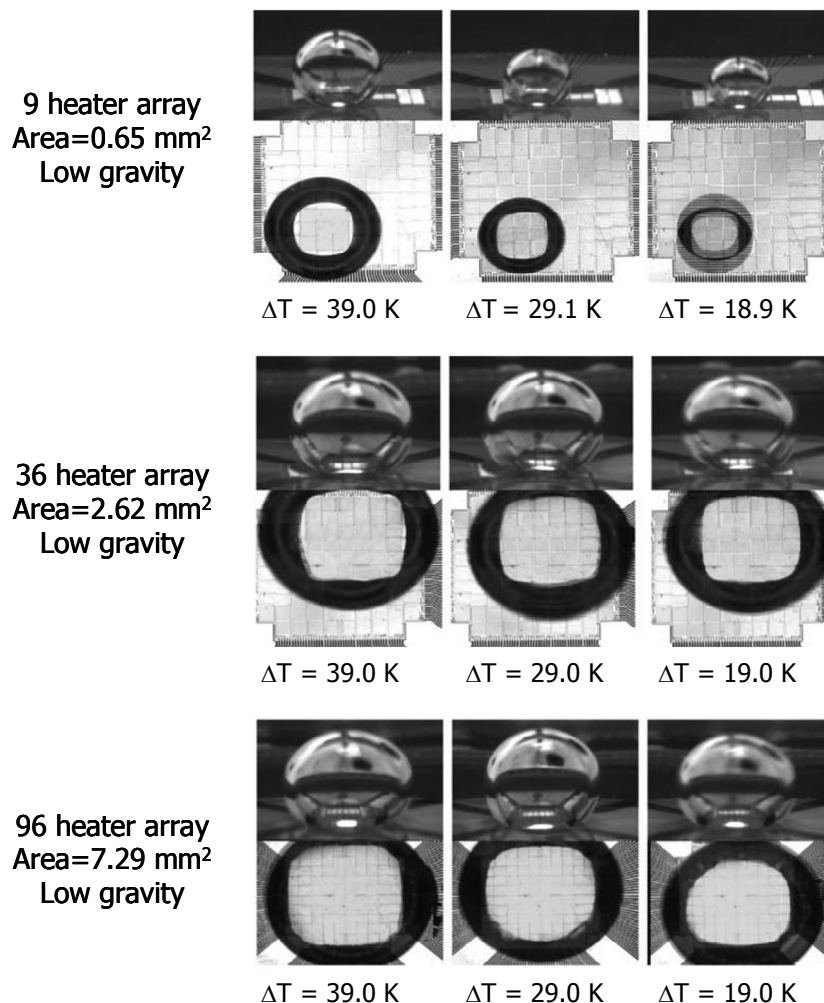


Figure 4.10 – Boiling pictures (bottom and side view) for three heater arrays in low gravity ( $\pm 0.01g$ ) and low subcooling ( $\pm 6K$ ), boiling liquid FC-72. – images taken from Henry and Kim (2004) –

Figure 4.10 shows the boiling results in a low gravity field ( $\sim 0.01 g$ ). Due to the low gravity the main bubble detachment force (buoyancy) is minimised. Therefore, regardless of the heater size or wall superheat the complete heater is covered by one (large) bubble. Due to the heater dryout, the boiling heat transfer capacity is poor.

The boiling behaviour in case of an increased vapour bubble detachment force (high gravity:  $\sim 1.8\text{ g}$ ) is shown in Figure 4.11.

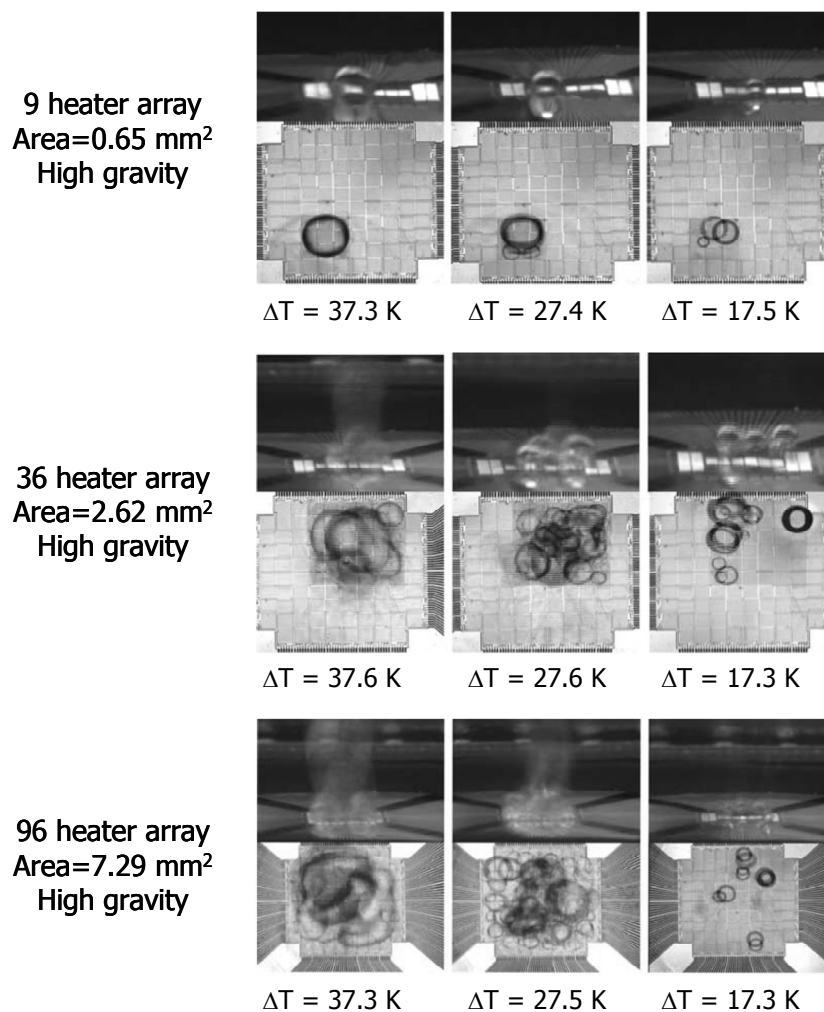


Figure 4.11 – Boiling pictures (bottom and side view) for three heater arrays in high gravity ( $\pm 1.8\text{g}$ ) and little subcooling ( $\pm 8\text{K}$ ), boiling liquid FC-72. – images taken from Henry and Kim (2004) –

The high gravity boiling visualisations show that for the smallest heater (area= $0.62\text{ mm}^2$ ) one single bubble may be formed causing heater dryout. For the larger heaters (with an area larger than  $2\text{ mm}^2$ ) no single bubble formation is observed, although the 36 heater array shows a similar tendency for the highest wall superheat,  $\Delta T=37.6\text{ K}$ .

From these observations the trivial conclusion can be drawn that if the heater size is more or less equal to the detachment bubble size, the heater is likely to be covered by a single vapour bubble. The heater dryout results in a poor heat transfer capacity.

#### 4.1.4 LITERATURE DISCUSSION

Although it is impossible to eliminate all interactions of the various boiling phenomena, the following may be concluded from the above literature: the more nucleation sites, the higher the nucleate boiling heat transfer becomes. The higher

the bubble detachment frequency, the higher the nucleate boiling heat transfer becomes. The smaller the heater, the more likely dry-out occurs, reducing the nucleate boiling heat transfer.

In the present research not only is the size of the heater plate varied, but the boiling pot is limited to the area of the heater as well. If the size of the boiling pot is reduced the number of active nucleation sites decreases as well. Therefore, as a first thought, this will lead to a decrease in heat transfer, as observed by Henry and Kim (2004). However, confining the boiling pot to the heater area limits the possibilities for the liquid flow to reach the heated surface. Our observations described below indicate that a change in overall fluid flow structure induces an increase of the nucleate boiling heat transfer on reducing the boiling pot diameter.

## ***4.2 Experimental***

To investigate the nucleate boiling in a spatially confined geometry we performed heat transfer measurements in various confined boiling configurations. Boiling pots with a diameter varying from 4.5 mm to 15 mm are constructed and used for heat transfer measurements.

### 4.2.1 EXPERIMENTAL SETUP

Since all measurement setups are constructed in a similar manner, only the measurement setup of the smallest pool boiling configuration will be discussed in detail.

The heat transfer as a function of wall superheat for confined boiling is measured in a pool boiling configuration realised by a cylindrical Teflon bounding wall that is placed watertight around a small copper rod. This results in a 4.5 ( $\pm 0.05$ ) mm diameter copper boiling surface ( $\lambda = 390$  W/mK) with a 2 mm high cylindrical thermally non-conducting Teflon wall ( $\lambda \sim 0.3$  W/mK). The hydrophobic Teflon prevents the water from creeping out and its low thermal conductivity ensures that all heat is dissipated at the bottom of the boiling pot. A schematic is shown in Figure 4.12.

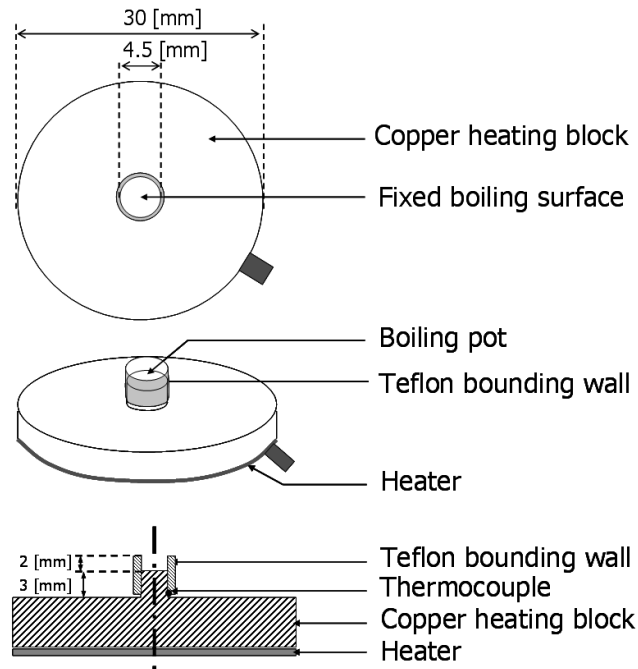


Figure 4.12 – Schematic overview of experimental setup for confined pool boiling. Top: top view; Middle: overhead view; Bottom: cross-section. A high boiling heat flux is ensured by the large size of the commercial heater placed at the bottom of a copper block. Similar experimental setups are made with boiling pot diameters of 5 mm, 6 mm, 8 mm, 10 mm and 15 mm.

The boiling pot is positioned on top of a larger copper block with an electrical heater at the bottom that can deliver a maximum heat flux of  $45 \text{ kW/m}^2$ . The boiling surface temperature is measured by a calibrated K-type thermocouple with a temperature range of  $80\text{-}125 \text{ }^\circ\text{C}$ , Figure 4.13A.

To keep the heat losses to a minimum, the set-up is properly insulated and covered in plastic to prevent the high temperature insulation material from wetting and thereby reducing its insulating property, Figure 4.13B.

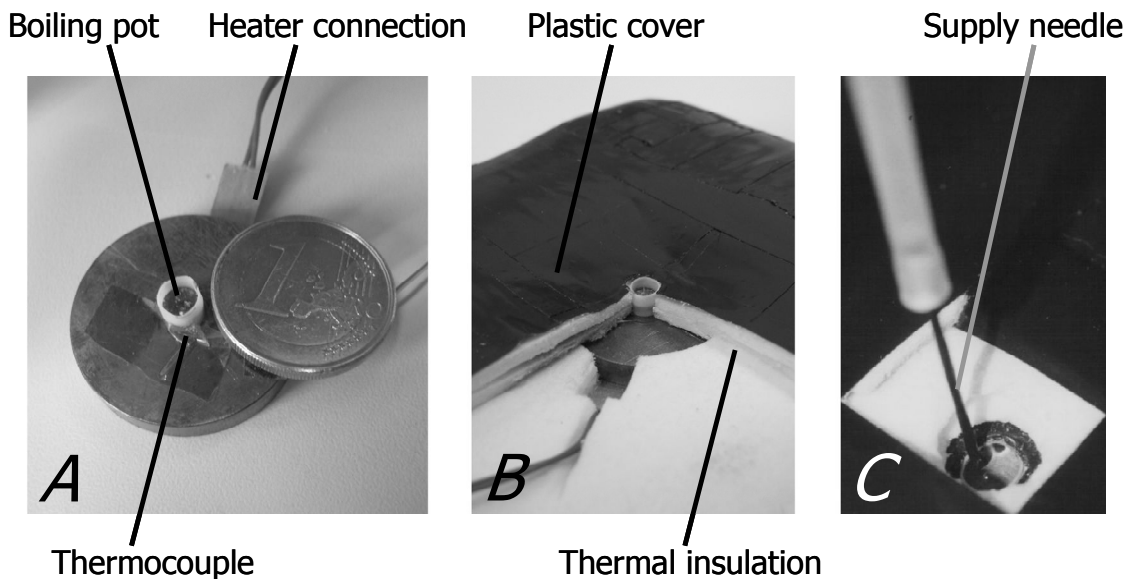


Figure 4.13 – The experimental set-up. A: copper block with 4.5 mm diameter cylindrical rod and Teflon bounding ring; B: partly insulated boiling pot; C: insulated small-scale boiling pot and water supply.

A constant water supply ensures that the boiling pot remains completely filled during the measurements. This water supply is provided by a flow controller (L1C2, Bronkhorst High-Tech) through a thin (0.35 mm diameter) Teflon-coated needle. The Teflon coating serves as insulation and minimises condensation on the needle, see Figure 4.13C.

#### 4.2.2 MEASUREMENT METHOD

The measurements are done by maintaining a steady heat input. The wall superheat measurement is valid when the steady state lasts for at least 19 minutes. This is the time required to fill or empty the smallest boiling pot at a flow rate of 0.1 g/h. At equilibrium the temperature remains constant within 0.1 K. At the critical heat flux the incoming water flow was about 40 grams per hour.

The wall superheat is measured using a single thermocouple. A small horizontal carve is made in the small copper rod to accurately position the thermocouple. In order to avoid influence of the thermocouple on the boiling process it is located  $2.5 \pm 0.1$  mm beneath the boiling surface. The thermocouple is in good thermal contact with the small copper rod and thermally insulated from the outside. The temperature of the boiling surface is deduced from the thermocouple reading, by taking into account the (one-dimensional) heat conduction in the copper rod.

The heat flux,  $q''$ , is determined by the electrical input power to the heater at steady state conditions when the exiting vapour flow is exactly balanced by the incoming water flow.

$$q'' = \frac{Q_{in} - Q_{loss}}{A} \quad (4.4)$$

$Q_{in}$  is the electrical power input [W] and  $Q_{loss}$  is the heat loss to the environment [W] and  $A$  is the boiling area of the pot [ $m^2$ ].

The heat losses of the insulated set-up at steady state are determined in two separate experiments. In the first experiment the heat loss equals the amount of heat needed to maintain a stable temperature ( $T=373-393K$ ) when no water is present. The second experiment determines the heat loss by the difference of the electrical power input and the evaporation enthalpy of the inflowing water at steady state conditions. Both methods indicate heat losses through the insulation of  $1.50 \pm 0.05$  W. This heat loss accuracy is equivalent to an apparent heat flux of  $3 \cdot 10^3$  W/ $m^2$ .

The water supply needle is placed against the inner side of the Teflon bounding ring to prevent a dropwise water supply. A Teflon insulation layer on the needle ensures a constant water flow at 293 K.

All measurements of the various confined boiling configurations are conducted in the same manner with similar experimental set-ups, thus maintaining the 2 mm pot depth. The confined boiling surfaces are prepared identically, first by sanding the copper boiling surface and then by aging it with several hours of boiling.

### 4.2.3 ANALYSIS OF MEASUREMENT ASSUMPTIONS

The validity of the one dimensional temperature approach in the small cylindrical rod is based on the fact that the heat flux through the boiling surface is much higher than the heat losses from the sides of the little rod. By means of numerical simulations (using the commercial CFD code Fluent) the temperature in the copper block is calculated while taking into account the heat losses. These calculations show the appropriateness of the assumption that the temperature gradient in the little copper rod is one dimensional, Figure 4.14.

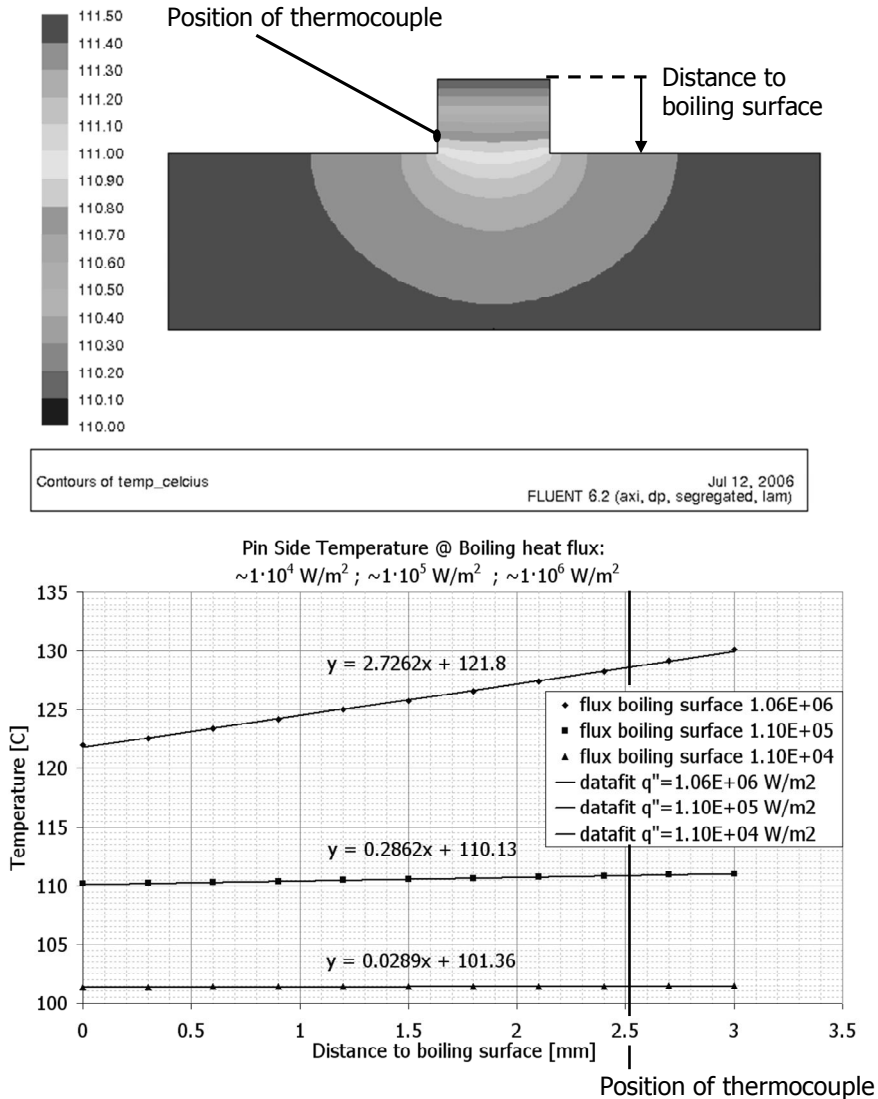


Figure 4.14 – The temperature profiles from three heat loads of the copper block calculated using the CFD code FLUENT. For the complete range of boiling heat fluxes a linear temperature profile is found all along the cylindrical pin. A realistic heat transfer coefficient of  $1 \text{ W/m}^2\text{K}$  for the heat losses is assumed.

The heat losses through the insulation are modelled assuming a realistic value for the heat transfer coefficient,  $h = 1 \text{ W/m}^2\text{K}$ . The temperature profile along the cylindrical pin is linear corresponding to a one dimensional situation. The heat conductivity,  $\lambda$ , can be estimated from the constant temperature slope,  $dT/dl$ , and the assumed boiling heat flux,  $q''$ :

$$\lambda = \frac{q''}{dT/dl} \quad (4.5)$$

The heat conductivity of the cylindrical pin estimated from the constant temperature slope along the pin varies within 3% of the actual value ( $\lambda=390$  W/mK). Even if the heat transfer coefficient used in the CFD calculation is raised to  $h = 10$  W/m<sup>2</sup>K, which corresponds to a non-isolated situation (Schlünder *et. al.* 1994), at boiling heat fluxes above  $1 \cdot 10^5$  W/m<sup>2</sup> the error to estimate the thermal conductivity is within 5%.

The limited influence of possible subcooling of the boiling pool is caused by the thorough mixing in the liquid boiling pool. From high speed camera visualisation the boiling water is observed to revolve in less than 0.1 seconds. This is assumed to be the time to mix the supply flow with the boiling water. The supplied water flow during the mixing time and the total water mass present in the boiling pot determine the average water temperature. For example, in case of the smallest boiling pot (volume =  $3.18 \cdot 10^{-8}$  m<sup>3</sup>) and a water supply rate of 10 g/h (note 40 g/h is supplied at CHF) the average liquid temperature is 99.3 °C. Zuber's relation (Rohsenow 1971) incorporates the effect of subcooling for the critical heat flux. For water at standard boiling conditions this relation simplifies to:

$$\frac{q''_{sub}}{q''_{sat}} = 1 + 0.05 \cdot (T_{sat} - T_{liq}), \quad (4.6)$$

where  $q''_{sub}$  is the heat flux at subcooled conditions and  $q''_{sat}$  is the heat flux for saturated pool boiling. This means that for up to two degrees of liquid subcooling the critical heat flux will not be affected by more than 10%. Since to the author no relation for the influence of subcooling in the complete nucleate boiling regime is known, we assume that this relation holds for the nucleate boiling regime as well.

During the nucleate boiling some droplets splash out the boiling. The splashing of liquid droplets has in principle no effect on the establishment of the boiling curve, since the heat flux is determined from the electrical power input. The amount of splashing is estimated in two ways: first, by high speed camera recordings and second by the difference in the evaporation enthalpy and the electrical power supply:

$$\frac{m_{splashing}}{m_{supply}} = 1 - \left( \frac{Q_{in} - Q_{loss}}{h_{ev} \cdot m_{supply}} \right), \quad (4.7)$$

where  $m_{splashing}$  is the mass of the water droplets splashing out the boiling pot,  $m_{supply}$  is the water supplied to the boiling pot through the supply needle,  $Q_{in}$  is the electrical power input, and  $Q_{loss}$  is the estimated heat loss to the environment.

In the maximum enhancement region ( $7 < \Delta T < 13$  K) the splashing is estimated to be less than 10% of the total water input. Only at higher wall superheats the splashing may reach values up to 30%.

Overviewing all error sources (such as uncertainties in the boiling surface area, in the surface temperature due to the actual position of the thermocouple, the electrical power input, the estimate of the heat loss, and the water subcooling) it is estimated that the combined error in the measured heat flux is about 15%. In case all errors simultaneously increase or decrease the measurement result, then the total measurement error is expected to be no greater than approximately 30%. This could lead to an uncertainty in the measured heat transfer enhancement factor of 1.3, which is well below the actually measured heat transfer enhancement of 5 to 10 times, see section 4.3.1.

## **4.3 Results**

### 4.3.1 MEASUREMENT RESULTS

The pool boiling curves measured for various pot diameters ranging from 4.5 to 15 mm are shown in Figure 4.15.

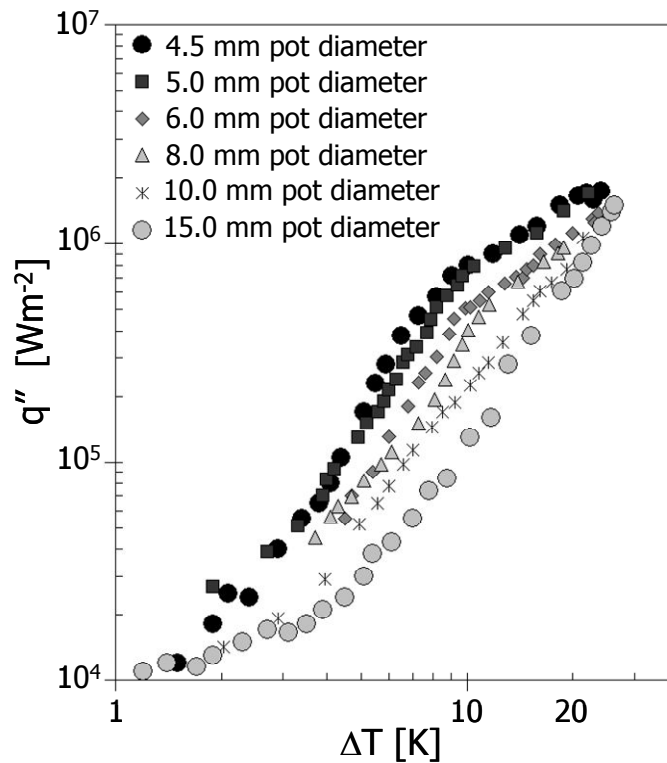


Figure 4.15 – Measured heat flux,  $q''$ , as a function of the difference  $\Delta T$  between the wall temperature and the saturation temperature of the fluid on confining the boiling area. Experimental results for various boiling pot diameters: 4.5mm (Confined pool boiling), 5mm, 6mm, 8mm, 10mm and 15mm (Unconfined pool boiling). The confined pool boiling results show a significantly different behaviour with an enhancement of the heat flux up to 10 times the unconfined heat flux.

Upon decreasing the diameter of the boiling area an enhancement of the nucleate boiling heat flux is observed. The increase of the heat transfer is noticeable by the different shape of the confined pool boiling curves (which are convex) and the curves at regular scale (which are concave). At small temperature differences between the boiling surface and the saturation temperature ( $\Delta T \leq 2$  K), the heat fluxes for confined and unconfined pool boiling are equal and show the same trend. At  $\Delta T \sim 3$  K the boiling curve for the small boiling pot starts to deviate from the unconfined pool boiling curve. The heat flux in the spatially confined geometry increases rapidly, and at wall superheats of 7–13 K the spatially confined heat flux enhancement is maximal. Depending on the boiling pot diameter the confined heat flux is up to ten times higher than the heat flux for unconfined pool boiling. At large wall superheats ( $\Delta T > 20$  K) the confined pool boiling and unconfined pool boiling heat fluxes become the same order of magnitude again. The heat flux enhancement relative to the unconfined pool boiling heat flux (15mm pot diameter) is displayed in Figure 4.16.

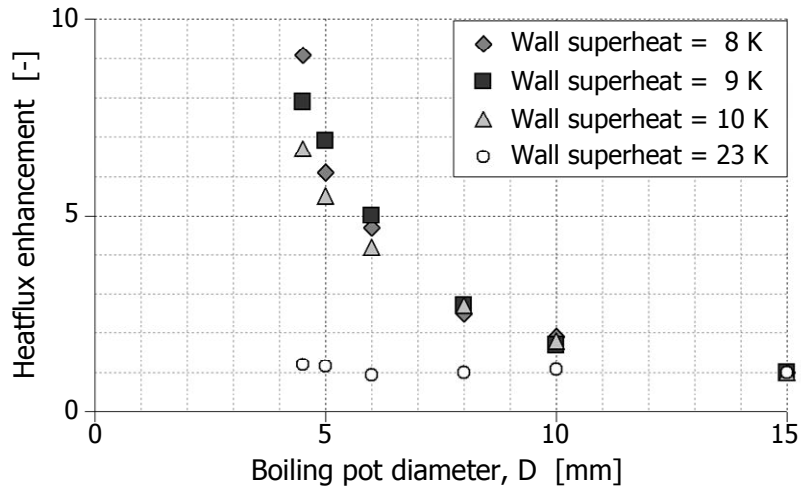


Figure 4.16 – The heat flux enhancement as function of the confinement by the boiling pot diameter at different wall superheat.

The Bond number for boiling pot with a diameter of 4.5 mm equals unity. Therefore, within smaller boiling pots the vapour bubbles are likely to become of the size of the boiling pot, promoting heater dry-out. Boiling curve measurements with larger boiling pot diameters (20mm and 25 mm) coincide with the 15mm diameter boiling pot results.

#### 4.3.2 COMPARISON OF THE RESULTS

To investigate if the enhancement is due to the confinement, the measurement setup was first verified by comparing our measurements (both unconfined,  $\varnothing 15\text{mm}$ , and confined,  $\varnothing 4.5\text{mm}$ ) with results obtained by others (Rao and Balakrishnan 2004; Raykoff and Kandlikar 1997; Lee *et. al.* 1994; McGillis *et. al.* 1990). The results are shown in Figure 4.17.

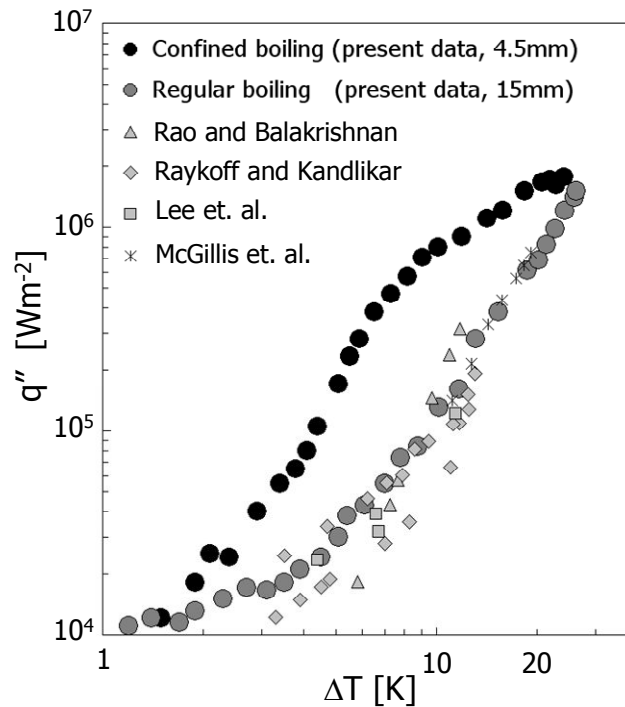


Figure 4.17 – Measured heat flux,  $q''$ , for confined and unconfined pool boiling as a function of the difference  $\Delta T$  between the wall temperature and the saturation temperature of the fluid. Our experimental results for unconfined pool boiling coincide with existing results, but our confined pool boiling results show a significant different behaviour. The results are independent of variations in the experimental configuration.

The confined pool boiling results show a significantly different behaviour from the literature results. Rao and Balakrishnan (2004) and Raykoff and Kandlikar (1997) performed water pool boiling experiments using a aluminium heater plate. Lee et. al. (1994) and McGillis *et. al.* (1990) used a copper surface to measure the boiling curve. The unconfined boiling pot results are in agreement with the results given in the literature. This agreement justifies our experimental method for the measurement of the heat flux.

#### 4.3.3 MEASUREMENT SET-UP VARIATION

To ensure that the heat transfer enhancement is independent of fluid, geometry, material and other conditions, several changes in the experimental configuration are carried out:

1. variation in liquid: iso-propanol,
2. variation in pot depth or aspect ratio,
3. material variation of the bounding wall,
4. variation in the diameter of the inlet water supply.

The confined pool boiling curve is measured using water and a 4.5mm boiling pot ( $Bo=1$ ). By changing the boiling fluid into iso-propanol the fluid-vapour behaviour will be different. Therefore for the confined boiling situation a boiling pot with a

diameter of 3mm is created ( $Bo=1$ ). For the unconfined pool boiling situation the 15mm diameter boiling pot is used. The results are shown in Figure 4.18.

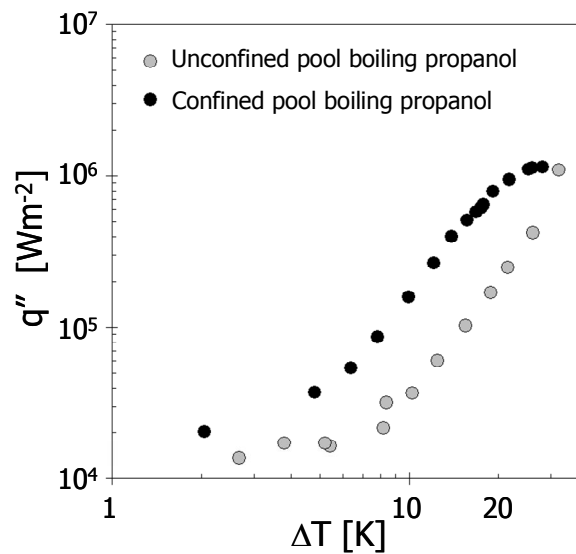


Figure 4.18 – Measured heat flux,  $q''$ , as a function of the difference  $\Delta T$  between the wall temperature and the saturation temperature of iso-propanol. Confined pool boiling (3mm pot diameter) vs. Unconfined pool boiling (15mm pot diameter).

Figure 4.18 shows that also in case of iso-propanol a heat transfer enhancement occurs during the nucleate boiling stage. For both low wall superheats ( $\Delta T < 4$  K) and high wall superheats ( $\Delta T > 30$  K) the measured heat flux towards the fluid are similar. However, at wall superheats between 10 K and 20 K a heat transfer enhancement of a factor of 5 is found.

The influence of the boiling pot wall material is investigated by changing the bounding wall material from hydrophobic (Teflon, nominal contact angle  $\sim 115^\circ$ ) to hydrophilic (PMMA, nominal contact angle  $\sim 73^\circ$ ).

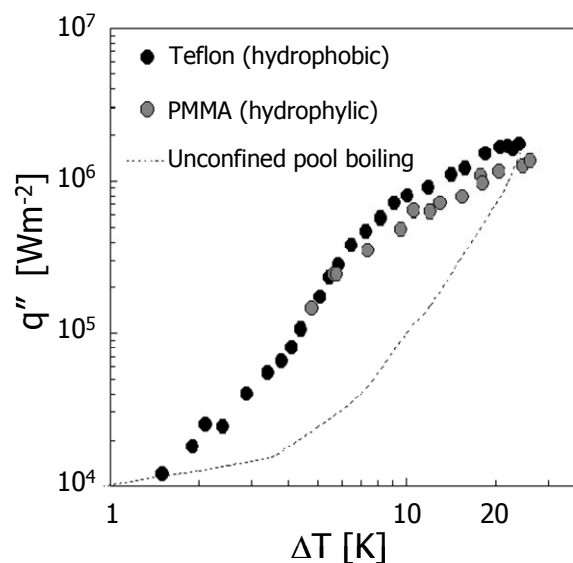


Figure 4.19 – Measured heat flux,  $q''$ , for spatially confined and unconfined boiling as a function of the difference  $\Delta T$  between the wall temperature and the saturation temperature of the fluid. Experimental results for the two different bounding wall materials (Teflon “original” and PMMA) show similar boiling curves.

The boiling curve measured with a 2 mm high PMMA bounding wall in Figure 4.19 shows a similar behaviour as the measurements using a 2 mm Teflon bounding wall. For low wall superheat temperatures no data points are shown since no stationary state could be identified within the 19-minute time interval observed for all other data points.

To investigate the influence of the boiling pot depth two additional pool boiling pots are produced with pot depths of 4mm and 6mm. The results of this variation in the height of the bounding wall, 2 mm (= "original"), 4 mm and 6 mm, are given below.

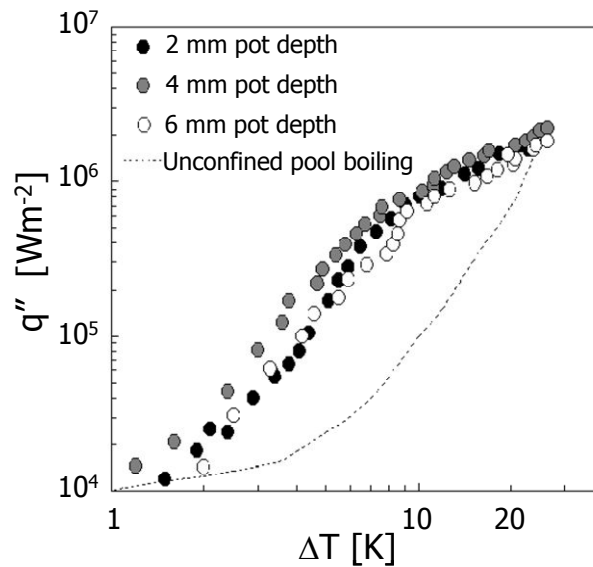


Figure 4.20 – Measured heat flux,  $q''$ , for spatially confined and unconfined boiling as a function of the difference  $\Delta T$  between the wall temperature and the saturation temperature of water. Experimental results for the various confined boiling pot depths (2 mm "original", 4 mm and 6 mm) show similar boiling curves.

Figure 4.20 shows that the depth of the boiling pot has only a minor influence on the shape of the confined pool boiling curve. This indicates that at the "original" geometry there is no distinct interaction between flow structures, heat transfer mechanism and boiling pot wall with respect to height.

The possible effect of the water inflow velocity is investigated by altering the inner diameter of the supply needle. (e.g.  $\phi_{m\_supply}=2$  g/h:  $u_{0.2\_diam}=0.017$  m/s,  $u_{0.35\_diam}=0.006$  m/s,  $u_{0.5\_diam}=0.003$  m/s).

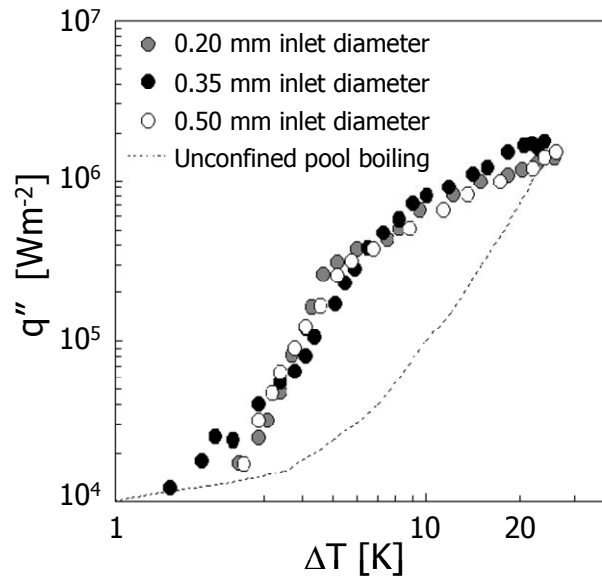


Figure 4.21 – Measured heat flux,  $q''$ , for spatially confined and unconfined boiling as a function of the difference  $\Delta T$  between the wall temperature and the saturation temperature of water. Experimental results for the various water supply diameters (0.2 mm, 0.35 mm “original” and 0.5 mm) show similar confined pool boiling curves.

From the above results in Figure 4.21 it is concluded that the influence of the inlet velocity is not significant. This may be explained by the fact that the bubble velocities ( $u_{\text{bubbles}} \sim 10^{-1}$  m/s) are approximately one order of magnitude higher than the liquid supply velocities. These bubble velocities are estimated by bubble tracking from digital high speed recordings of the top bubbles and correspond generally to values found in literature (e.g. Mingming and Morteza 2002; Moghaddam and Kiger 2004).

Also the location of the supply needle did not alter the confined pool boiling heat transfer. Whether the supply needle was positioned at the left, right or centre of the boiling pot, a strong circulating flow was observed. Only if the needle did not make contact with the boiling water, the relatively large droplets formed at the needle tip could break down the flow pattern. Due to these relatively large droplets dripping in the small boiling pot, a proper 19 minute stable period could not be obtained.

#### 4.3.4 HIGH SPEED CAMERA VISUALISATION

We investigated the spatially confined boiling by observing the flow patterns in the boiling thin water layer of the unconfined boiling pot and the confined boiling pot with high-speed video imaging (Photron Ultima APX, 1000x1000 pixels spatial resolution, at a rate of 1000 fps). The camera was positioned at an angle of approximately  $40^\circ$ , allowing images of the top of the boiling water, which can be used to obtain information on the vertical direction of the bubble motion. A large working distance (ca 20cm) was applied to prevent vapour condensation on the lens (Rhodenstock 0.8x - 4.0x macro lens). The motion of the bubble patterns is studied by tracking vapour bubbles (Particle Tracking Velocimetry, PTV). At a wall superheat of 7 K (near the maximum enhancement in heat transfer) the video sequences show a structured and circulating flow for the spatially confined boiling set-up, see Figure

4.22. In the unconfined boiling set-up a more chaotic and mainly upward motion is observed.

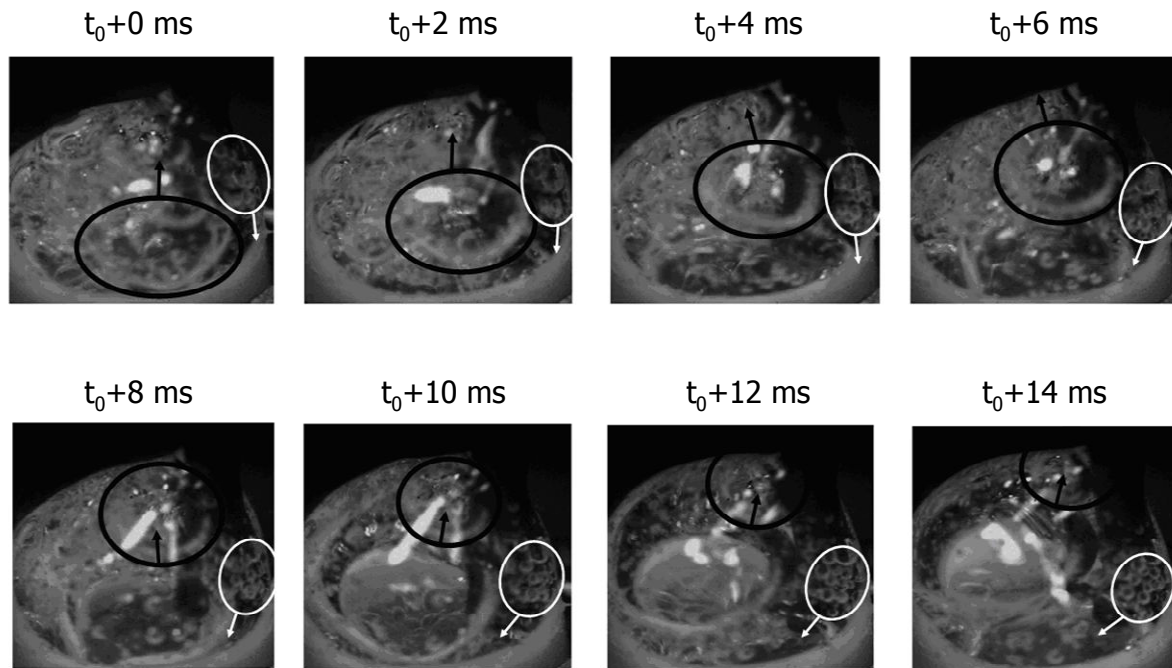


Figure 4.22 – High-speed visualisation of the confined pool boiling (pot diameter: 4.5mm) at wall superheat of 7 K. The black circles show the position of a bubble at the front side of the boiling pot, while the white circles mark the position of a group of bubbles at the rear-side in time. The relative motion of the front and rear side bubbles show the circulating behaviour of the flow.

## 4.4 Discussion

### 4.4.1 THE CONFINED POOL BOILING MECHANISM

The observed circulating bubble flow can explain the heat transfer enhancement. In the wake of the rising bubbles liquid is efficiently moved away from the heated surface, while in the gaps between the rising bubbles, due to continuity of mass, colder liquid flows towards the heated surface. In the unconfined situation the chaotic and random motion of bubbles impedes the flow of cooler liquid towards the heated surface, while for spatially confined boiling a structured, circulating motion of much smaller vapour bubbles is observed. This circulating motion of the liquid, as shown in Figure 4.22, sweeps the vapour bubbles more quickly. This leads to the creation of smaller vapour bubbles, yet at a higher frequency. The wall-normal liquid entrainment at the boiling surface is enlarged and hence increases the heat transfer towards the fluid.

Kandlikar (2002) investigated the influence of the liquid flow on the bubble growth and detachment size and he showed that an increased flow leads to smaller bubble detachment sizes and a faster bubble growth. Kim *et. al.* (2006) amongst others (e.g. Zhao *et. al.* 2003; Wu *et. al.* 1998) noted that an increased bubble detachment frequency leads to an increase in heat transfer.

To understand the change in flow pattern, we consider the detailed nucleation process of the vapour bubbles. The origin of the stable circulating motion may be found in the nucleation site density, which is the number of active nucleation sites per unit area. Qi and Klausner (2006) report 13 active sites per square centimetre at the start of the nucleate pool boiling regime for water and copper. Basu et. al (2002) mention similar active nucleation site densities in case of flow boiling. At increasing wall temperature this number grows two orders of magnitude (e.g. Basu et. al. 2002; Sakashita and Kumada 2001; Benjamin and Balakrishnan 1997). Consequently, only very few, and possibly just one, active sites are present in our experiments for the spatially confined boiling measurements, while for the unconfined set-up a tenfold of active sites are present.

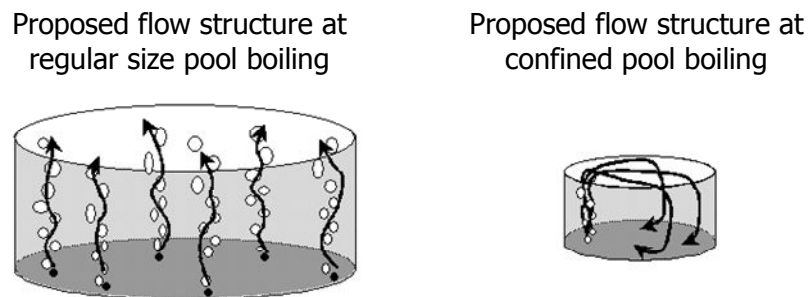


Figure 4.23 – Visualisation of hypothesis for explanation of existence of the circulating motion in confined pool boiling. Left: unconfined pool boiling situation, chaotic motion. Right: confined pool boiling situation, circulating flow.

Figure 4.23 (left) schematically shows the chaotic motion induced by the multiple nucleation sites at unconfined pool boiling. The image on the right visualises how the singularisation of the nucleation in confined pool boiling allows the formation of a bubble column above the active nucleation site that acts as a stable driving mechanism for a steady circulating motion.

The formation of circulation cells on a larger scale is observed by Beek (1965) in bubble columns. Similarly, Mudde (2005) discusses the formation of circulation cells in gravity driven bubbly flows.

At larger wall superheats more nucleation sites become active in the confined pool boiling pot as well. As a result, the circulating flow pattern breaks down as multiple bubble columns counteract each other. The pattern breakdown leads to a decrease of the enhancement effect and the confined boiling heat flux approaches the unconfined critical heat flux.

#### 4.4.2 OUTSCALING OF CONFINED POOL BOILING

The confined pool boiling mechanism is interesting, especially since it efficiently enhances the nucleate boiling heat transfer without reducing the final critical heat flux. In case of the confined boiling curve the heat flux does not drop as fast as in case of the unconfined boiling heat flux on lowering the temperature below CHF-temperature. Therefore it is profitable to run a device at a lower temperature, which creates a larger safety margin towards CHF. Due to the boiling pot miniaturisation the heat transferring area is small. However, by outscaling (also known as

numbering up) the confined pool boiling situation, this heat transfer mechanism can be applied for larger areas as well.

Within the present work the actual outscaling of the confined pool boiling experiment is realised by dividing a large circle ( $\text{\O} 26\text{mm}$ ) into 8 equal segments. Each segment is separated through a 2 mm thick wall. This wheel with spokes is 5 mm in height and made out of Teflon, Figure 4.24.

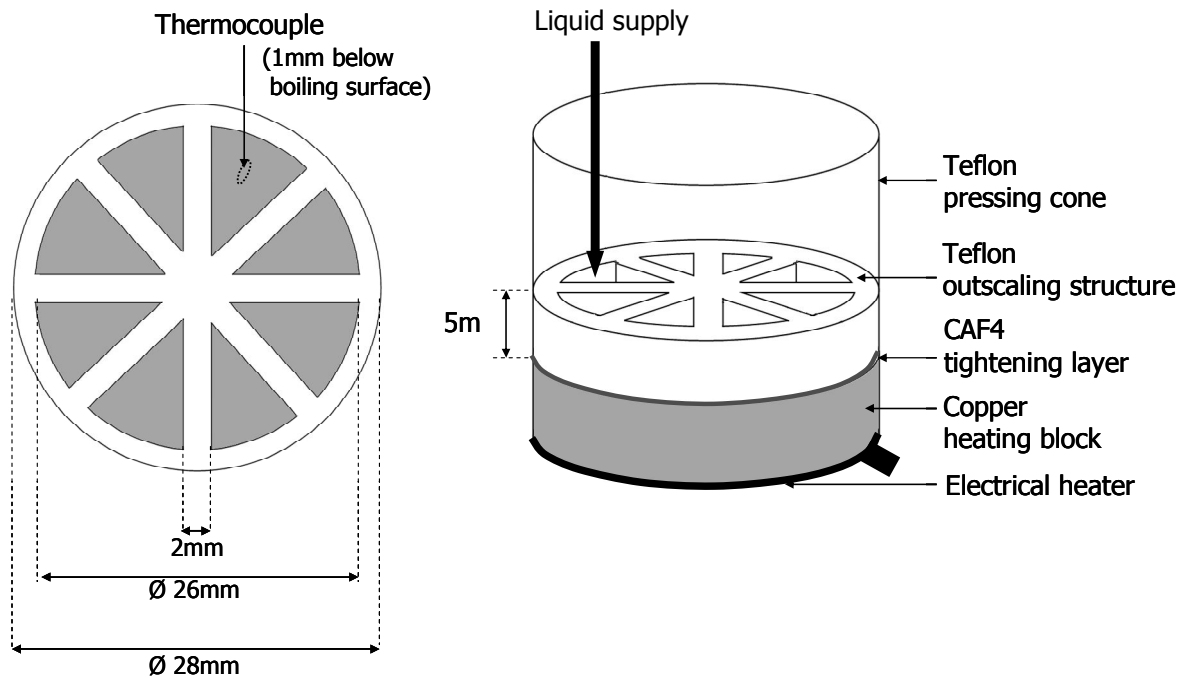


Figure 4.24 – Schematic overview of the outscaling set-up of the confined pool boiling mechanism. Each boiling segment has a 6.2mm equivalent pot diameter.

The eight boiling pots are formed by pressing the Teflon wheel tight onto a heated copper block. A thin layer of a silicon based synthetic (CAF4) is attached to the lower part of the Teflon wheel. The synthetic adjusts itself completely to roughness of the copper surface and the Teflon wheel, which prevents leakage underneath the Teflon spokes. This ensures that the participating boiling surface is limited only to the bottom copper surface of the eight segments.

A high power electrical heater (Betronic, ceramic thick film heater) provides the boiling energy. The complete setup (heater, copper block, Teflon cone pressing the Teflon spoke wheel) is insulated to minimise the heat losses. The heat losses are measured in order to accurately determine the boiling heat flux.

The boiling surface temperature is measured by a calibrated K-type thermocouple. The thermocouple is positioned 1 mm below the boiling surface in the middle of a boiling segment.

All boiling segments are filled and flooded with a thin water layer ( $\pm 1$  mm) and remain flooded due to a constant water supply. This water supply (temperature = 293 K) is provided through the thin Teflon coated needle which is positioned just above the Teflon spoke wheel. At smaller thicknesses of the thin water layer above the boiling segments could lead to a temporary dry out of individual boiling

segments. At thick water layers the circulating motion within the boiling segments could not fully develop.

Figure 4.25 shows the result of the measured pool boiling curve in case of 8 boiling segments. As a reference the single boiling pot results with pot diameters 4.5 mm, 6 mm and 15 mm are given as well. Only the bottom surface of the boiling segments (i.e. the wetted area) is taken into account to estimate the boiling heat flux.

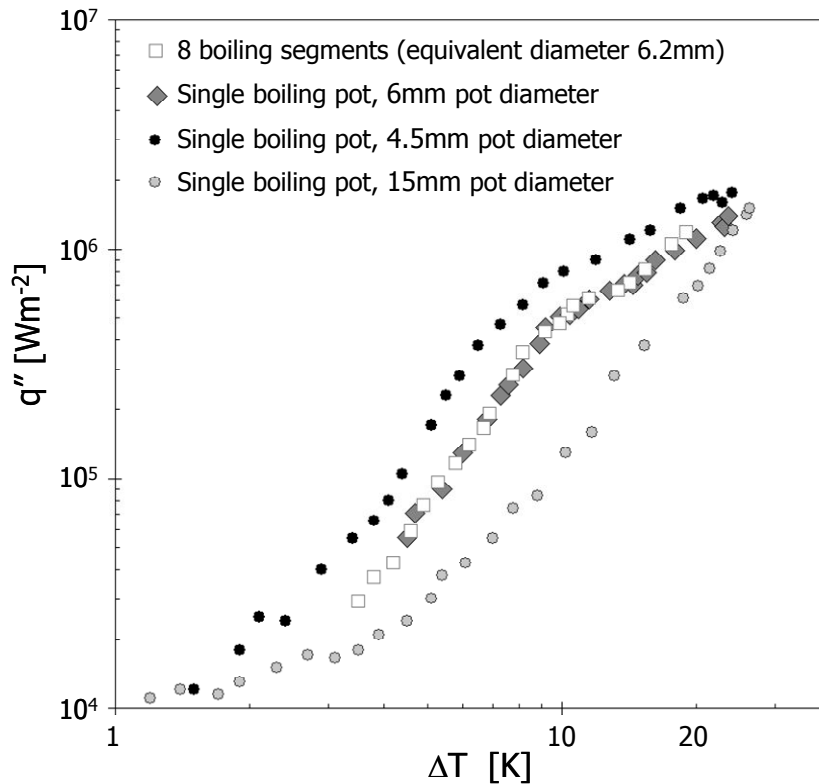


Figure 4.25 – Measured heat flux for multiple confined pool boiling segments, as a function of the wall superheat,  $\Delta T$ . For comparison the 4.5 mm, 6 mm and 15 mm diameter single boiling pot results are shown.

The multiple boiling pot result shows the confined pool boiling behaviour and overlaps with the 6 mm single boiling pot result. This overlap indicates that indeed not the boiling pot shape matters, but the confinement of the boiling area.

## 4.5 Conclusions

Our results on confined pool boiling demonstrate an enhancement of the nucleate boiling heat flux when the boiling pot diameter is decreased. With our analysis of possible errors and a variation of experimental parameters we could exclude that the observed enhancement is the result of the chosen boiling liquid, the variation in boiling pot depth, the material of the bounding wall, or the variation in the diameter of the inlet water supply. In the nucleate boiling regime the heat flux in confined boiling is between 5 to 10 times higher than the heat flux for unconfined pool boiling.

An explanation is found in the singularisation of the basic process for nucleate pool boiling, leading to a different flow behaviour. The flow pattern is chaotic in the case

of unconfined pool boiling, and it becomes directed and circulating as the dimensions of the confinement are reduced. The circulating fluid motion augments the entrainment of liquid by the vapour bubbles, and hence it significantly increases the heat transfer in the nucleate boiling regime.

Due to the enhancement, the heat flux does not show a rapid decrease for temperatures below the CHF. This allows an operation of the device at a comfortable temperature safety margin with respect to the critical superheat temperature without compromising too much in heat transfer capacity. When confined boiling would be integrated on a large scale (by means of 'scaling out'), it has the potential of improving the heat transfer efficiency and of reducing the energy consumption of industrial facilities and home appliances.



## 5 Boiling within small-diameter channels

Boiling within small diameter channels combines three aspects interacting with each other: Phase change heat transfer, two-phase flow and confining flow structures. Various literature is available on flow boiling in small-diameter channels. New opportunities are encountered making use of the high heat transfer on a small area. However, also drawbacks are encountered such as high pressure drops and flow instabilities. The high pressure drop is inherently connected to small-diameter channels. On the other hand the pressure, temperature and flow instabilities do not have this inevitable connection to small-diameter channel, and are therefore related to the design. In this chapter the research into the pressure fluctuations and possible flow reversal is described.

### 5.1 Present status

Before showing our results on boiling within small-diameter channels, a short overview is given. First some general aspects are discussed of small-diameter flow boiling and its observed instabilities. Next, a review is given dealing with confined vapour bubbles (slug bubbles) and their growth behaviour in small-diameter channels.

#### 5.1.1 SMALL-DIAMETER FLOW BOILING: INSTABILITIES

Two-phase flow instabilities can be classified into two groups: The first group are static instabilities such as flow excursion, boiling crisis, or relaxation instability; The second group are dynamic instabilities such as acoustic wave instability, density wave instability, or thermal oscillations (Tadrist 2007).

Understanding of the two-phase instabilities present in small-diameter flow boiling devices is beneficial for the design of the inlet and outlet manifold in multichannel evaporators. Design strategies with respect to premature dryout or critical heat flux conditions can be found. The evaporation of the liquid phase affects the flow in two ways. First, the effect of surface tension increases the probability for slug flow to occur. Second, the pressure drop is altered by the introduced acceleration term (Kandlikar 2004).

Many researchers observed an oscillating behaviour in a multi channel evaporator, like Hetsroni *et al.* (2000) in 21-26 parallel channels with hydraulic diameter ranging from 103  $\mu\text{m}$  to 129  $\mu\text{m}$ . Also, Peles *et al.* (2001) and Kandlikar and Balasubramanian (2003) noticed flow reversal in a multiple micro-channel evaporator. A vapour backflow example observed by Steinke and Kandlikar (2003), is shown in Figure 5.1. The water-vapour interface moves from the right to the left ( $8 < t < 40$  ms) while the overall flow direction is set from the left to the right.

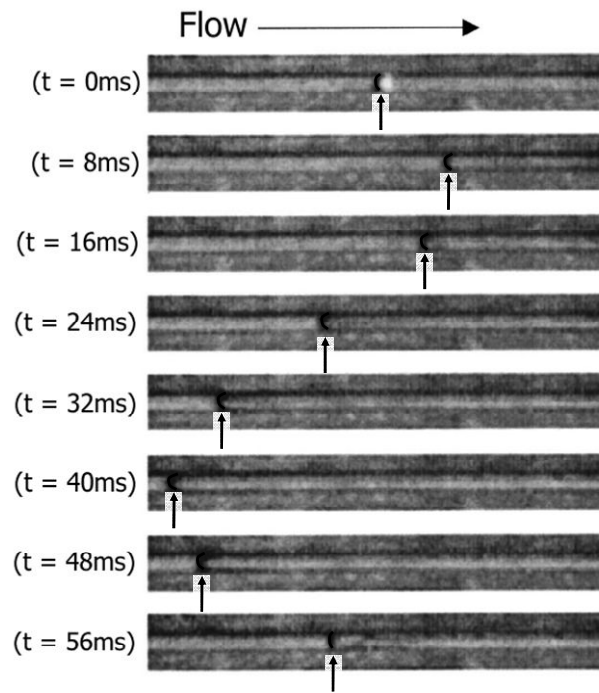


Figure 5.1 – Flow reversal in parallel microchannels. Water flow is from left to right, a single channel out of a multiple channel array is shown, Steinke and Kandlikar (2003).

This commonly observed flow instability within micro-channels cannot be explained by flow excursion also known as the Ledinegg instability, i.e. decreased pressure drop versus flow rate instability (Ledinegg 1938). Brutin *et al.* (2003) and Brutin and Tadrist (2004) performed flow boiling experiments in a single micro channel (with a hydraulic diameter  $D_h=889 \mu\text{m}$ ), see Figure 5.2.

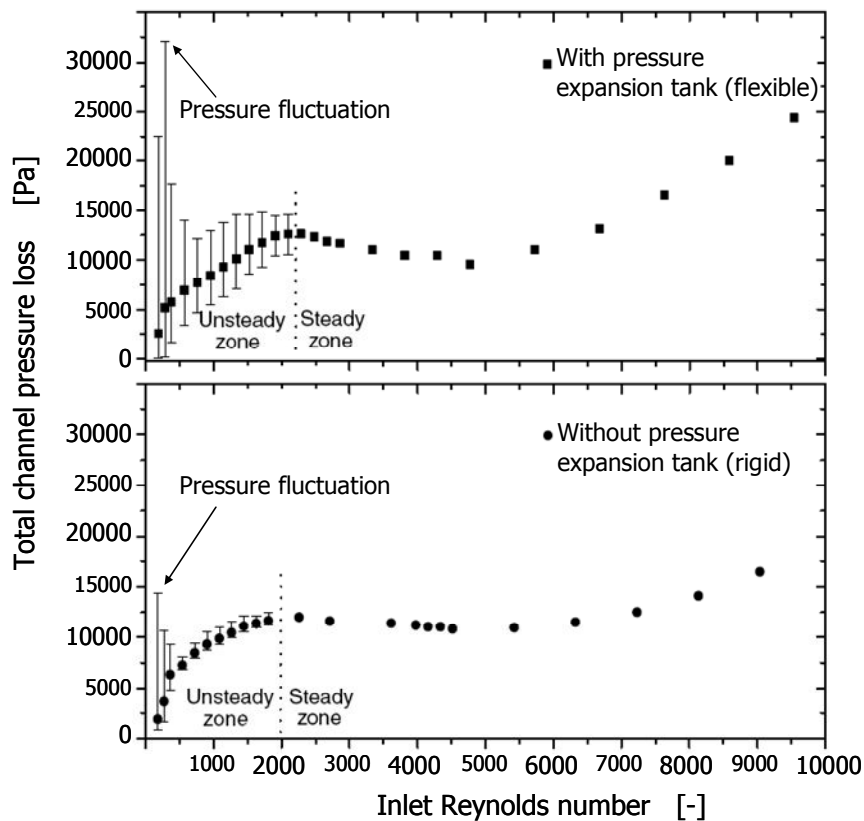


Figure 5.2 – Comparison of the micro-channel pressure loss with the pressure fluctuations between two upstream conditions of the flow boiling experiment. Top figure: flexible upstream conditions; bottom figure: rigid upstream conditions (Brutin and Tadrist 2004).

The pressure fluctuations are not encountered in the negative slope part, but only in the early rising part (i.e. low Reynolds mass flow) of the pressure drop curve. In case of a compressible delivery system (constant feed pressure) the fluctuations are larger than for a rigid delivery system (constant feed volume flow). These large fluctuations in case of the compressible delivery system are explained as a coupling effect between the expansion tank and the flow boiling channel. The smaller pressure fluctuations in case of the rigid delivery system are not explained by Brutin and Tadrist (2004).

Bergles *et al.* (2003) discusses various options for this flow instability and point out the importance of compressibility effects as well. A 'soft' (compressible) delivery system may augment incoherently the instabilities by interacting with the channel head-flow characteristic. At regular scale internal compressibility of very long channels ( $L/D > 150$ ) are known to cause pressure drop oscillations as well (Shapiro 1953). Micro-channels may well exceed this length. Although the effect is only investigated in conventional channels, this effect may occur in micro-channels as well.

Flow instabilities occur when the pressure drop in the upstream section is relatively small. The compressibility of the two-phase mixture, in the adjacent channels, acts in a manner similar to a flexible upstream section of a single evaporator tube. These instabilities have a significant effect on the pressure drop under flow boiling conditions, see Figure 5.3.

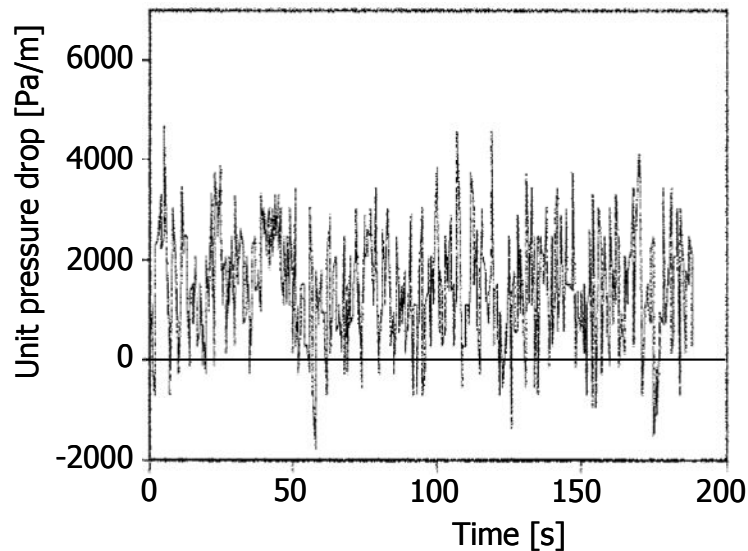


Figure 5.3 – Differential pressure history for a configuration of 6 channels ( $1 \times 1 \text{ mm}^2$ ) in parallel (Kandlikar 2002).

The large negative spikes in the pressure drop indicate that substantial flow oscillations occur in the system. Kandlikar (2002) suggests that the oscillations and flow reversals induce temperature instabilities as well.

Kandlikar (2002) notes that for all micro-channels in multi channel configuration the heat transfer coefficient decreased with increasing heat fluxes. This observation corresponds to the unstable burnout critical heat flux reduction found in forced convection subcooled boiling systems. Bergles *et al.* (2003) shows that a critical heat flux reduction of approximately 30% is invoked by the unstable boiling process, see Figure 5.4.

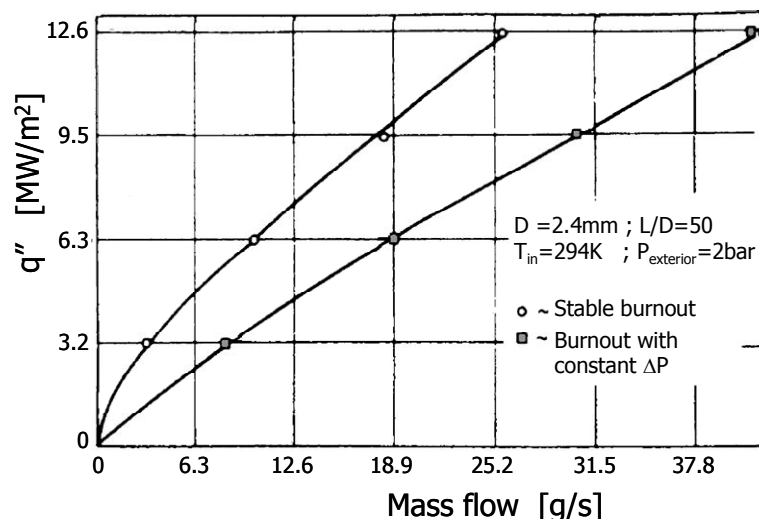


Figure 5.4 – Critical heat flux reduction in case of stable and unstable flow boiling for water, after Bergles *et al.* (2003).

Zhang *et al.* (2005) performed boiling experiments in a single micro channel ( $D_h = 27\text{-}171 \mu\text{m}$ ) with a constant flow. Although it is believed that a forced flow feed does not allow flow instabilities, rather than a constant pressure, some rapid temperature fluctuations are found. In the experiment the temperatures are measured by the change in electrical resistance. After a detailed study, the high

frequency ( $>1$  Hz) signals are considered to be induced by transient pressure components rather than true temperature signals. Zhang *et al.* (2005) observe no bubble nucleation period for channels smaller than  $50\ \mu\text{m}$  diameter. Instead, a process called “eruption boiling” emerges. Possibly, this apparent lack of a nucleation period may be explained by the low frame rate ( $\sim 30$  Hz) of the camera, which could not capture the nucleation process. The smaller the channel, the faster a nucleated spherical bubble obtains the size of the channel followed by the explosive bubble growth. Their nucleate boiling ( $D_h > 100\ \mu\text{m}$ ) and eruption boiling results ( $D_h < 50\ \mu\text{m}$ ) are both supported by the nucleation site hypothesis of Hsu’s model (Hsu 1962). Zhang *et al.* (2005) can not verify in their experiments the “evaporating space” model and “fictitious boiling” concept suggested by Peng (1998). These boiling mechanisms for micro-channels suggested by Peng (1998) assume that nucleation of vapour bubble does not occur and the phase transition is accomplished by other means, such as a sort of overall flashing of the liquid.

### 5.1.2 CONFINED BUBBLE BEHAVIOUR

The dominance of slug flow in small-diameter channels is believed to be one of the major reasons for instabilities to occur. Therefore, this flow pattern and its features in capillaries will be discussed into more detail.

Kreutzer (2005) gives a comprehensive overview on the flow around a slug bubble, its film thickness and the pressure drop. For adiabatic flow, the vapour bubble is not attached to the channel wall. Depending on the dimensionless velocity of the bubble (capillary number:  $Ca = \mu u / \sigma$  i.e. scaling by the viscosity,  $\mu$ , and the surface tension,  $\sigma$ ) either a complete bypass flow occurs ( $Ca > 0.7$ ), or a recirculation vortex with a ring of stagnation points on the vapour bubble is present ( $Ca < 0.7$ ). In case of a complete bypass only a single stagnation point is present, while the recirculation vortex forms a ring a ring of stagnation points on the preceding bubble. The recirculation vortex is most commonly found in small-diameter channels.

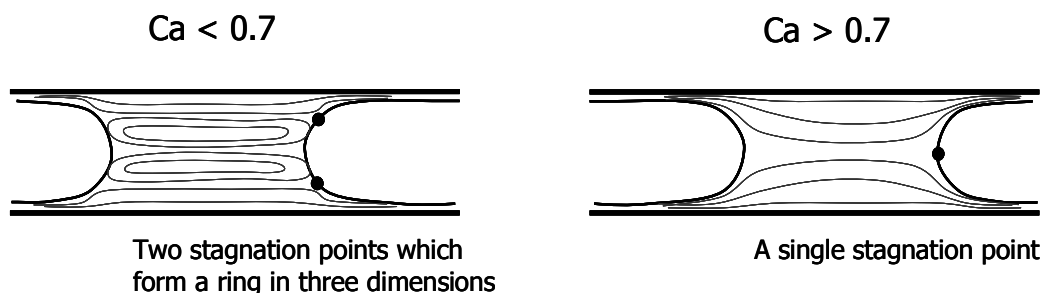


Figure 5.5 – The streamlines within a slug flow for two conditions: recirculation vortex ( $Ca < 0.7$ ) and complete fluid by pass ( $Ca > 0.7$ ).

By means of a lubrication analysis for the transitional region between the spherical bubble cap and the flat film a relation for the film thickness,  $\delta$ , can be derived (Bretherton 1961). Using a scaling analysis results in the classical scaling rule  $\delta/D_h \sim Ca^{2/3}$ , while a thorough derivation of Bretherton’s result yields:

$$\frac{\delta}{D_h} = 0.66Ca^{2/3} \quad (5.1)$$

Equation (5.1) only holds for capillary numbers between  $10^{-4} < Ca < 10^{-2}$ .

The Bretherton relation predicts thick film thicknesses for large capillary numbers. This is not observed in measurements by Taylor (1961) and Bretherton (1961). The film thickness tends to a maximum relative thickness of  $\delta/D_h = 0.2$ . To extend Equation (5.1) to higher capillary numbers, Ausillous and Qu ere (2000) propose the following correlation:

$$\frac{\delta}{D_h} = \frac{0.66Ca^{2/3}}{(1 + 3.33Ca^{2/3})} \quad (5.2)$$

Measurements show that for very small capillary numbers ( $Ca < 10^{-5}$ ) the relative film thickness remains more or less at a threshold value:  $\delta/D_h \sim 10^{-4}$  in round capillaries. In square capillaries the film thickness remains constant at about  $\delta/D_h \sim 10^{-2}$ , for capillary numbers below  $Ca < 10^{-2}$ , see Figure 5.6.

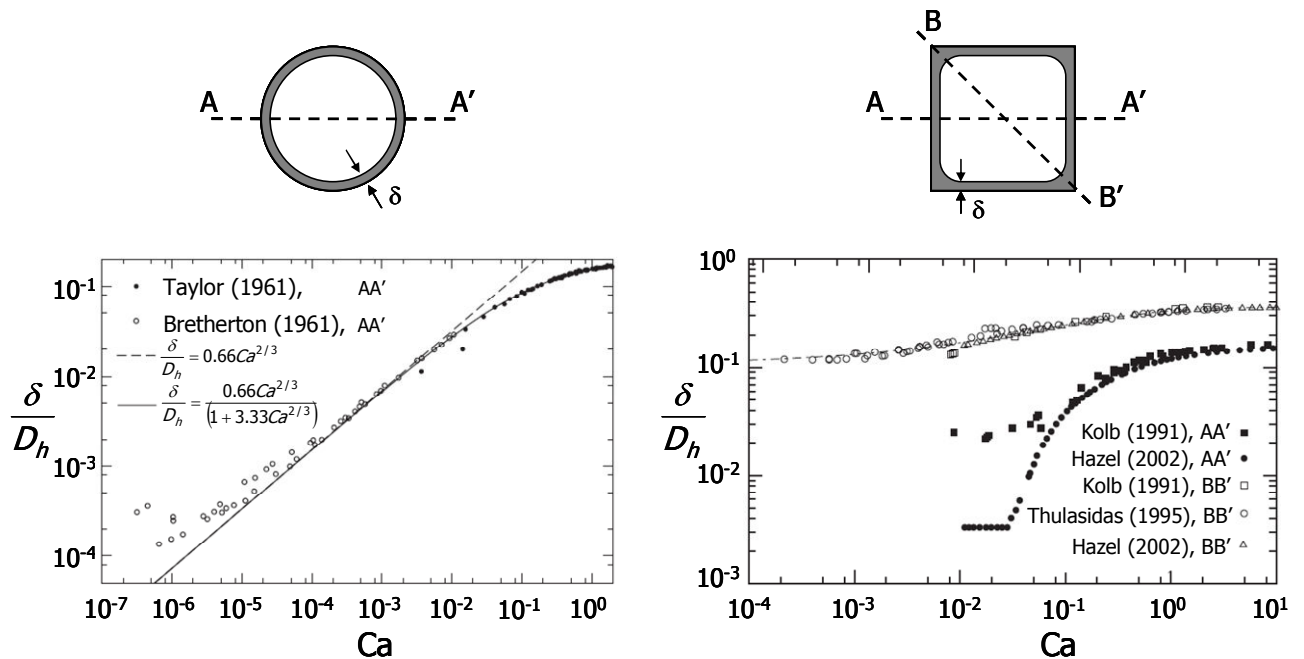


Figure 5.6 – The film thickness,  $\delta$ , relative to the hydraulic diameter,  $D_h$ , as a function of the capillary number,  $Ca$ . Left: measurements and correlation for a round capillary; Right: Measurements (Kolb and Cerro 1991, Thulasidas 1995) and numerical simulations (Hazel and Heil 2002) for a square capillary, after Kreutzer et al. (2005).

The pressure drop in a slug flow is usually attributed to three phenomena, each with its separate contribution. The first contribution is due to the wall friction of the liquid slugs. In micro-channels this term is purely viscous. The second contribution is due to gravity and may be neglected in micro-channels due to the small geometrical sizes. The last contribution is due to the liquid-vapour interface and is thus

proportional to the number of bubbles per unit length. The corresponding Laplace pressure terms can be estimated from lubrication theory. Bretherton relates this pressure term to the film thickness and the capillary number:

$$\Delta P_{Laplace} = 7.16 \cdot \frac{\sigma}{D_h} \cdot (3Ca)^{2/3} \quad (5.3)$$

The expression (5.3) for the pressure drop agrees nicely with experimental data for low capillary numbers. The lubrication theory by Bretherton does not include secondary effects such as Marangoni effects, inertial effects or gravitational effects.

In pressure drop relations for slug flow no pressure drops are assumed along the cylindrical part of the slug bubble. This "no-shear" assumption is justified, since the vapour bubble is not attached to the wall and moves through the liquid. The shear stress is induced by the viscosity of the vapour which is negligible compared to that of the liquid.

### 5.1.3 CONFINED BUBBLE GROWTH

The rapid expansion of the vapour bubble during flow boiling in small-diameter channels is believed to induce flow instabilities. Within several investigations various authors have modelled this process.

Mukherjee and Kandlikar (2005) performed a numerical study characterising the confined bubble growth. No pressure drop, and therefore no supply flow, is assumed over the boiling micro-channel ( $D_h=200 \mu\text{m}$ , channel length=800  $\mu\text{m}$ ). By introducing an inlet restriction in the CFD model, the vapour bubble shows only an explosive growth in the downstream direction.

A one dimensional model along the channel axis on the heat transfer and evaporation rate is suggested by Thome (2004a, b). This model considers three stages (liquid plug, annular film around vapour bubble, and dry-out) for which steady-state correlations are used at all positions. For the regions with a liquid phase and a vapour phase only, regular heat transfer coefficients are used. The evaporation of the liquid film is driven by a wall heat flux, transferred across the liquid film by conduction, implying a fully-developed linear temperature profile across the film. This model does not take into account the pressure fluctuations nor the volume increase of the vapour bubble by the evaporating film.

Kenning *et al.* (2006) performed experiments on explosive bubble growth in a small-diameter tube ( $D_h=0.8 \text{ mm}$  and  $D_h=0.48 \text{ mm}$ ). The round smooth borosilicate glass tube is open at the top side, while at the closed bottom a pressure sensor is implemented. The water was first superheated ( $\Delta T=1.6 \text{ K}$ ,  $2.2 \text{ K}$  and  $3.7 \text{ K}$ ) equal to the wall superheat. Next, bubble growth was triggered by a hot wire to control the start of the experiment. The bubble length is observed with a high-speed camera (200 fps or 500 fps).

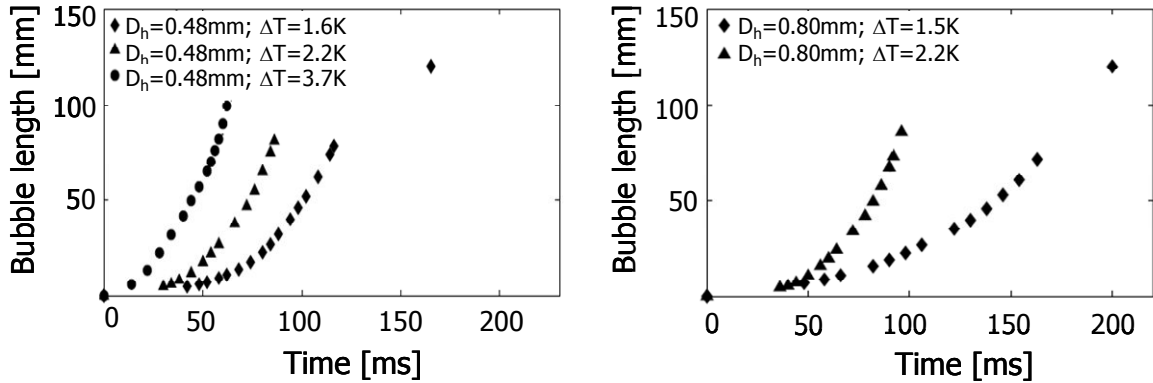


Figure 5.7 – Results for bubble length measurements during explosive bubble growth; Left: 0.48mm diameter tube and three liquid (and wall) superheats; Right: 0.80mm diameter tube and two liquid (and wall) superheats; After Kenning (2006).

Figure 5.7 shows the results for the bubble length for the five measurements. Due to the complexity of the measurement technique (which is sensitive to premature and uncontrolled bubble nucleation) it was not possible to investigate reproducibility.

The proposed bubble growth modelling consists of two parts: spherical bubble growth and confined growth. The spherical bubble growth model is similar to the model of Plesset and Zwick (1954), see section 2.2.2. The confined bubble growth model is based on the following four assumptions.

1. The vapour inside the bubble is at saturation temperature;
2. The film thickness is constant and the same at all positions along the bubble;
3. The liquid column shear stress is calculated by the expression for fully developed laminar flow;
4. The evaporative heat flux is estimated using the one-dimensional transient heat conduction. For reasons of simplicity, the liquid film and the tube wall are assumed to have the same thermal properties for the calculation of the penetration depth.

Kenning *et al.* (2006) use energy, momentum and mass conservation to derive a set of third-order differential equations for the bubble length. No explicit correlation is given between the bubble length and the superheat, the channel diameter or the film thickness. Optimisation of various parameters allowed the bubble length simulations to agree with the measurements, see Figure 5.8.

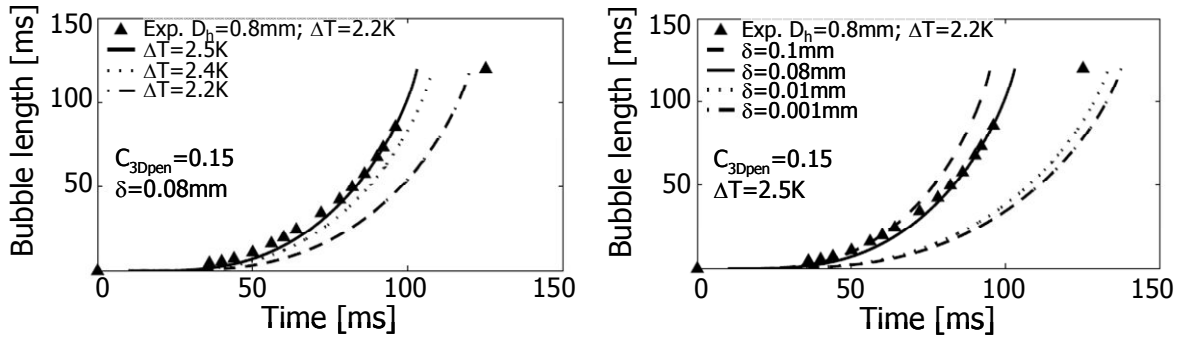


Figure 5.8 – Typical modelling results and sensitivity study for 0.8mm tube diameter and wall superheat 2.2 K. Optimal parameters settings for this case are: Three dimensional spherical heat penetration coefficient,  $C_{3Dpen} = 0.15$ ; Film thickness,  $\delta = 0.08$  mm; Superheat (wall+liquid),  $\Delta T = 2.5$  K. After Kenning *et al.* (2006).

In order to obtain agreement between the bubble length resulting from the model and the measurements, the system superheat in the model has to have an excess of 0.3 K. This is the maximum allowed offset considering the temperature margin of uncertainty in the measurements. Next, in the model the relative film thickness,  $\delta/D_h$ , is set to a fixed value of about 0.1 in order to obtain agreement with their measurements. Although this implies a rather thick film (based on equation (5.2) the relative thickness would be 5 times thinner), this assumed thickness lies within the range of measured film thicknesses in (adiabatic) slug flow through capillaries, see Figure 5.6. The correction factor for the three dimensional heat penetration,  $C_{3Dpen}$ , has to be set to 0.15, while compared to literature this value is expected between 1 – 2, see section 2.2.2.

## 5.2 Elongated vapour bubble behaviour analysis

The elongated slug bubbles are identified as being one of the main reasons for instabilities to occur. In order to get insight to the dominant parameters we performed analyses on the slug bubble blockage and departure and on the growing behaviour of the slug bubble in case of some simplified situations.

### 5.2.1 SINGLE SLUG BUBBLE DETACHMENT MODELLING

To gain insight in the blockage and detachment behaviour of a slug bubble, a scaling analysis is performed considering the flow dynamics in a well-defined situation. Therefore only a single micro channel containing a single slug bubble fixed at one location is considered. Also, the liquid flow rate through the channel is assumed to be constant regardless of the slug bubble size. This situation will be created in the experiment described in section 5.3.1.

Note that in case of a multiple micro-channel heat exchanger the liquid flow can choose another path around the blocked channel. This will therefore minimise the liquid flow through the channel containing the slug bubble. In the next section (5.2.2) this multiple channel situation is discussed in analogy with the scaling analysis presented below of the single micro-channel boiling experiment.

To estimate whether the fixed bubble will detach, a momentum balance is formed over a control volume around the vapour bubble.

$$F_{hyd} = F_{attach} \quad (5.4)$$

The hydrodynamic forces,  $F_{hyd}$ , try to detach the bubble, while the slowly growing vapour bubble is attached to the single heated spot,  $F_{attach}$ , see Figure 5.14.

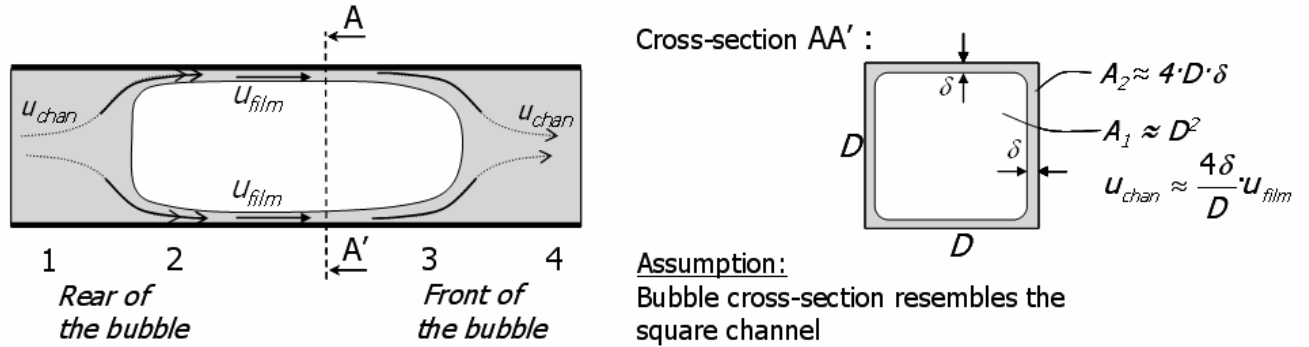


Figure 5.9 – Flow model channel blockage by slug bubble. Left: side view; Right: cross-section view.  $u_{chan}$  is the average undisturbed liquid velocity;  $u_{film}$  is the average liquid velocity in the thin film layer;  $D$  is the channel diameter;  $\delta$  is the liquid film thickness.

For reasons of simplicity no thermal effects like condensation and evaporation will be taken into account. The effects invoked by surface tension gradients (such as Marangoni effects) are neglected as well, since they are only a correction on the Laplace pressure terms at the rear and front of the bubble (see Kreutzer 2003). The bubble cross-section will resemble the square channel for small capillary numbers ( $Ca < 0.04$ ), Kreutzer (2005). Which is the case for our single channel experiment. The bubble is assumed to be a rigid body with no shear at its interface. The total pressure drop  $\Delta P$  over the stagnant bubble is given by

$$\Delta P = \Delta P_{12} + \Delta P_{film} + \Delta P_{34} \quad (5.5)$$

where  $\Delta P_{12}$  and  $\Delta P_{34}$  are the pressure variations respectively at the rear and front of the bubble, and  $\Delta P_{film}$  is the pressure drop in the liquid layer between the vapour bubble and the channel wall, see Figure 5.9.

The flow characteristics in the experiment are slightly different than the standard slug flow. Although the capillary number is very low, no stagnation ring (and thus no recirculation zone) is present. In our experiments all liquid has to pass along the slug bubble (complete fluid by-pass with a single stagnation point) and the bubble itself is stagnant instead of moving through a liquid. Therefore, the standard low capillary number pressure drop relations found in literature do not apply (Kreutzer *et al.* 2005). Instead, we assume the pressure drop over the bubble to be equal to the pressure drop in the thin film of liquid with thickness  $\delta$  which is given by (Incropera *et al.* 2002):

$$\Delta P_{film} = \frac{96}{\text{Re}_{film}} \cdot \frac{L}{D_h} \cdot \frac{1}{2} \rho u_{film}^2 \left( = \frac{96 \mu_{liq} L u_{film}}{32 \delta^2} \right) = \frac{3 \mu_{liq} L_{bub} u_{film}}{\delta^2} \quad (5.6)$$

where  $\text{Re}_{film}$  is the Reynolds number given by  $\text{Re}_{film} = \frac{\rho u_{film} D_h}{\mu}$  and the hydraulic diameter of the film,  $D_h = 4\delta$  (see Figure 5.9).

When the bubble is spherical  $\Delta P \sim \Delta P_{12} + \Delta P_{34}$ , and the observation that these short bubbles do not detach implies that the forces on the rear and front cups of the slug bubble are not sufficient to overcome the attachment force of the bubble. Next, we show in more detail that the pressure drop related to the liquid acceleration and deceleration is (much) smaller than the pressure drop related to the liquid layer ( $\Delta P_{12} + \Delta P_{34}$ )  $<$   $\Delta P_{film}$ .

For an unconfined spherical gas bubble at low Reynolds number the drag force coefficient, which is given by the shape drag only, is given by  $16 \cdot \text{Re}^{-1}$ . We assume that the net drag force of the rear and front caps is of a similar form, i.e.  $C \cdot \text{Re}^{-1}$ . The ratio of inertial forces over viscous forces in these regions is given by  $\text{Re} \cdot \delta / D$ , where  $\delta$  is the film thickness and  $D$  the channel height. In our experiment described in section 5.3.1,  $\text{Re} \sim 1$  and  $\delta / D \sim 1/50$ , so that we are in the lubrication regime (i.e. viscous flow). For a spherical particle in a confined flow (or channel flow), the drag force also scales as  $C \cdot \text{Re}^{-1}$ , although  $C$  is of the order  $10^3$ - $10^4$  when the particle diameter approaches the channel dimensions (Happel and Brenner, 1983). However, we demonstrate that for growing bubbles  $\Delta P_{film}$  dominates, i.e.  $\Delta P \sim \Delta P_{film}$ , and determines the bubble detachment.

We therefore assume that:

$$(\Delta P_{12} + \Delta P_{34}) \sim \frac{C}{\text{Re}_{chan}} \cdot \frac{1}{2} \rho u_{chan}^2 \quad (5.7)$$

where  $\text{Re}_{chan} = \frac{\rho u_{chan} D}{\mu}$  and from Figure 5.9 it follows that  $u_{chan} \cdot D^2 = u_{film} \cdot 4D\delta$ .

$\Delta P_{film}$  will be dominant when  $\Delta P_{film} \gg (\Delta P_{12} + \Delta P_{34})$ . Using equation (5.6) and equation (5.7) with its substitutions we obtain the following relation:

$$\frac{3 \mu_{liq} L_{bub} u_{film}}{\delta^2} \gg \frac{C \mu_{liq}}{\rho \left( \frac{4 u_{film} \delta}{D} \right) D} \cdot \frac{1}{2} \rho \left( \frac{4 u_{film} \delta}{D} \right)^2 \Rightarrow \frac{L_{bub}}{D} \gg C_{tot} \left( \frac{\delta}{D} \right)^3 \quad (5.8)$$

All constants are absorbed in  $C_{tot}$  ( $C_{tot} = 2/3 \cdot C$ ). For  $\delta / D \sim 1/50$  and  $C_{tot} \sim 10^3$ - $10^4$ , the assumption  $\Delta P \sim \Delta P_{film}$  is generally satisfied.

The pressure drop is investigated by performing CFD calculations (FLUENT 6.3) modelling a blocking vapour bubble in a square channel. Again the vapour bubble is

assumed to be a rigid body with no shear at its liquid-vapour interface. The average relative thickness of the liquid film,  $\delta/D$ , is chosen to be 2.5%.

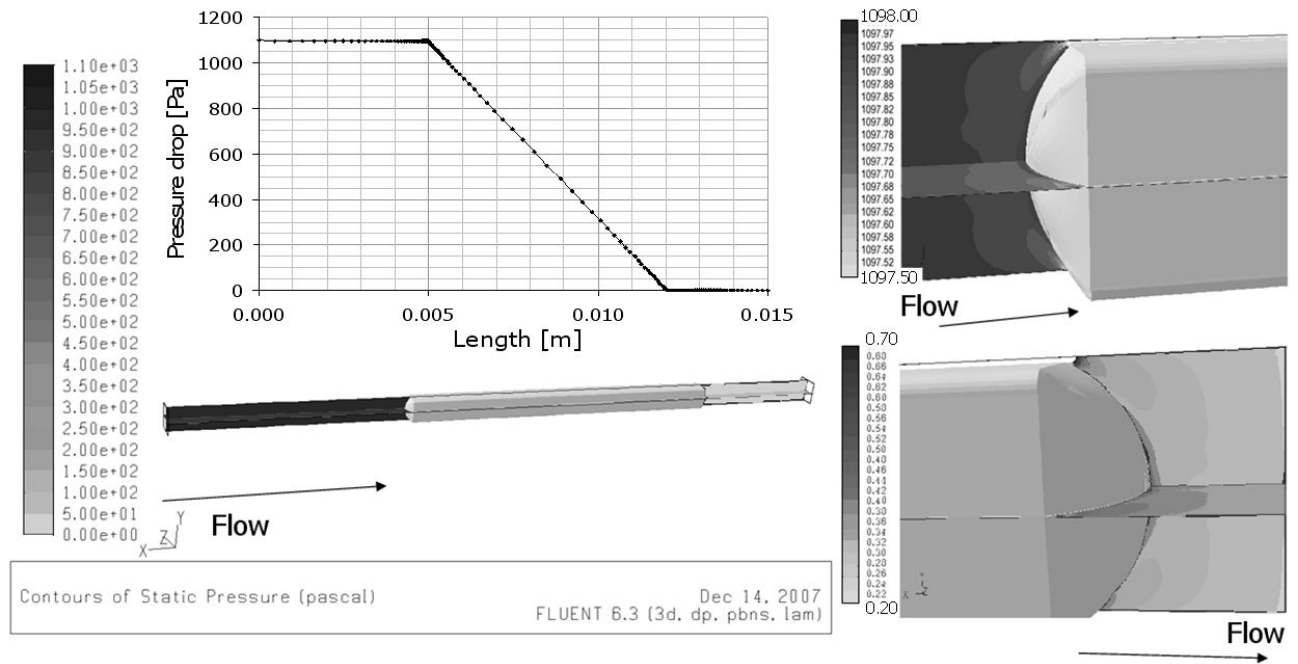


Figure 5.10 – Pressure distribution over a blocking vapour bubble.  $\delta/D=2\%$ ;  $L_{Bubble}=10 D$ ; Flow =  $15 \mu\text{l}/\text{min}$ ; Left: Total pressure drop ( $\sim 1.1 \cdot 10^3 \text{ Pa}$ ); Top right: Rear of the bubble pressure drop ( $\Delta P_{12} \sim 0.5 \text{ Pa}$ ); Bottom right: Front of the bubble pressure drop ( $\Delta P_{34} \sim 0.5 \text{ Pa}$ ).

The bubble is coloured light grey to indicate its position. The left hand figure shows that the main pressure drop is determined by the liquid film which has to be squeezed between the vapour bubble and the channel wall. The two figures on the right hand side show the rear (top figure) and the front of the bubble (bottom figure). For reasons of clarity only the relevant pressure ranges for the corresponding regions are plotted. From these calculations it may be concluded that the pressure drop over the bubble caps,  $\Delta P_{12}$  and  $\Delta P_{34}$ , is indeed negligible with respect to the pressure drop in the film.

A vapour bubble has no exact square shape. At the corners of the bubble the liquid film is somewhat thicker due to the limited curvature of the bubble. Our CFD calculations show that the maximum liquid velocity is about 3 times higher at these corners than the maximum velocity in the planar liquid film. However, this velocity maximum at the corners is rather localised, which reduces its effect on the mass flow distribution. The corner area corresponds roughly to 3% of the total flow through area around the bubble, while 5% of the total flow is passing through this area.

The hydrodynamic force detaching the vapour bubble is therefore given by:

$$F_{hyd} \approx \frac{3}{4} \mu_{liq} \left( \frac{D}{\delta} \right)^3 \cdot L_{bub} \cdot u_{chan} \quad (5.9)$$

Using equation (5.9) to calculate the pressure drop over the bubble as modelled in our CFD simulation yields  $\sim 1.35 \cdot 10^3$  Pa. This is in reasonable agreement with the pressure drop given by the CFD calculation (i.e.  $\sim 1.1 \cdot 10^3$  Pa).

The vapour bubble grows from the single heated spot, see Figure 5.14. The attaching force is estimated by the surface tension of the slug bubble and its attachment length, which is assumed to be the perimeter of the heated spot.

$$F_{attach} \sim \sigma \cdot L_{hotspot\_perimeter} \quad (5.10)$$

Next, it may be assumed that detachment is accomplished if the detaching forces exceed the attaching forces. This yields into the following criterion for the bubble length on detachment:

$$L_{bubble\_detachment} \sim \left( \frac{\sigma \cdot L_{hotspot\_perimeter}}{\frac{3}{4} \mu_{liq} \left( \frac{D}{\delta} \right)^3} \right) \cdot \frac{1}{u_{chan}} \quad (5.11)$$

For capillary numbers smaller than  $1 \cdot 10^{-3}$  it is reported in the literature (e.g. Kolb and Cerro 1991; Kreutzer 2003) that there is an independence of the film thickness of flow velocity. Film thicknesses relative to the square channel diameter are given between 2.5% (observed visually by Kolb and Cerro 1991) and 0.5% (calculated numerically by Hazel and Heil 2002). This means that due to the independent relative film thickness the bubble length and the water mass flow (velocity) are inversely proportional.

$$L_{bubble\_detachment} = \frac{\text{Constant}}{u_{Chan}} \quad (5.12)$$

## 5.2.2 DISCUSSION ON MULTIPLE CHANNEL FLOW

In practice a heat exchanging device will contain multiple micro channels and thus the liquid flow can choose another path in case of a blocking slug bubble. Therefore the liquid flow through the channel containing the stagnant slug bubble will be minimal. Due to the minimal flow, the pressures at the rear and the front of the bubble are mainly determined by external conditions. The pressure at the rear side of the slug bubble will approach the upstream pressure in the divider manifold,  $P_{manifold}$ , since no flow is present. Likewise the pressure at the front side of the bubble will approach the downstream pressure,  $P_{end}$ , if no bubble growth is

assumed. This leads to a hydrodynamic detachment force,  $F_{hyd}$  of the liquid acting on the stagnant, non-growing vapour bubble given by

$$F_{hyd} = D^2 (P_{manifold} - P_{end}) \quad (5.13)$$

A small amount of additional liquid evaporating into the slug bubble results in a large volume increase of the vapour causing the bubble to expand. In case of an expanding bubble, the pressure at the front of the bubble (i.e. the downstream pressure) is raised by an additional friction force induced by the velocity of the bubble front,  $u_{bf}$ , see Equation (5.14), and the increase of momentum of the liquid in front of the bubble, given by Equation (5.15):

$$\Delta P_{liquid\_velocity} = f_{fric} \cdot \frac{L_{liq}}{D} \cdot \frac{1}{2} \rho u_{bf}^2 \quad (5.14)$$

$$\Delta P_{liquid\_acceleration} = L_{liq} \rho_{liq} \cdot \frac{du_{bf}}{dt} \quad (5.15)$$

where  $f_{fric}$  is the flow friction factor ( $f_{fric} = 57/Re$  for stationary flow in rectangular channels; Incropera *et al.* 2002) and  $L_{liq}$  is the channel length downstream of the vapour bubble.

This implies that the hydrodynamic force acting on the bubble is dependent on the bubble growth velocity:

$$F_{hyd} = D^2 \left[ P_{manifold} - \left( P_{end} + \frac{57 \mu_{liq} L_{liq} u_{bf}}{2D^2} + L_{end} \rho_{liq} \cdot \frac{du_{bf}}{dt} \right) \right] \quad (5.16)$$

Under normal conditions the pressure in the divider manifold exceeds the pressure at the outlet, yielding a positive hydrodynamic force pushing the bubble downstream. However, if the bubble expands, the additional pressure may result in a negative hydrodynamic force. This causes the bubble not only to expand and move in the downstream direction, but in the upstream direction as well. Upstream motion of the vapour slug bubble is believed to invoke the major flow instabilities. Therefore, this upstream movement should be prevented for stable operation of the multi-channel evaporator

To predict the sign of the hydrodynamic force from Equation (5.16), it is important to know the positions of the front and rear bubble caps in time. Our analytical model on the explosive bubble growth of an elongated bubble during flow boiling is derived in section 5.2.3

### 5.2.3 EXPLOSIVE BUBBLE GROWTH MODELLING

The explosive bubble growth model is derived for an elongated vapour bubble blocking the channel. Note that this choice excludes the period of spherical bubble growth from nucleation to channel-confined bubble expansion. The vapour inside the growing bubble is assumed to be homogeneous at a temperature equal to the fluid saturation temperature ( $T_{sat}=373K$ ). Furthermore, the detailed evaporation and condensation processes taking place in the vapour bubble are not included in the model. The evaporative heat flux,  $q''$ , is estimated similar to the heat transfer model proposed by Dupont *et al.* (2004). I.e. the heat flux into the liquid layer is estimated by assuming a linear temperature profile in the thin liquid layer between the bubble temperature and the fixed wall temperature, see Figure 5.11.

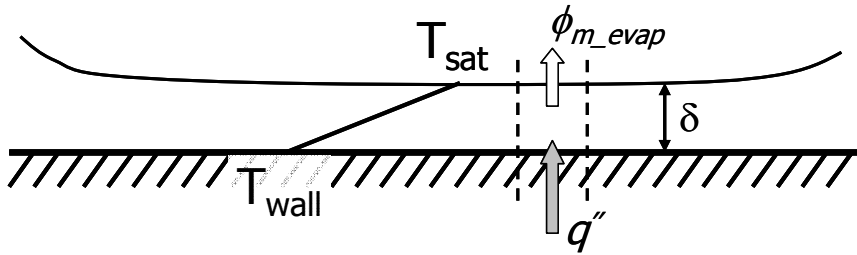


Figure 5.11 – Linear temperature profile assumption over thin liquid layer;  $q''$ = evaporative heat flux,  $\delta$ =film thickness,  $\phi_{m\_evap}$ =evaporation mass flow,  $T_{wall}$ =wall temperature,  $T_{sat}$ =liquid saturation temperature.

$$q'' = -\lambda_{liq} \frac{dT}{dx} = \lambda_{liq} \frac{T_{wall} - T_{sat}}{\delta} \quad (5.17)$$

On assuming that all the heat is used for evaporation, the evaporative mass flow can be estimated as follows:

$$\phi_{m\_evap} = \frac{A_{evap}}{h_{ev}} \frac{\lambda_{liq} (T_{wall} - T_{sat})}{\delta} \quad (5.18)$$

To estimate the film thickness as a function in time, a mass balance is formed over a control volume in a slice of the liquid layer, see Figure 5.11. The incoming and outgoing liquid mass flows are assumed to compensate each other, leaving only the evaporative mass flow as an outgoing mass flow.

$$\frac{dm_{film}}{dt} = \rho_{liq} A_{evap} \frac{d\delta}{dt} = -\phi_{m\_evap} \quad (5.19)$$

The thickness,  $\delta$ , of the liquid layer can be calculated by solving the above differential equation. Hence the film thickness and the evaporation mass flow rate,  $\phi_{m\_evap}$ , in time are given by Equations (5.20) and (5.21):

$$\delta(t) = \sqrt{\delta_0^2 - \frac{2\lambda_{liq}(T_{wall} - T_{sat})}{h_{ev}\rho_{liq}} t} \quad (5.20)$$

$$\phi_{m\_evap}(t) = \frac{A_{evap}\lambda_{liq}(T_{wall} - T_{sat})}{h_{ev}\delta(t)} \quad (5.21)$$

$\delta_0$  is the initial thickness of the liquid layer at time  $t=0$  s.

All vapour causing the elongated bubble to grow originates from the thinning liquid layer,  $\phi_{m\_evap}(t)$ . Using Equations (5.20) and (5.21) we construct a mass balance over the expanding elongated vapour bubble according to Figure 5.12.

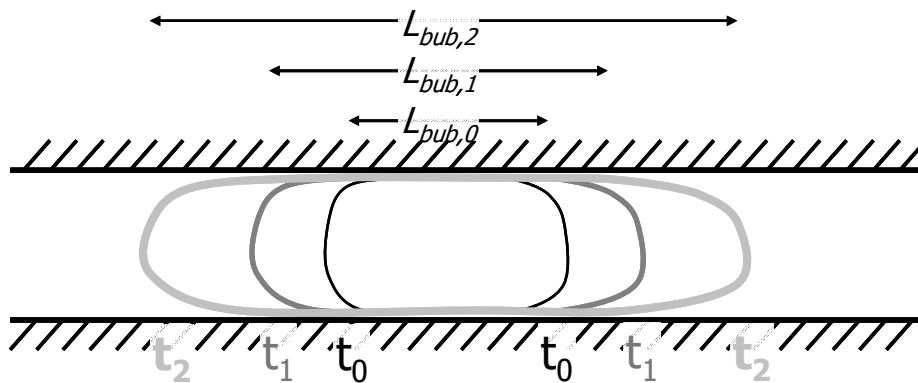


Figure 5.12 – Expanding vapour bubble at various moments in time:  $t_0$ ,  $t_1$ ,  $t_2$ ;  $L_{bub,0}$  initial bubble length,  $L_{bub,1}$  bubble length at time  $t_1$ ,  $L_{bub,2}$  bubble length at time  $t_2$ .

As a first estimate, the expanding evaporation area,  $A_{evap}$ , is assumed to be equal to the elongated vapour bubble length,  $L_{bub}$ , multiplied by its perimeter which is assumed to be equal to the channel perimeter,  $4D$ . Next, it is assumed that the liquid film layer has a constant thickness over the full length of the bubble. All newly created film (i.e. by bubble growth) is of equal thickness as the already existing liquid film. Hence no bubble cap velocity dependency ( $\sim Ca^{2/3}$ ) or time delay is included.

$$\frac{dm_{bub}}{dt} = D^2 \rho_{vap} \frac{dL_{bub}}{dt} = \frac{(L_{bub} \cdot 4D)\lambda_{liq}(T_{wall} - T_{sat})}{h_{ev} \sqrt{\delta_0^2 - \frac{2\lambda_{liq}(T_{wall} - T_{sat})}{h_{ev}\rho_{liq}} \cdot t}} \quad (5.22)$$

Solving the above differential equation results in a relation for the length of the vapour bubble in time as given by Equation (5.23):

$$L_{bub}(t) = L_o \exp \left\{ \frac{4\rho_{liq}\delta_0}{D\rho_{vap}} \left[ 1 - \left( 1 - \frac{2\lambda_{liq}(T_{wall} - T_{sat})}{h_{ev}\rho_{liq}\delta_0^2} t \right)^{\frac{1}{2}} \right] \right\} \quad (5.23)$$

The parameters of equation (5.23) may not be exactly known. For example in our experiment on the explosive bubble growth of water in aluminium channels these are the initial film thickness,  $\delta_0$ , the wall superheat,  $T_{wall} - T_{sat}$ , and the initial bubble length,  $L_0$ . For these three parameters a sensitivity study is performed.

Figure 5.13 shows the bubble growth sensitivity with respect to the initial film thickness,  $\delta_0$ , and the wall superheat,  $T_{wall} - T_{sat}$ .

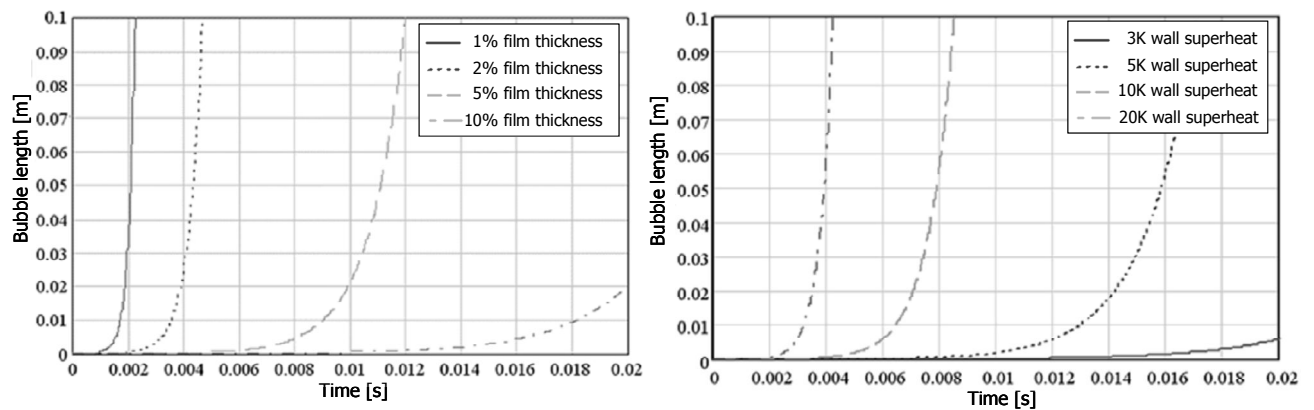


Figure 5.13 – Bubble growth model parameter sensitivity; Left: variation of initial film thickness, range 1% - 10% of channel diameter @  $\Delta T=25K$ . Right: variation of wall superheat, range 3K – 20K @  $\delta_0=0.015D$ .

Within the left graph of Figure 5.13 the film thickness,  $\delta$ , is varied from 1% to 10% of the channel diameter. The right graph shows the bubble length for the wall superheat,  $T_{wall} - T_{sat}$ , at the start of nucleate boiling, 3K, up to the wall superheat near the critical heat flux, 20K. For both parameters this variation is within their full reasonable range. A prominent influence on the explosion time was found for these both parameters.

Finally, the influence of choosing an initial bubble length on the explosion time,  $L_0$ , is found to be less prominent than the influence of the film thickness or the wall superheat. This is understood from the fact that this parameter is not present in the exponent of Equation (5.23), as opposed to the liquid film thickness and the wall superheat.

### 5.3 Experimental

Theoretical analyses on slug bubble behaviour are proposed in the previous chapter. To justify these analyses, which give a better understanding on the pressure instabilities, two types of experiments are conducted. First, the single channel slug

bubble blockage and detachment are investigated by means of the simplified experiment in which the attachment and growth of a single slug bubble are well controlled. Second, the explosive growth is observed in a multiple channel setup by means of a high speed camera.

### 5.3.1 SINGLE SLUG BUBBLE BLOCKAGE SETUP

The slug bubble behaviour is investigated in a  $500 \times 500 \mu\text{m}^2$  glass micro-channel. In order to control the location of the slug bubble formation, heat is supplied to the fluid only at a single location. A  $800 \times 500 \mu\text{m}^2$  copper hotspot is created by a small copper rod (water contact angle  $\sim 40^\circ$ ) placed through the glass (water contact angle  $\sim 50^\circ$ ). The temperature of the hotspot is set at just above the boiling temperature of water. Due to the relatively poor heat conductivity of glass ( $\lambda \sim 0.9 \text{ W/m K}$ ) and the applied low wall superheat the little void (depth  $\sim 50 \mu\text{m}$ ) is the only region where the wall temperature exceeds the boiling temperature. This void determines the attachment region,  $L_{attach}$ , of the fixed slug bubble. The length of this bubble attachment region equals the perimeter of the heater:  $L_{attach} \sim \text{heater perimeter} = 2.6 \text{ mm}$ . In Figure 5.14 the heated copper spot and the  $500 \times 500 \mu\text{m}^2$  glass channel are shown.

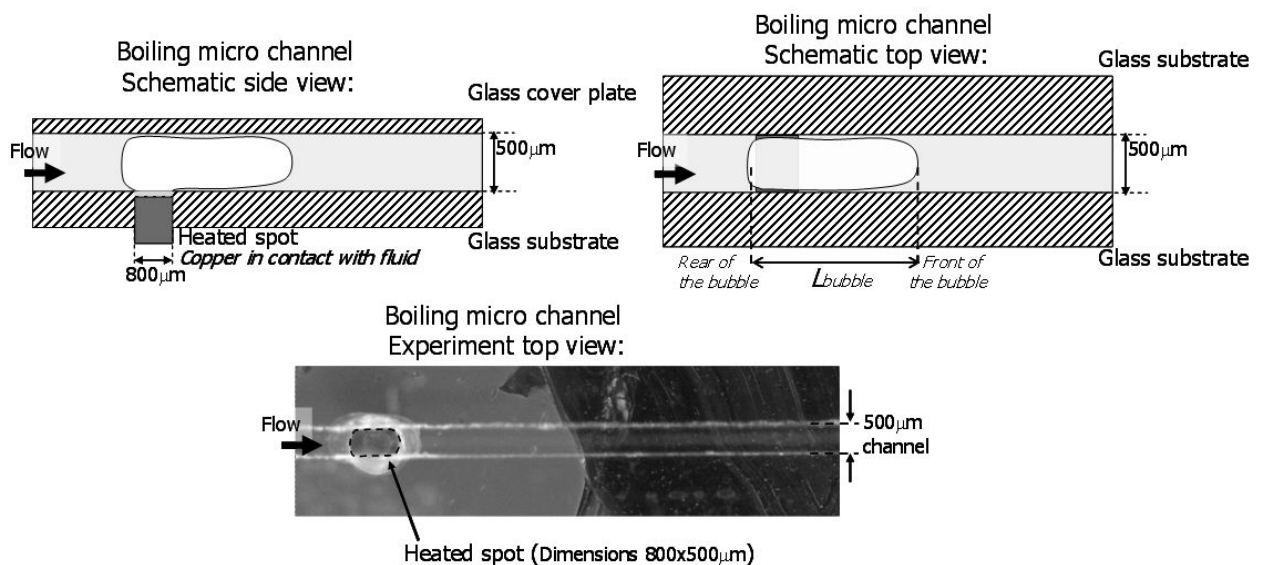


Figure 5.14 – Schematic overview and actual experimental setup of a single slug bubble boiling micro-channel

Except for the little copper rod the complete setup is kept at room temperature ( $T = 293 \text{ K}$ ). Due to the small thermal entry length the water is regarded to be in equilibrium with the wall at all locations. This means that the vapour bubble will grow in a subcooled liquid. A low wall superheat realises a slow and well controlled bubble growth. At a later stage the same experiment is repeated while the complete setup is kept at  $353 \text{ K}$  ( $80^\circ\text{C}$ ). By submerging the complete setup in water of the specified temperature the optical access to the micro-channel is preserved.

The water flow through the channel is set by a syringe pump (KD-Scientific, KDS101). A 1 ml syringe (with an inner diameter of 4.7mm) is used to achieve flow rates  $0.005 \text{ ml/min}$  and  $0.03 \text{ ml/min}$ . This ensures that for the applied flow the step

frequency of the syringe pump is higher than 10 Hz, with a micro-step advance of 0.088  $\mu\text{m}$ . The tubing for the water supply is kept short (<5 cm) and rigid (stainless steel).

The experiment is repeated 5 to 10 times for each individual flow rate. Over these measurements an average bubble detachment length is estimated. No monotonous increase or decrease in the consecutive flow rates is applied to prevent possible hysteresis effects.

### 5.3.2 EXPLOSIVE BUBBLE GROWTH SETUP

The research on explosive slug bubble growth is performed in two parallel 1x1 mm<sup>2</sup> aluminium small-diameter channels covered by a glass plate for optical access. At the bottom of the precision milled aluminium piece an electrical heater is attached, shown in Figure 5.15.

The water flow is set by a syringe pump (Aladdin-1000). A 60 ml syringe (with an inner diameter of 25.4 mm) is used and it is ensured that for the applied flows the step frequency exceeds 10 Hz. The tubing for the water supply is kept short (<5 cm) and rigid (stainless steel). The presence of a second channel allows the provided liquid to chose an alternative path in case of a channel blockage. Therefore, relatively small pressure fluctuations (<1mbar) are expected in the inlet divider manifold. No actual pressure measurements were taken during the experiment.

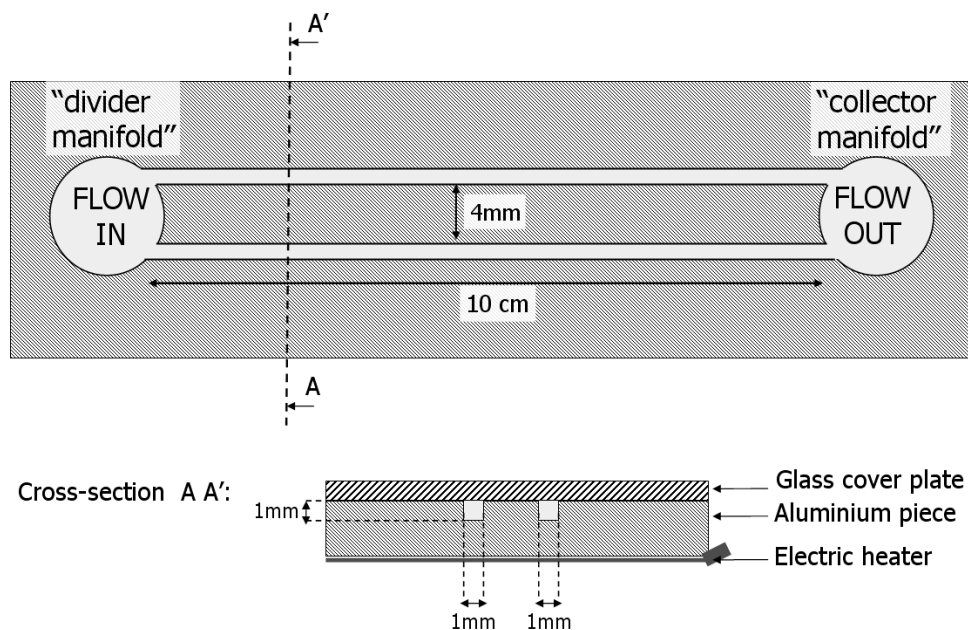


Figure 5.15 – Schematic overview of the multiple small-diameter setup in which the explosive bubble growth is observed.

The heating power input is fixed for each run and the wall temperature of the channels is estimated from a K-type thermocouple placed 3 mm below the channels (0.5 K accuracy). Due to the high thermal conductivity of aluminium ( $\lambda=237 \text{ W/mK}$ ) all three metal walls of the flow boiling channels are expected to participate in the heat transfer. The electrical power input is not recorded and only the most

elementary insulation is applied to the setup, since the (evaporative) heat flux estimation is no aim of this experiment. The incoming water flow is at room temperature,  $T=293$  K.

By means of high-speed camera recordings bubble explosions are observed for a range of water flows (100 ml/hr – 750 ml/hr) and wall superheats (4.2 K – 8.6 K). These high-speed camera visualisations (2000 fps and 3000 fps) of the flow are made to determine the slug bubble length as a function of time. Within the first part of the channel all characteristic features of the bubble growth take place. Only the first 40 mm of the two parallel channels are imaged in order to have enough spatial resolution (1 pixel  $\sim 0.05 \times 0.05$  mm<sup>2</sup>).

## 5.4 Experiment results

### 5.4.1 SINGLE SLUG BUBBLE BLOCKAGE RESULTS

Raw camera images are shown in Figure 5.16. The snapshots show the large bubbles just after their detachment from the heated spot. A clear influence of the amount of water flow on the bubble length for detachment is visible. The low wall superheat of the hotspot causes a slow growth of (small) bubbles on the heater. However, if these small bubbles do not coalesce to one “large” slug bubble they may detach prematurely from the heated surface. These tiny bubbles often get trapped in the corners of the square channel due to the low velocity. The fact that these bubbles remain to exist despite the liquid subcooling, may indicate that the bubbles are mainly filled by the dissolved air.

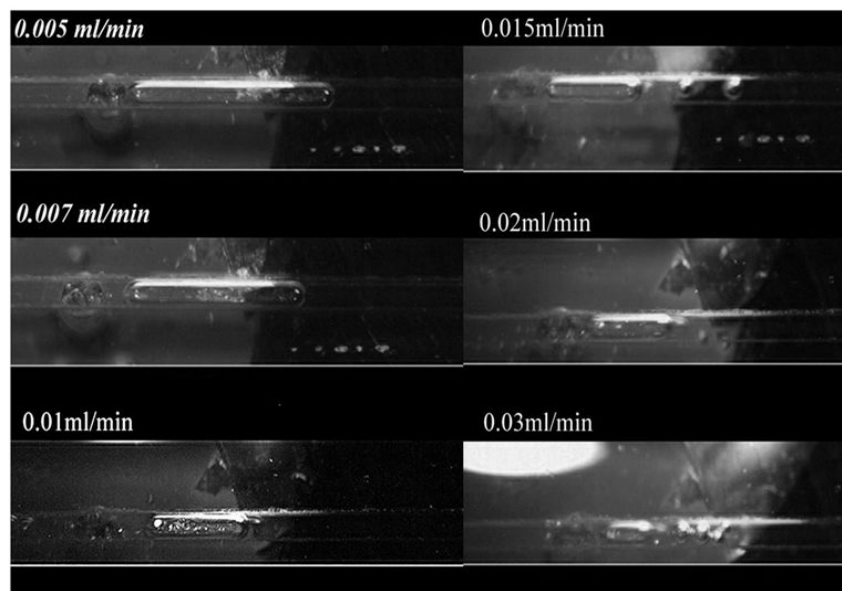


Figure 5.16 – Raw camera images just after the vapour bubble detachment for different flows (setup temperature 293K). Eg: Flow= 0.01 ml/min ( $u_{liq}=0.7$ mm/s) corresponds to capillary number  $Ca = \eta_{liq}u/\sigma = 1 \cdot 10^{-5}$ .

The influence of the water flow on the bubble length at detachment is quantified in more detail in Figure 5.17.

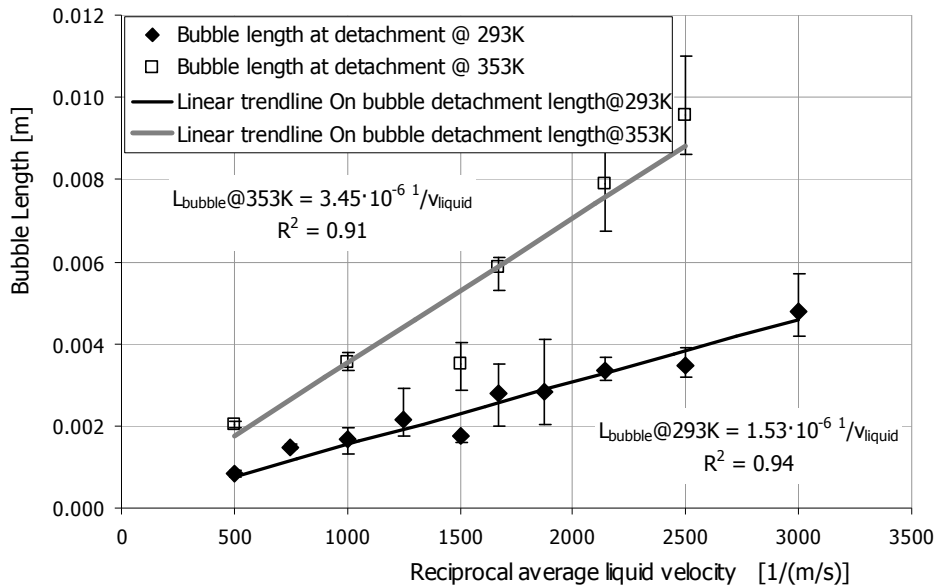


Figure 5.17 – Bubble length at the moment of detachment as a function of the water flow. The solid symbols are the results for a system temperature of 293 K. The open symbols are the results for a system temperature of 353 K. The equations of the least square linear fits through the data points are shown as well.

On plotting the bubble length on detachment versus the reciprocal water flow velocity the data points appear to lie on a straight line for both setup temperatures (293K and 353K). In case the complete setup is kept at room temperature (except for the heated hotspot) the linear slope is  $1.53 \cdot 10^{-6} \text{ m}^2/\text{s}$ . A larger slope value for the least square fit of  $3.45 \cdot 10^{-6} \text{ m}^2/\text{s}$  is found for the case when the complete setup is kept at 353K.

The linear proportionality with respect to the reciprocal average liquid velocity corresponds to equation (5.12) derived in section 5.2.1. The measured proportionality constants between the measured bubble detachment length and reciprocal velocity can be related to relative film thicknesses using the respective physical properties for each measurement situation. For the case when the complete setup is at room temperature (i.e. 293 K)  $D/\delta$  is 54 and for the case the complete setup is kept at 353 K the relative thickness,  $D/\delta$ , is 56. This corresponds to a film thickness of approximately 2% of the total channel diameter, which is in correspondence with the values reported in the literature (Kolb and Cerro 1991).

The outlying data point for both test situations at 1500 s/m (flow 0.01 ml/min) is not understood. A possible interaction between the stepping frequency of the pump and the system is investigated by changing the 1ml syringe ( $D=4.7 \text{ mm}$ ) into a 2.5 ml syringe ( $D=8.6 \text{ mm}$ ). The bubble detachment length results obtained with the 2.5 ml syringe fell within the existing error margin of the other measurements.

#### 5.4.2 EXPLOSIVE BUBBLE GROWTH RESULTS

Bubble explosions are observed for four different wall temperatures (104.2°C, 106.4 °C, 107.6 °C and 108.6 °C) and for four different water flows (100 ml/hr, 200 ml/hr, 300 ml/hr and 750 ml/hr). The slug bubble length is determined in time from high

speed camera recordings, because the explosion time of a vapour bubble is typically in the order of a few milliseconds. Figure 5.18 shows a typical result of these recordings.

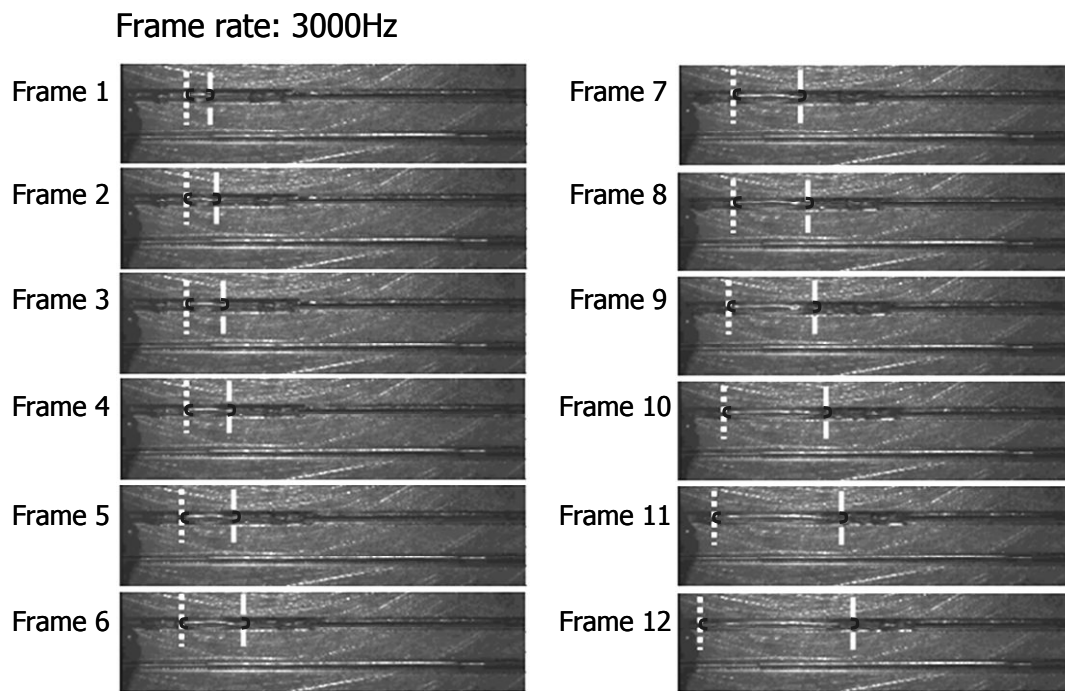


Figure 5.18 – Typical result of explosive bubble growth with flow reversal. The rear and the front ends of the bubble are marked, the flow is from left to right; Wall superheat=4.2K, flow=300ml/hr, time interval between frames= $3.3 \cdot 10^{-4}$  s.

The first frame (Figure 5.18) shows the blocking vapour bubble in the upper channel. The rear end is marked by the narrowly dashed line and the front of the bubble is indicated by the widely dashed line. The high-speed camera flow visualisation indicates that the vapour bubble first expands only in streamwise direction (frame 1 to 4) and the rear of the bubble remains fixed. After a while (frame 5) the rear end of the bubble moves in the upstream direction towards the flow inlet. This vapour bubble expansion behaviour is similar to the behaviour observed by Kandlikar (2002) and Brutin *et al.* (2003).

To quantify the explosive vapour bubble growth, the length of the vapour bubble (i.e. the distance between the two dashed lines) is determined in each frame for all experiments. Typical results for different flow rates and wall temperatures are shown in Figure 5.19. To give an impression of the reproducibility for some test situations multiple growth results are given ( $T_{\text{wall}}=104^{\circ}\text{C}$  and flow=100 ml/hr;  $T_{\text{wall}}=104^{\circ}\text{C}$  and flow=200ml/hr).

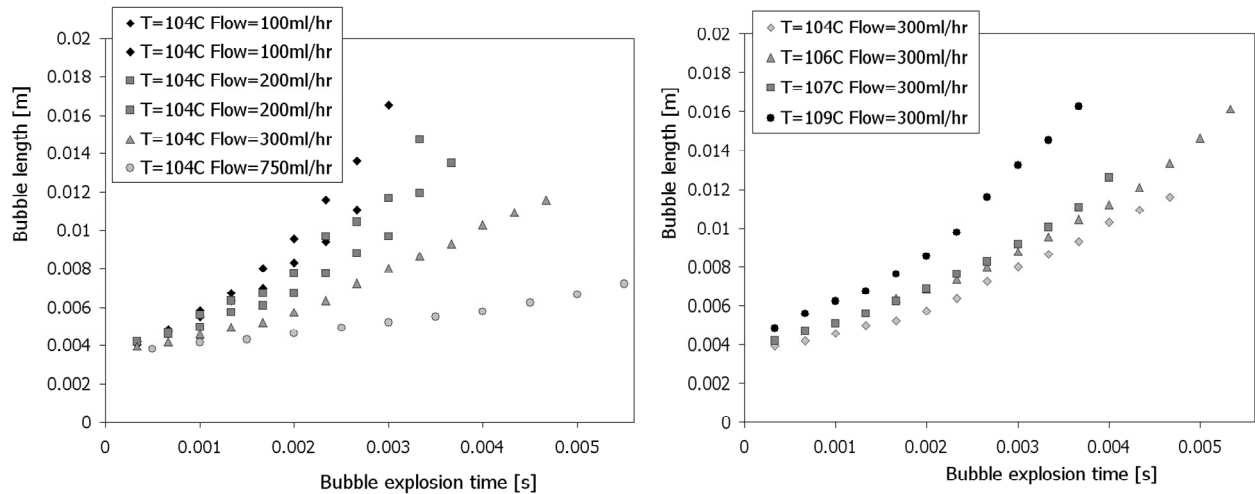


Figure 5.19 – Exploding vapour bubble length as a function of time. Left: bubble growth for various flows; Right: bubble growth for various temperatures.

In order to make comparison at different conditions for each bubble an initial length of 4mm ( $4 \cdot D_h$ ) is chosen as starting point in the graph. At this length the surface area of the cylindrical part of the bubbles is larger than the surface area of the bubble caps. This length is set as the initial bubble length in our explosive bubble growth model as well.

The results in the left hand graph show a decrease in bubble growth rate on increasing the liquid flow supply to both channels. The right hand graph shows an increase on bubble growth rate on increasing the wall superheat.

### 5.4.3 EXPLOSIVE BUBBLE GROWTH MODEL VALIDATION

To test and compare the simplified model where it was assumed that only the cylindrical part of the bubble contributes to the evaporation mass flow, only the measurement data exceeding four channel diameters is taken into account. At this length the surface area of the cylindrical part of the bubbles outweighs the surface area of the bubble caps. This length ( $4 \cdot D_h = 4 \text{ mm}$ ) is set as the initial bubble length,  $L_0$ , in the model.

In the present experiments the glass top of the channel can be regarded as an adiabatic wall, which does not participate in the heat transfer. Therefore, only three participating walls are taken into account, as a consequence the perimeter related to the heat transfer is 3D.

The film thickness is believed to be dependent on the liquid supply flow rate, since only two channels are available. For the present explosive bubble experiments no information on the initial film thickness could be obtained. Therefore, the film thickness in the model is optimised for the different flows at a single wall superheat, see Figure 5.20.

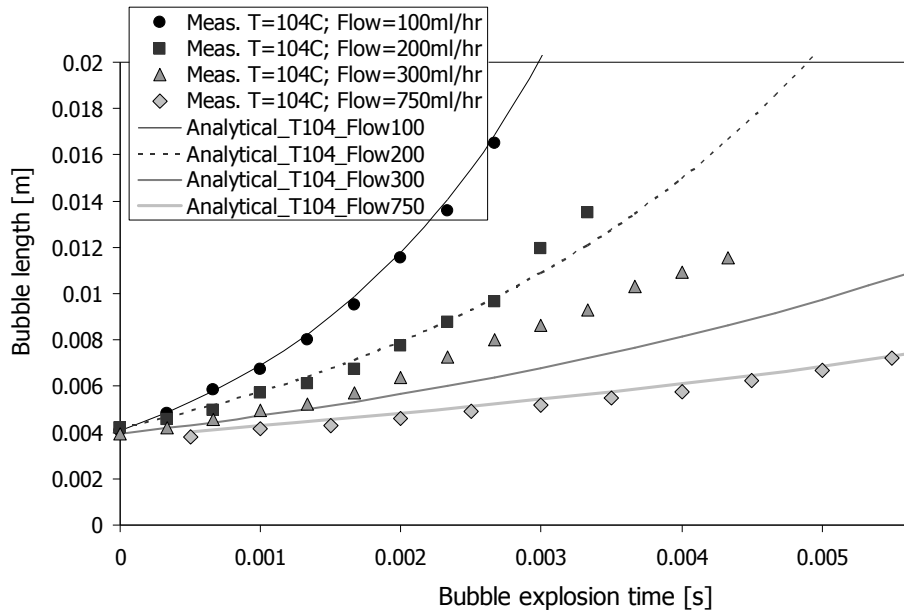


Figure 5.20 – Bubble length calculations with optimised film thickness for each flow; Flow=100 ml/hr ->  $\delta_0=0.012D$ ; Flow=200 ml/hr ->  $\delta_0=0.02D$ ; Flow=300 ml/hr ->  $\delta_0=0.035D$ ; Flow=750 ml/hr ->  $\delta_0=0.055D$ .

Using the film thickness determined above from the model fit for each of the flows, the wall superheat dependency of the model is compared with measurements at two water flows, Figure 5.21.

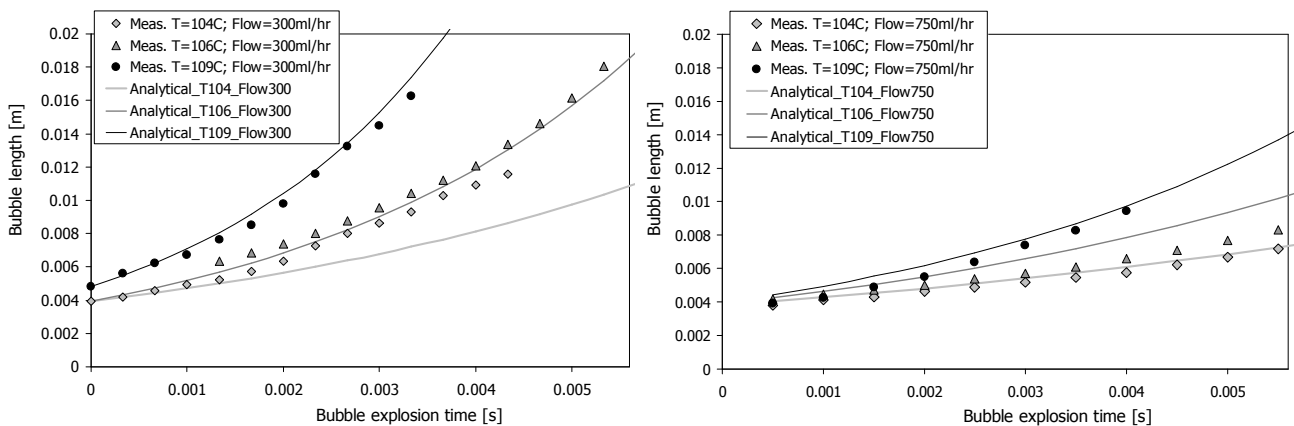


Figure 5.21 – Bubble length calculations vs. measurements for 3 values of the wall superheat. Left: intermediate flow rate (300 ml/hr), right: high flow rate (750 ml/hr).

For both the intermediate flow rate (300 ml/hr) and the high flow rate (750 ml/hr) the predictions of the bubble explosion model are in reasonable agreement with the measurements.

The explosive bubble model is compared to the bubble explosion measurements performed by Kenning *et al.* (2006). Since Kenning has performed his measurements in a round channel the perimeter of the evaporative area in the model should be  $\pi \cdot D$  instead of  $4 \cdot D$  for our experiments. Again, no measurements on the film thickness are available. Therefore the value of the relative film thickness in the model has been optimised for both channels:  $\delta/D=0.15$  in case of 0.48 mm channel and  $\delta/D=0.1$  in case of 0.80 mm channel. Reasonable agreement is found

in most cases. Although our model underestimates the vapour bubble growth in case of the 0.80 mm diameter channel at a superheat of 2.2 K, see Figure 5.22.

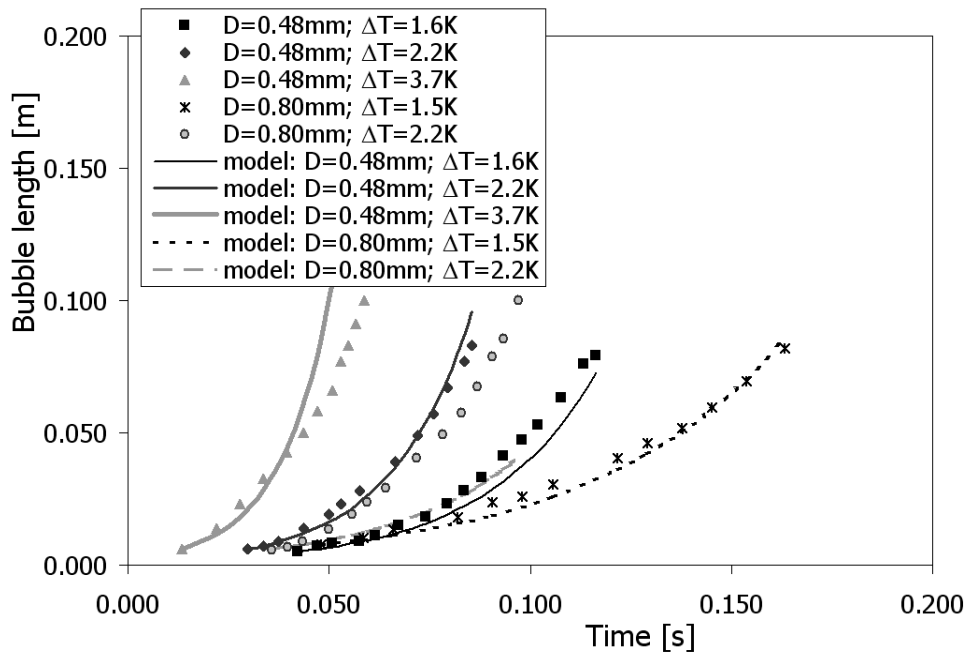


Figure 5.22 – Bubble length calculations for a round channel vs. bubble explosion measurements in a round channel by Kenning (2006). Optimised initial relative film thickness: 15% and 10% in case of 0.48mm and 0.80mm channel diameter respectively;

Our simplified model is solely based on mass balances over the vapour bubble and over the liquid film. Therefore, no other effects such as surface tension, friction and acceleration are taken into account. These effects can be neglected on the basis of a time scale analysis of the energy balance over the expanding vapour bubble.

$$\frac{dE_{bub}}{dt} = E_{in} - E_{out} \quad (5.24)$$

The energy content of the vapour bubble,  $E_{bubr}$ , consists of thermal energy,  $E_{therm}$ , and kinetic energy,  $E_{kin}$ .

$$\begin{aligned} E_{therm} &= m_{bub} c_p T \approx \rho_{vap} \cdot c_{p\_vap} \cdot T_{vap} \cdot (D^2 L_{bub}) \\ E_{kin} &= \frac{1}{2} m_{bub} u_{bub}^2 \approx \frac{1}{2} \rho_{vap} \cdot u_{bub}^2 \cdot (D^2 L_{bub}) \end{aligned} \quad (5.25)$$

The incoming energy,  $E_{inr}$ , is equal to the evaporation heat, which is approximated by the heat transferred over the thin liquid layer.

$$E_{in} \approx A_{ll} \frac{\lambda_{liq} \Delta T}{\delta} = \frac{4D \cdot \lambda_{liq} \cdot \Delta T}{\delta} \cdot L_{bub} \quad (5.26)$$

Not all of the energy entering the bubble is used to increase the energy content of the bubble. The surface enlargement of the bubble requires energy, as well as the motion of the liquid at the rear and the front of the bubble: wall friction and liquid acceleration. Therefore  $E_{out}$  can be approximated by:

$$E_{out} \approx 2 \left[ 4D \cdot \sigma \cdot u_{bf} + f_{fric} \cdot \frac{1}{2} \rho_{liq} u_{bf}^2 \cdot \frac{L_{liq}}{D} + \frac{d}{dt} \left( \frac{1}{2} \rho_{liq} L_{liq} D^2 \cdot u_{bf}^2 \right) \right] \quad (5.27)$$

Since the bubble is expected to expand in two directions (to the front and the rear) all these terms are multiplied by two. In the above equations  $c_{p\_vap}$  is the heat capacity of the vapour,  $T$  is the temperature of the vapour,  $V$  is the volume of the bubble,  $v_{bub}$  is the bubble velocity,  $v_{bf}$  is the velocity of the moving bubble interface and  $L_{liq}$  is the length of the liquid column next to the bubble.

Now we make the following five assumptions:

1. isothermal ( $T=T_{sat}$ ) cylindrical bubble with no velocity
2. no reduction in film thickness (constant evaporation mass flux)
3. the bubble expands equally in two directions,  $u_{bf} = \frac{1}{2} \frac{dL_{bub}}{dt}$
4. rectangular channel, thus the (laminar) friction factor is  $f_{fric} = \frac{57}{Re}$
5. the liquid column next to the bubble,  $L_{liq}$  is independent of the bubble length.

Although each of these assumptions implies a simplification of the actual situation, we have chosen for this approach since it will give us insight on the relative importance of each effect. Using the above assumptions it is possible to rewrite the energy based differential equation and find for each term its time constant,  $\tau$ :

$$\frac{1}{L_{bub}} \left( \frac{dL_{bub}}{dt} \right) = \frac{1}{\tau_1 + \tau_2 + \tau_3 + \tau_4} \quad (5.28)$$

with:

$$\tau_1 = \frac{\rho_{vap} c_{p\_vap} T_{sat} \delta_0}{4 \lambda_{liq} \Delta T} \quad (5.29)$$

$$\tau_2 = \frac{D \sigma}{\lambda_{liq} \Delta T} \quad (5.30)$$

$$\tau_3 = \frac{57 \mu_{liq} L_{liq} L_{bub}}{2 \rho_{liq} \Delta h_{ev} D^2} \quad (5.31)$$

$$\tau_4 = \frac{\rho_{liq} L_{liq} D \delta_0}{8 \lambda_{liq} \Delta T} \left( \frac{d^2 L_{bub}}{dt^2} \right) \quad (5.32)$$

In Equation (5.28)  $\tau_1$  represents the time scale of evaporation,  $\tau_2$  represents the time scale of bubble surface expansion,  $\tau_3$  represents the wall friction time scale, and finally  $\tau_4$  is the liquid acceleration time scale. In case of our experiments (10 cm long 1x1mm channels, boiling liquid water:  $\rho_{vap}=0.6 \text{ kg/m}^3$ ,  $c_{p\_vap}=2 \cdot 10^3 \text{ J/kgK}$ ,  $T_{sat}=373 \text{ K}$ ,  $D=1 \cdot 10^{-3} \text{ m}$ ,  $\delta_0=5 \cdot 10^{-5} \text{ m}$ ,  $\lambda_{liq}=0.6 \text{ W/mK}$ ,  $\Delta T=5 \text{ K}$ ,  $\sigma=0.6 \text{ N/m}$ ,  $\mu_{liq}=3 \cdot 10^{-4} \text{ Pas}$ ,  $L_{liq}=1 \cdot 10^{-1} \text{ m}$ ,  $L_{bub}=1 \cdot 10^{-2} \text{ m}$ ,  $\rho_{liq}=1 \cdot 10^3 \text{ kg/m}^3$ ,  $\Delta h_{ev}=2.6 \cdot 10^6 \text{ J/kg}$ ,  $d^2 L_{bub}/dt^2=2 \cdot 10^3 \text{ m/s}^2$ )  $\tau_1$  is typically in the order of  $10^{-4} \text{ s}$ , while  $\tau_2 = 10^{-6} \text{ s}$ ,  $\tau_3 = 10^{-9} \text{ s}$  and  $\tau_4 = 10^{-5} \text{ s}$ . This implies that  $\tau_1$  is the largest which indicates that the evaporation process is dominant with respect to the surface tension, friction and acceleration terms and therefore justifying the neglect of the surface tension, friction and acceleration terms.

#### 5.4.4 DESIGN RECOMMENDATIONS

These relations above, derived by the simple models, can be used to get a better design of a multiple micro-channel array. Equation (5.16) shows the importance of the bubble cap velocity inducing the flow reversal with possibly ending up with vapour presence in the inlet divider manifold.

However, consider that an upstream movement of the bubble will move the liquid at its rear upstream towards the inlet divider manifold. This liquid motion also invokes an additional pressure to the rear of the bubble. This results in a positive contribution to the hydrodynamic force,  $F_{hyd}$ . Enlargement of this additional pressure at the rear of the bubble can prevent vapour from entering the divider manifold. A channel entrance of reduced size will increase the additional pressure induced by the liquid flow reversal. This is shown in the numerical calculations performed by Mukherjee and Kandlikar (2005).

Due to the negligible inflow during bubble blockage, the pressure at the rear of the bubble is expected be equal to the divider manifold pressure at all times. When the bubble grows, the remaining channel length,  $L_{liq}$  in equation (5.16), will reduce and therefore the hydrodynamic force towards detaching the bubble will become larger. Therefore, at a certain position,  $L_{liq}$ , the bubbles have to detach, when the overall pressure drop (" $P_{manifold} - P_{end}$ ") of the device exceeds the attaching force of the bubble. This analysis points out, as well, that if the overall pressure drop does not exceed the bubble attaching force, a bubble will always remain attached since any bubble growth velocity only reduces the detaching pressure drop. This means that under those conditions a vapour bubble will always push out the remaining liquid in the channel. A restricted entrance will increase the overall pressure drop, and

therefore make it less likely for a vapour bubble to completely fill the length of the channel.

The additional overall pressure drop, induced by the entrance restriction has a positive influence on obtaining a uniform the flow distribution over the different channels. Also, this restriction decreases the compliance effect of neighbouring channels influencing each other.

## ***5.5 Conclusions***

The results of our investigation on the origin of the pressure fluctuations and the possible flow reversal yield a better understanding of these phenomena. First, the measured length of a slug bubble at detachment agrees with the trend obtained by scaling analysis using a hydrodynamic force balance. The slope of the predicted linear correlation through the measurements corresponds to a 2% film thickness. This relative film thickness is similar to the values given in literature (Kolb and Cerro 1991). By applying a similar hydrodynamic force balance on a multiple channel array, a criterion is found predicting vapour flow reversal, equation (5.16).

Within this criterion the bubble cap velocity is an important parameter. High-speed camera recordings allowed us to obtain the vapour bubble length during its explosive growth. Using simple assumptions it is possible to find an explicit relation for the vapour bubble length in time. After optimisation of the film thickness, this relation shows reasonable agreement with our explosive bubble length measurements.

The explosive bubble growth model combined with the criterion predicting vapour flow reversal allows us to design the inlet restriction. The explosive bubble growth velocity can be related to a pressure fluctuation, which has to be dealt with by the flow invoked inlet restriction pressure drop.

## 6 Conclusions and future work

In this chapter we summarise the conclusions we have reached regarding the three main topics of our research. Namely, the adiabatic two-phase flow pattern map in small diameter channels, confined pool boiling, and the research on boiling within small diameter channels, all which have been addressed in this thesis. Finally recommendations for future work will be given as well.

### 6.1 Conclusions

The typical size of the “small geometries” regarded here range from about 5 mm down to about 0.1 mm. Furthermore, in general the liquid phase is water and the gaseous phase is either air or water vapour. In general standard conditions (i.e. pressure  $\sim 1 \cdot 10^5$  Pa and ambient temperature  $\sim 293$  K) are considered.

An overview is given on two-phase flow pattern maps available in the literature, which are measured within small diameter channels ( $0.5 < Co < 50$ ). Only three anchor flow regimes are identified: bubble flow, slug flow, and annular flow. A reasonable agreement is found between these two-phase flow pattern maps found in literature. Likewise corresponds the present work ( $3 < Co < 25$ ) to the maps found in literature. This correspondence justifies the superficial velocity as a scaling parameter in plotting the two-phase flow pattern maps for both large diameter channels ( $Co < 0.5$ ) as small diameter channels ( $Co > 0.5$ ). The agreement indicates as well, a weak dependence on the actual shape of the small diameter channel on the flow pattern, see section 3.1.5.

The present work extends the researched regions of the two-phase flow pattern map to much lower superficial liquid velocities, in which the occurrence of stratified flow might be expected. The present experiments show no stratified flow or wavy flow pattern region. Therefore, in order to theoretically predict the transition lines the stratified flow is most likely not the most adequate initial two-phase flow pattern. Annular flow is suggested to be a more appropriate initial two-phase flow pattern, see section 3.3.6.

The present work on confined pool boiling demonstrates an enhancement of the nucleate boiling heat flux when the boiling pot diameter is decreased. In the nucleate boiling regime the heat flux in confined boiling is between 5 to 10 times higher than the heat flux for unconfined pool boiling, see Figure 4.16.

The analysis of possible errors and a variation of experimental parameters excludes that the observed enhancement is the result of the chosen boiling liquid, the variation in boiling pot depth, the material of the bounding wall, or the variation in the diameter of the inlet water supply, see section 4.3.3.

An explanation is found in the singularisation of the basic process for nucleate pool boiling, leading to a different flow behaviour. The flow pattern is chaotic in the case of unconfined pool boiling, and it becomes directed and circulating as the dimensions of the confinement are reduced. The circulating fluid motion augments

the entrainment of liquid by the vapour bubbles, and hence it significantly increases the heat transfer in the nucleate boiling regime, see section 4.4.1.

Due to the enhancement, the heat flux does not show a rapid decrease for temperatures below the CHF. This allows an operation of the device at a comfortable temperature safety margin with respect to the critical superheat temperature without compromising too much in heat transfer capacity. Confined pool boiling could be integrated on a large scale by means of 'numbering up' or 'scaling out', see section 4.4.2.

The present work on the origin of the pressure fluctuations and the possible flow reversal during flow boiling in small diameter channels yield a better understanding of these phenomena. The measured length of a slug bubble at detachment agrees with the trend obtained by scaling analysis using a hydrodynamic force balance. The slope of the predicted linear correlation through the measurements corresponds to a 2% film thickness. This relative film thickness is similar to the values given in literature. By applying a similar hydrodynamic force balance on a multiple channel array, a criterion, equation (5.16), is found predicting vapour flow reversal, see section 5.4.1.

Within the flow reversal criterion, equation (5.16), the bubble cap position as a function of time is an important parameter. High-speed camera recordings allowed us to obtain the vapour bubble length during its explosive growth. Using simple assumptions it is possible to find an explicit relation for the vapour bubble length in time. After optimisation of the film thickness, this relation shows reasonable agreement with our explosive bubble length measurements, see section 5.4.3.

The explosive bubble growth velocity can be related to a pressure fluctuation, which has to be dealt with by the flow invoked inlet restriction pressure drop. The explosive bubble growth model combined with the criterion predicting vapour flow reversal allows us to design the inlet restriction, see section 5.4.4.

## ***6.2 Recommendations for future work***

With respect to the two-phase flow pattern mapping, the variance in transition lines may indicate some uncontrolled influence, or hysteresis, or chaotic behaviour. Further investigations are suggested, emphasising the less subjective determination methods like pressure drop measurements or (void) frequency measurements.

The investigated regions of the two-phase flow pattern map may be extended further to even lower superficial liquid velocities and superficial gas velocities. If annular flow is found within these regions, it will support our hypothesis that annular flow is a more appropriate initial two-phase flow pattern for small diameter channels.

Further two-phase flow pattern map research on channels with even smaller diameters ( $1 \mu\text{m} < D < 100 \mu\text{m}$ ) is interesting since within this range the no-slip condition for gasses no longer holds ( $0.1 > \text{Kn} > 0.001$ ). This slip between the gaseous phase and the liquid phase may cause new two-phase flow patterns to occur.

With respect to the confined pool boiling mechanism, further detailed visualisation is of interest. It is a challenge to perform PIV measurements within the confined boiling structure to visualise the liquid flow patterns. High speed visualisations from the bottom boiling surface will lead to further understanding as well. A transparent and uniformly heated boiling surface have to be used for these visualisations.

The confined pool boiling mechanism has only be tested for single liquids. Within industry many mixtures are be processed and evaporated. The evaporation behaviour of these mixtures differs from single liquids, therefore their behaviour during confined pool boiling may change as well.

Further investigations on the 'outscaling' or 'numbering up' to implement the confined pool boiling mechanism at an industrial level are recommended. Within the current outscaling setup heat transfer enhancement was achieved only on applying the described experimental method. More robust techniques should become available and investigated.

With respect to the slug bubble length measurements at detachment, the unexplained data point at 1500 s/m (flow = 0.01 ml/min) needs further research. A variation in channel diameter or using another liquid are possible option for further research.

Despite the experimental work already performed in literature (e.g. Kolb and Cerro 1991; and Thulasidas 1995) further detailed measurements on the liquid film layer thickness are desired. The fluorescence technique, applied in the present work to determine the two-phase flow pattern, offers opportunities to perform these detailed measurements accurately. For both the bubble detachment measurements as the explosive bubble growth measurements the liquid film thickness is an important parameter, however so far unknown.

More accurate temperature measurements of the wall temperature in the research on the explosive bubble growth during boiling in small diameter channels are welcome. The rather large uncertainty in the actual wall superheat (0.5 K) introduces large model prediction margins. Careful calibration of the thermocouples and a (three dimensional) thermal analysis of the temperature field inside the aluminium block containing the multiple channels, should narrow down the uncertainty margin to 0.1 K.

The explosive bubble growth model, as presented in section 5.2.3, includes no secondary effects such as inertia, surface tension or friction. Especially in case of very large accelerations (e.g. long bubbles) the inertia effects become important and should therefore be included in the next analytical model on explosive bubble growth. Secondly, in the present model all newly created film (i.e. by bubble growth) is of equal thickness as the already existing liquid film. Hence no bubble cap velocity dependency ( $\sim Ca^{2/3}$ ) or time delay is included. This assumption for the current analytical model needs refinement as well.



# Samenvatting

Met het beschikbaar komen van nieuwe productie technieken in de jaren 80, diende de mogelijkheid voor massa productie van microfluïde systemen zich aan. De werking van een systeem wordt veranderd door het verkleinen van de afmetingen. Fysische fenomenen welke opereren op volumes, zoals zwaartekracht en traagheid, worden minder belangrijk ten opzichte van fysische fenomenen welke opereren op oppervlakten of lijnen, zoals drukken en oppervlakte spanning. Dit relatief nieuwe onderzoeksgebied van kleine fluïdische systemen wordt "*micro-fluidics*" genoemd.

Een microfluïde stroming kan gekarakteriseerd worden met behulp van dimensieloze kentallen zoals het Reynolds getal ( $Re$ ), Weber getal ( $We$ ), Knudsen getal ( $Kn$ ) en het Bond getal ( $Bo$ ). Een gas-vloeistof tweefase systeem wordt klein geacht als het Bond getal kleiner is dan 4, ofwel zijn inverse wortel (ook wel het "confinement number",  $Co$ , genoemd) moet groter zijn dan 0.5.

In het huidige werk is de interactie van het warmte transport tijdens de faseovergang en het tweefase gedrag van een stroming in een kleine geometrie onderzocht. Hiertoe is het onderzoek in twee delen opgesplitst:

1. Interactie tweefase stroming en kleine geometrie
2. Interactie warmteoverdracht tijdens faseovergang en kleine geometrie

De typische grootte van de "kleine geometrie" varieert tussen de 0.1 mm en 5 mm. Over het algemeen is voor de vloeistoffase water gekozen en de gasfase is ofwel lucht ofwel waterdamp. Verder zijn de standaard condities aangenomen (omgevingsdruk  $\sim 1 \cdot 10^5$  Pa en temperatuur  $\sim 293$  K).

Om een theoretische basis te bieden zijn de algemene tweefase stromingsbegrippen geïntroduceerd, zoals de superficiële snelheid en het tweefase stroming diagram. In de literatuur wordt een verandering van het tweefase stroming diagram gerapporteerd wanneer de kanaaldiameter verkleind wordt. Zo komt bijvoorbeeld de horizontaal gestratificeerde stroming niet voor in kanalen met een kleine diameter. Slechts drie basis stromingspatronen kunnen geïdentificeerd worden: bellen stroming, slug stroming en annulaire stroming. Basiskennis en de laatste inzichten met betrekking tot het gedrag van een kookbel, kernkoken en koken in een kanaalstroming zijn gegeven. Verschillende warmteoverdracht mechanismen gedurende het kernkoken zijn beschreven, als mede hun interacties.

Een overzicht van de reeds in de literatuur beschikbare tweefase stroming diagrammen is gegeven, welke gemeten zijn in kanalen met een kleine diameter ( $0.5 < Co < 5$ ). Deze in de literatuur gevonden tweefase stroming diagrammen vertonen een redelijke overeenstemming. De resultaten verkregen in het huidige werk zijn tevens in overeenstemming met de tweefase stroming diagrammen gevonden in de literatuur. Deze algemene overeenstemming rechtvaardigt de keuze om de superficiële snelheid te gebruiken als schaalparameter voor tweefase stroming diagrammen van zowel grote kanalen als kleine kanalen. Het huidige werk vergroot de onderzochte gebieden van het tweefase stroming diagram naar veel

lagere superficiële vloeistof snelheden, alwaar een gestratificeerd stromingspatroon verwacht wordt. De huidige experimenten vertonen geen gestratificeerd stromingspatroon. Daarom achten wij het gestratificeerd stromingspatroon niet als het meest geschikte initiële stromingspatroon om theoretisch de fase overgangen te voorspellen. Annulaire stroming achten we als een geschikter initieel tweefase stromingspatroon.

Het huidig onderzoek aan koken op een beperkt oppervlak laat een verhoging van de kook warmteoverdracht zien, wanneer de diameter van de kookpot verkleint wordt. In het kern kook regime is de warmteoverdracht in een beperkte geometrie een factor 5 tot 10 groter dan de warmteoverdracht in een onbeperkte geometrie. Een foutanalyse en een variatie van experimentele parameters sluiten uit dat de geobserveerde verhoging een resultaat is van de gekozen kookvloeistof, variatie in kookpot hoogte, het materiaal van de wanden van het kookpotje, of variatie in de diameter van de vloeistof toevoer. Een verklaring is gevonden in het verenkeldigheid van het basis proces van kern koken, wat leidt tot een ander stromingsgedrag in het kookpotje. Het stromingspatroon is chaotisch in het geval van koken in een onbeperkte geometrie, en het wordt geregeld en circulerend als de geometrie verkleind en beperkend worden. De circulerende stroming vergroot het meeslepen van vloeistof door de damp bellen en verhoogd daardoor significant de warmteoverdracht in het kernkook regime. Het mechanisme van koken op een beperkt oppervlak zou geïntegreerd kunnen worden op een groter oppervlak door middel van 'numbering up' ofwel 'scaling out'.

Ons huidig onderzoek naar koken in kanalen met een kleine diameter geeft een beter begrip van de oorzaak van drukfluctuaties en de mogelijke omkering van de stromingsrichting. Ten eerste komt de gemeten slugbellengte op het moment van loslaten overeen met de trend verkregen uit een analytische beschouwing voorkomend uit een hydrodynamische krachten balans. De helling van de voorspelde lineaire correlatie correspondeert met een vloeistof filmlaag dikte van 2%. Deze waarde is overeenkomstig met waarden gegeven in de literatuur. Vervolgens kan, door het opstellen van een vergelijkbare hydrodynamische balans over een array van kanalen, een criterium worden opgesteld ter voorspelling van het omkeren van de stromingsrichting. Binnen dit omkeer criterium de snelheid van de uiteinden van de exploderende bel als functie van de tijd een belangrijke parameter. Door middel van opnamen met een hoge snelheid camera is het mogelijk geweest om de dampbel lengte tijdens de explosieve bel groei te meten. Met behulp van vereenvoudigende aannamen zijn we in staat om een expliciete relatie te vinden voor de dampbel lengte in de tijd. Na optimalisatie van de film dikte, was deze relatie in redelijke overeenstemming met onze bel lengte metingen. De relatie voor de explosieve belgroei gecombineerd met het criterium om omkering van de stroming te voorspellen stelt ons in staat om nodige de inlaat restrictie te ontwerpen.

## Bibliography

- Ali, M.I., Sadatomi, M., and Kawaji, M. (1993) Two-phase flow in narrow channels between two flat plates. *Canadian journal of chemical engineering*, **71**, pp. 657–666.
- Aoshima, R., Chiba, T., and Asai, H. (1984) Thin-layer optical cell with light path length shorter than 10mm for absorption and fluorescence measurement of highly absorbent solutions. *Applied optics*, **23**(4), pp. 597-600.
- Aussilous, P., and Qu ere, D. (2000) Quick deposition of a fluid on the wall of a tube. *Physics of fluids*, **12**(10), pp. 2367–2371.
- Basu, N, Warriar, G.R., and Dhir, V.K. (2002) Onset of nucleate boiling and active nucleation site density during subcooled flow boiling. *Journal of heat transfer*, **124**, pp. 717-728.
- Basu, N., Warriar, G.R., and Dhir, V.K (2005a) Wall heat flux partitioning during subcooled flow boiling: Part 1— model development. *Journal of heat transfer*, **127**, pp. 131-140.
- Basu, N., Warriar, G.R., and Dhir, V.K (2005b) Wall heat flux partitioning during subcooled flow boiling: Part II— model validation. *Journal of heat transfer*, **127**, pp. 141-148.
- Benjamin, R. J., and Balakrishnan A. R. (1997) Nucleation site density in pool boiling of saturated pure liquids: Effect of surface microroughness and surface and liquid physical properties. *Experimental Thermal and Fluid Science*, **15**, pp. 32-42.
- Beek, W.J. (1965) Oscillations and vortices in a batch of liquid sustained by a gas flow. *Proceedings of Symposium on Two-Phase Flow*, Exeter, United Kingdom.
- Bergles, A.E., Lienhard, J.H., Gail, V., Kendal, E., and Griffith, P. (2003) Boiling and evaporation in small diameter channels. *Heat transfer engineering*, **24**(1), pp. 18–40.
- Bird, G.A. (1994) *Molecular gas dynamics and the direct simulation of gas flows*. Clarendon press, Oxford, United Kingdom.
- Bonjour, J., and Lallemand, M. (1998) Flow patterns during boiling in a narrow space between two vertical surfaces. *International journal of multiphase flow*, **24**, pp. 947–960.
- Bosnjakovic, F. (1930) Verdampfung und Flussigkeitsuberhitzung. *Tech. Mech. Thermodyn. Bevl.*, **1**, pp. 358-362
- Bowring, R.W. (1962) Physical model based on bubble detachment and calculation of steam voidage in the subcooled region of a heated channel. *HPR-10, Institutt for Atomenergi*, Halden, Norway.
- Bretherton, F.P. (1961) The motion of long bubbles in tubes. *Journal of fluid mechanics*, **10**, pp. 166-188.

- Brutin, D., and Tadrist, L. (2004) Pressure drop and heat transfer analysis of flow boiling in a minichannel: influence of the inlet condition on two-phase flow stability. *International journal of heat and mass transfer*, **47**, pp. 2365–2377.
- Brutin, D., Topin, F., and Tadrist, L. (2003) Experimental study of unsteady convective boiling in heated minichannels. *International journal of heat and mass transfer*, **46**, pp. 2957–2965.
- Butterworth, D. (1975) A comparison of some void-fraction relationships for co-current gas-liquid flow. *International journal of multiphase flow*, **1**, pp. 845-850.
- Chen, J.C. (1963) A correlation for boiling heat transfer to saturated fluid in convective flow. *ASME Paper*, 63-HT-34, pp. 1–11.
- Chen, L., Tian, Y.S., and Karayiannis T.G. (2006) The effect of tube diameter on vertical two-phase flow regimes in small tubes. *International journal of heat and mass transfer*, 49(21), pp.4220-4230.
- Chen, Y. (2002) Study of forces acting on a growing bubble from a smooth surface. *International journal of heat & technology*, **20**, pp. 31-40.
- Chung, P.M.-Y., and Kawaji M. (2004) The effect of channel diameter on adiabatic two-phase flow characteristics in microchannels. *International journal of multiphase flow*, **30**, pp. 735–761.
- Davis, E.J., and Anderson, G.H. (1966) The incipience of nucleate boiling in forced convection flow. *American institute of chemical engineers AIChE Journal*, **12**(4), pp. 774-780.
- Dias, I., and Riethmuller, M.L. (1998) PIV in two-phase flows: simultaneous bubble sizing and liquid velocity measurements. *Proceedings of 9<sup>th</sup> International symposium on applications of laser techniques to fluid mechanics*, Lisbon, Portugal
- Dhir, V.K. (1998) Boiling heat transfer. *Annual review of fluid mechanics*, **30**, pp. 365-401.
- Dittus, F.W., and Boelter, L.M.K. (1930) Heat transfer in automobile radiators of the tubular type. *University of California publication on engineering*, **2**, pp. 443–461.
- Dombrowski, N., Foumeny, E.A., Ookawara, S., and Riza, A. (1993) Influence of the Reynolds number on the entry length and pressure drop for laminar pipe flow. *The Canadian journal of chemical engineering*, **71**, pp. 472-476.
- Dupont, V., Thome, J.R., and Jacobi, A.M. (2004) Heat transfer model for evaporation in microchannels. Part II: comparison with the database. *International journal of heat and mass transfer*, **47**, pp. 3387–3401.
- Forschungszentrum Karlsruhe (2008) Developments on micro process engineering datasheets. Electronic distribution.
- Forster, H.K., and Zuber, N. (1955) Dynamics of vapor bubbles and boiling heat transfer. *American institute of chemical engineers AIChE Journal*, **1**(4), pp. 531-535.
- Fox, R.W., and McDonald, A.T. (1985) *Introduction to fluid mechanics*. 3<sup>rd</sup> edition Wiley, New York, United States of America.

- Gad-El-Hak, M. (1999) The fluid mechanics of microdevices - the freeman scholar lecture. *Journal of Fluids Engineering*, **12**(1), pp.5-33.
- Gad-El-Hak, M. (2003) Comments on "Critical view on new results in micro-fluid mechanics" *International journal of heat and mass transfer*, **46**(20), pp.3941-3945.
- Geld, C.W.M. (2000) A note on the bubble growth force. *Multiphase science and technology*, **12**(3,4), pp.215-232.
- Geld, C.W.M. (2007) The dynamics of a boiling bubble before and after detachment. *Heat and mass transfer*, Special Issue, DOI 10.1007/s00231-007-0254-7.
- Gungor, K.E., and Winterton, R.H.S. (1986) A general correlation for flow boiling in tubes and annuli. *International journal of heat and mass transfer*, **29**(3). pp. 351-358.
- Happel J, and Brenner H. (1983) *Low Reynolds number hydrodynamics*. Martinus Nijhoff, Dordrecht, The Netherlands.
- Hazel, A.L., and Heil, M. (2002) The steady propagation of a semi-infinite bubble into a tube of elliptical or rectangular cross-section. *Journal of fluid mechanics*, **470**, pp. 91–114.
- Helden, W.G.H. (1994) On detaching bubbles in upward flow boiling. *Dissertation* Eindhoven University of Technology, Eindhoven, The Netherlands.
- Helden, W.G.H., Geld, C.W.M., and Boot, P.G.M., (1995) Forces on bubbles growing and detaching in flow along a vertical wall. *International journal of heat and mass transfer*, **38**(11), pp.2075-2088.
- Henry, C.D., and Kim, J. (2004) A study of the effects of heater size, subcooling, and gravity level on pool boiling heat transfer. *International journal of heat and fluid flow*, **25**, pp. 262-273.
- Herwig, H., and Hausner, O. (2003) Critical view on "new results in micro-fluid mechanics: an example. *International journal of heat and mass transfer*, **46**(5), pp.935-937.
- Hetsroni, G., Segal, Z., and Mosyak, A. (2000) Nonuniform temperature distribution in electronic devices cooled by flow in parallel microchannels. *Packaging Electronic Photonic Devices , EEP-*, **28**, pp. 1–9.
- Hornbeck, R.W. (1964) Laminar flow in the entrance region of a pipe. *Applied scientific research*, **13**, pp. 224-232 .
- Hsu Y.Y. (1962) On the size range of active nucleation sites on a heating surface. *Journal of heat transfer*, **84**, pp. 207-216.
- Incropera, F.P., and DeWitt D.P. (2002) *Fundamentals of heat and mass transfer*. John Wiley and Sons, Hoboken (NJ), United States of America.
- Jakob, M. and Linke, W. (1935) Der Wärmeübergang beim verdampfen von Flüssigkeiten an senkrechten und waagerechten Flächen. *Physikalische zeitschrift*, **36**(8), pp. 267-280.

- Kandlikar, S.G. (1990) A general correlation for saturated two-phase flow boiling heat transfer inside horizontal and vertical tubes. *Journal of heat transfer*, **112**(1), pp. 219-228.
- Kandlikar, S.G. (2002) Two-phase flow patterns, pressure drop, and heat transfer during boiling in minichannel flow passages of compact evaporators. *Heat transfer engineering*, **23**, pp. 5-23.
- Kandlikar, S.G. (2004) Heat transfer mechanisms during flow boiling in micro channels. *Journal of heat transfer*, **126**, pp. 8-16.
- Kandlikar, S. G., and Balasubramanian, P. (2003) High speed photographic observation of flow patterns during flow boiling in a single rectangular minichannel. *Proceedings of the ASME summer heat transfer conference*, Las Vegas (Nevada), United States of America.
- Karniadakis, G.E., and Beskok, A. (2002) *Micro flows: fundamentals and simulation*. Springer-Verlag, New York, United States of America.
- Kawahara, A., Chung, P.M.-Y., and Kawaji, M., (2002) Investigation of two-phase flow pattern, void fraction and pressure drop in a microchannel. . *International journal of multiphase flow*, **28**, pp. 1411–1435.
- Kenning, D.B.R., Wen, D.S., Das, K.S., and Wilson, S.K. (2006) Confined growth of a vapour bubble in a capillary tube at initially uniform superheat: Experiments and modelling. *International journal of heat and mass transfer*, **49**, pp. 4653–4671.
- Kew, P., and Cornwell, K. (1997) Correlations for prediction of boiling heat transfer in small diameter channels. *Applied thermal engineering*, **17**(8-10), pp. 705-715.
- Kim, J.H., You, S.M. and Pak, J.Y. (2006) Effects of heater size and working fluids on nucleate boiling heat transfer. *International journal of heat and mass transfer*, **49**, pp. 122-131.
- Kolb, W.B., Cerro, R.L. (1991) Coating the inside of a capillary of square cross-section. *Chemical engineering science*, **46**(9), pp. 2181-2195.
- Kolb, G., and Hessel, V. (2004) Micro-structured reactors for gas phase reactions. *Chemical engineering journal*, **98**, pp. 1-38.
- Kreutzer, M.T. (2003) Hydrodynamics of Taylor flow in capillaries and monoliths channels. *Doctoral dissertation*. Delft university of technology, Delft, The Netherlands.
- Kreutzer, M.T., Kapteijn, F., Moulijn, J.A., and Heiszwolf, J.J. (2005) Multiphase monolith reactors: chemical reactor engineering of segmented flow in microchannels. *Chemical engineering science*, **60**, pp. 5895-5916.
- Kruzhilin, G.N. (1947) Free-convection transfer of heat from a horizontal plate and boiling liquid. *Doklady AN SSSR (Reports of the USSR Academy of Sciences, in Russian)*, **58**(8), pp. 1657–1660.
- Kutateladze, S.S. (1948) On the transition to film boiling under natural convection. *Kotloturbostroenie*, **3**, pp. 10-18.

- Kutateladze, S.S., and Borishanskii, V.M. (1966) *A concise encyclopedia of heat transfer*. Pergamon Press, New York (NY), United States of America.
- Kwok, D.Y., Leung A., Lam, C.N.C., Li, A., Wu, R., and Neumann, W. (1998) Low-Rate dynamic contact angles on Ploy(methyl methacrylate) and the determination of the solid surface tension. *Journal of colloid and interface science*, **206**(1), pp. 44-51.
- Labuntsov, D.A. (1972) Heat transfer problems with nucleate boiling of liquids. *Thermal engineering*, **19**(9), pp. 21–28.
- Lay, J.H., and Dhir, V.K. (1994) A nearly theoretical model for fully developed nucleate boiling of saturated liquids. *Proceedings of 10<sup>th</sup> international heat transfer conference*, Brighton, United Kingdom.
- Lee, Y., Piro, I.L., and Park, H.J. (1994) An experimental study on a plate type two-phase closed thermosyphon. *Proceedings of 4<sup>th</sup> international heat pipe symposium*, Tsukuba, Japan.
- Ledinegg, M. (1938) Instability of flow during natural and forced circulation. *Wärme*, **61**(8), pp. 891–898.
- Leib, S.J., and Goldstein, M.E. (1986) The generation of capillary instability on a liquid jet. *Journal of fluid mechanics*, **168**, pp. 479-500.
- McGillis, W.R., Fitch, J.S., Hamburg, W.R., and Carey, V.P. (1990) Pool boiling enhancement techniques for water at low pressure. *Research report 90/9, Western research laboratory*, California, United states of America.
- Mingming, W., and Morteza, G. (2002) Experimental studies on the shape and path of small air bubbles rising in clean water. *Physics of fluids*, **14**(7), L49-L52.
- Moghaddam, S., and Kiger, K.T. (2004) Pool boiling mechanism of HFE-7100. *Proceedings of ASME Heat transfer/Fluid engineering summer conference*, Charlotte (North Carolina), United States of America.
- Mori, B.K., and Baines, W.D. (2001) Bubble departure from cavities. *International journal of heat and mass transfer*, **44**, pp. 771-783.
- Mostinski, I.L. (1963) Calculation of heat transfer and critical heat flux in boiling liquids based on the law of corresponding states. *Teploenergetica*, **10**(4), pp. 66-71.
- Mukherjee, A., Kandlikar, S.G. (2005) Numerical study of the effect of inlet constriction on bubble growth during flow boiling in microchannels. *Proceedings of 3<sup>th</sup> international conference on micro and minichannels*, Toronto (Ontario), Canada.
- Myers, J.G., Yerramilli, V.K., Hussey, S.W., Yee, G.F., and Kim, J. (2005) Time and space resolved wall temperature and heat flux measurements during nucleate boiling with constant heat flux boundary conditions. *International journal of heat and mass transfer*, **48**(12), pp. 2429-2442.
- Mudde, R.F. (2005) Gravity-driven bubbly flows. *Annual review of fluid mechanics*, **37**, pp. 393-423.

- Niño, V.G., Hrnjak, P.S., and Newell, T.A. (2003) Two-phase flow visualization of R134A in a multiport microchannel tube. *Heat transfer engineering*, **24**(1) pp. 41-52.
- Nukiyama, S. (1966) The maximum and minimum values of the heat Q transmitted from metal to boiling water under atmospheric pressure. *International journal of heat and mass transfer*, **9**, pp. 1419–1433.
- Peles, Y. P., Yarin, L. P., and Hetsroni, G. (2001) 'Steady and unsteady flow in a heated capillary. *International journal of multiphase flow*, **27**(4), pp. 577–598.
- Pirotto, I.L., Rohsenow, W., and Doerffer, S.S. (2004) Nucleate pool-boiling heat transfer II: assessment of prediction methods. *International journal of heat and mass transfer*, **47**, pp. 5045–5057.
- Pirotto, I. (1997) Boiling heat transfer characteristics of thin liquid layers in a horizontally flat two-phase thermosyphon. *Preprints of the 10<sup>th</sup> International Heat Pipe Conference*, Stuttgart, Germany.
- Plesset, M. S., and Zwick, S. A. (1952) A nonsteady heat diffusion problem with spherical symmetry. *Journal of Applied Physics*, **23**, pp. 95-98.
- Plesset, M. S. and Zwick, S. A. (1954) The Growth of Vapor Bubbles in Superheated Liquids *Journal of Applied Physics*, **25**, pp. 493-500.
- Qi, Y. and Klausner, J.F. (2006) Comparison of nucleation site density for pool boiling and gas nucleation. *Journal of heat transfer*, **128**, pp. 13-20.
- Rao, G.V., and Balakrishnan, A.R. (2004) Heat transfer in nucleate pool boiling of multicomponent mixtures. *Experimental thermal and fluid science*, **29**, pp. 87-103.
- Raykoff, T., and Kandlikar, S.G. (1997) Bubble characteristics and convective effects in the flow boiling heat transfer of binary mixtures.; *Engineering foundation conference on Convective and pool boiling*, Irsee, Germany.
- Rohsenow, W.M. (1952) A method of correlating heat transfer data for surface boiling of liquids. *Transactions of the ASME*, **74**, pp. 969-976.
- Rohsenow, W.M. (1971) Boiling. *Annual review of fluid mechanics*, **3**, pp. 211-236.
- Rops, C.M., Lindken, R., Westerweel, J., and Velthuis, J.F.M. (2005) Enhanced heat transfer for pool boiling at micro scale. *ECI International conference on heat transfer and fluid flow in microscale*, Castelvecchio Pascoli, Italy.
- Rops, C.M., Lindken, R., Westerweel, J., and Velthuis, J.F.M. (2006) Enhanced heat transfer in microscale boiling. *ECI International conference on boiling heat transfer*, Spoleto, Italy.
- Sakashita, H., and Kumada, T. (2001) Method for predicting boiling curves of saturated nucleate boiling. *International journal of heat and mass transfer*, **44**,(3), pp. 673-682.
- Shapiro, A. H. (1953) *The dynamics and thermodynamics of compressible fluid flow*. Ronald Press, New York (NY), United States of America.

- Schlünder, E.-U., Gnielinski, V., Martin, H., Muschelknautz, M., Stephan, K., Steiner, D., and Vortmeyer, D. (1994) *VDI Wärmeatlas, siebte erweiterte auflage*. VDI-Verlag GmbH, Düsseldorf, Germany.
- Shah, M.M. (1982) Chart correlation for saturated boiling heat transfer: Equations and further study. *American Society of Heating, Refrigerating and Air-Conditioning Engineers: ASHRAE Transactions*, **88** (1), pp. 185-196.
- Shah, R.K. (2005) Compact heat exchangers for microturbines. *Proceedings of 5<sup>th</sup> international conference on: Enhanced, compact and ultra compact heat exchangers*, Hoboken (New York), United States of America.
- Sobierska, E., Shuai, J., Kulenovic, R., and Groll, M. (2004). Visualisation and flow pattern map for flow boiling of water in a vertical microchannel, *Proceedings of micro and minichannels*, Rochester (New York), USA.
- Steiner, H., Kobor, A., and Gebhard, L. (2005) A wall heat transfer model for subcooled boiling flow. *International journal of heat and mass transfer*, **48**, pp. 4161–4173
- Steinke, M. E., and Kandlikar, S. G. (2003) Flow boiling and pressure drop in parallel microchannels. *Proceedings of 1<sup>st</sup> international conference on microchannels and minichannels*, Rochester (NY), United States of America.
- Tabatabai, A., and Faghri, A. (2001) A new two-phase flow and map transition boundary accounting for surface tension effects in horizontal miniature and micro tubes. *Transactions of the ASME*, **123**, pp. 958-968.
- Tadrist, L. (2007) Review on two-phase flow instabilities in narrow spaces. *International journal of heat and fluid flow*, **28**, pp. 54-62.
- Taitel, Y., and Dukler, A.E. (1976) A model for predicting flow regime transitions in horizontal and near horizontal gas-liquid flow. *American institute of chemical engineers AIChE Journal*, **22**(1), pp. 47-55.
- Taitel, Y., Bornea, D., and Dukler, A.E. (1980) Modelling flow pattern transitions for steady upward gas-liquid flow in vertical tubes. *American institute of chemical engineers AIChE Journal*, **26**(3), pp. 345-354.
- Taylor, G.I. (1961) Deposition of a viscous fluid on the wall of a tube. *Journal of fluid mechanics*, **10**, pp. 161-165.
- Thome, J.R., Dupont, V., and Jacobi, A.M. (2004) Heat transfer model for evaporation in microchannels. Part I: presentation of the model. *International journal of heat and mass transfer*, **47**, pp. 3375–3385.
- Thome J.R. (2004) *Wolverine engineering data book III*. Wolverine Tube Inc. , Electronic distribution.
- Wambsganss, M.W., Jendrzejczyk, J.A., and France, D.M. (1991) Two-phase flow patterns and transitions in small, horizontal, rectangular channel. *International journal of multiphase flow*, **17**(3), pp. 327-342.

- Warrier, G.R., and Dhir, V.K. (1999) Review of experimental and analytical studies on low pressure subcooled flow boiling. *Proceedings of the 5<sup>th</sup> ASME/JSME joint thermal engineering conference*, San Diego (California), United States of America.
- Weast, R.C. et. al. (1980) *Handbook of chemistry and physics 60<sup>th</sup> edition*. CRC Press, Boca Raton (Florida), United States of America.
- Wu, W.-T., Yang, Y.-M., and Maa, J.-R. (1998) Nucleate pool boiling enhancement by means of surfactant additives. *Experimental thermal and fluid science*, **18**, pp. 195-209.
- Young, R.K., and Hummel, R.L. (1964) Improved nucleate boiling heat transfer. *Chemical engineering progress*, **60**(7) pp. 53-58.
- Zhang, L., and Shoji, M. (2001) A periodic bubble formation from a submerged orifice. *Chemical engineering science*, **56**, pp. 5371-5381.
- Zhang, L., and Shoji, M. (2003) Nucleation site interaction in pool boiling on the artificial surface. *International journal of heat and mass transfer*, **46**, pp. 513-522.
- Zhang, L., Wang, E.N., Goodson, K.E., and Kenny, T.W. (2005) Phase change phenomena in silicon microchannels. *International journal of heat and mass transfer*, **48**, pp. 1572-1582.
- Zhao, T.S., and Bi, Q.C. (2001) Co-current air-water two-phase flow patterns in vertical triangular microchannels. *International journal of multiphase flow*, **27**, pp. 765-782.
- Zhao, Y., Tsuruta, T., and Ji, C. (2003) Experimental study of nucleate boiling heat transfer enhancement in confined space. . *Experimental thermal and fluid science*, **28**, pp. 9-16.
- Zuber, N (1958) On the stability of boiling heat transfer. *Transactions of the ASME*, **80**, pp. 711-720.
- Zuber, N. (1961) The dynamics of vapor bubbles in nonuniform temperature fields. *International journal of heat and mass transfer*, **2**(1-2), pp. 83-98.
- Zuber, N., Tribus, M., and Westwater, J.W. (1961) The hydrodynamic crisis in pool boiling of saturated and subcooled liquids. *Proceedings of 2<sup>nd</sup> international developments in heat transfer*, Denver, United States of America.

## Curriculum Vitae

Cornelius Maria Rops was born on the 14<sup>th</sup> of May in Ulvenhout (Nieuw-Ginneken). In his home town he attended the primary school "de Rosmolen" (1979-1986) after which he successfully completed his secondary education at grammar school "het Stedelijk Gymnasium te Breda" (1986-1993). The following five years (1993-1998) he studied Applied Physics at the Delft University of Technology and obtained his masters degree (specialisation on fluid mechanics) "cum laude". The third year (1995/1996) of his studies he attended the courses at St. Andrews University (Scotland), and he performed a half year traineeship (1997) at Schlumberger Paris (France).

In February 1999 he joined TNO TPD (which is renamed to TNO Science & Industry) in the Process Physics department. During the five years before starting this PhD research he was involved in ceramics drying research, thermal and flow calculations on sensors & controllers and CFD work on the combustion process for space applications. In 2004 he started the PhD research on two-phase flow and phase change heat transfer at small structures in close collaboration with the Aero-and Hydrodynamics group of the Delft University of Technology. After this PhD research he is employing his microfluidic two-phase flow expertise at TNO Science & Industry.